

CHARACTERIZATION AND MICROSTRUCTURE CONTROL OF SHEATHED
SUPERCONDUCTING BiSrCaCuO THICK FILMS BY AC-ELECTRIC-FIELD
ASSISTED ELECTROPHORETIC DEPOSITION

BY

CHENG-FENG J. YUE

A DISSERTATION PRESENTED TO THE GRADUATE SCHOOL
OF THE UNIVERSITY OF FLORIDA IN PARTIAL FULFILLMENT
OF THE REQUIREMENTS FOR THE DEGREE OF
DOCTOR OF PHILOSOPHY

UNIVERSITY OF FLORIDA

1998

Copyright 1998

by

Cheng-Feng J. Yue

To my father, mother, elder sisters and younger brother, for
their love and support.

ACKNOWLEDGMENTS

I would like to acknowledge the many individuals who made this research work. First, I would like to appreciate my advisor, Dr. Rajiv K. Singh, for his guidance and support. The open atmosphere provided by him during these years that I worked with him has constructed a progressive and beneficial graduate study experience. I would like to thank Dr. Paul Holloway, Dr. Brij Moudgil, Dr. Kevin Jones, and Dr. Ramakant Srivastava for kindly participating on my advisory committee.

Several people assisting me with my research also greatly played an important role during my graduate study. Thanks especially go to Dr. Dhananjay Kumar for providing many hours of discussion and sharing his experiences precious to me. Thanks are also due to Jesse Arnault for his extensive technical assistance with mechanical testing.

I would like to also acknowledge all the friends and coworkers who made graduate school such as a memorable period. Dr. Jinghong Lee, Dr. Jeng Chen, Tzung-Ying Lee, Don Gilbert, Dong-Gu Lee, Ali Ata, Jeng Hu, Shan Sun, and others provided the social perspective that is necessary to prosper in life. Special thanks go to Everett Yang for his support and encouragement.

Thanks are due to the University of Florida, Engineering Research Center for Particle Science and Technology at the University of Florida, and the National Science Foundation, which have provided the resources to support the research work.

I would also like thank the administrative and support staff of the Department of Materials Science and Engineering for their efforts in making success possible.

Finally, I would like to thank my father, Chin-Yen Yue, my mother, Re-Yuen Chu, my brother, Jengyi, and sisters, Li-Shie and Shu-Jing, for the love and support to me over the many years of my extended education.

TABLE OF CONTENTS

ACKNOWLEDGMENTS	iv
LIST OF TABLES	ix
LIST OF FIGURES.....	x
ABSTRACT	xviii
CHAPTER I. INTRODUCTION	1
1.1 High Temperature Superconductor Tape/Wire	2
1.1.1 High- T_c Superconductors	6
1.1.2 Polycrystalline Film Synthesis	9
1.1.3 Arrangement and Boundary of Anisotropic Grains	14
1.2 Motivation and Objectives	17
1.3 Outline of This Dissertation	20
CHAPTER II. EXPERIMENTAL APPROACH	24
2.1 Introduction	24
2.2 Sequential Micro-lamination of Electrophoretic Deposition and Thermomechanical Consolidation	26
2.3 Preparation of BSCCO Powder Suspension Solution	27
2.4 Modified Electrophoretic Deposition	29
2.4.1 Particle Orientation Controllability by EPD Parameter	30
2.4.1.1 Substrate Configuration Condition	33
2.4.1.2 DC Field Strength Effect	33
2.4.1.3 Electric Flux Incident Angle Effect	36
2.4.1.4 Influence of Interparticulate Separation	36
2.4.1.5 Influence of Particle Size	36
2.4.2 C-axis Texturing Enhancement by Additional AC Electric Field Parallel to Substrate Surface	38
2.4.3 Electrode Configuration for Uniform Electric Field	40
2.5 Thermomechanical Consolidation Assisted Texturing	40
2-5-1 Uni-axial Pressure	43
2-5-2 Consolidation Temperature	43
2.5.2.1 Angular Distribution of C-axis Texturing	43
2.6 Sintering Enhanced C-axis Texturing	44
2.6.1 Green Film Condition Influences	44
2.6.1.1 BSCCO particle size influence	44
2.6.1.2 Silver sheathing effect	46
2.6.2 Sintering Parameter Effect on Superconductivity	46
2.7 Ag/BSCCO/Ag Tape Strengthening	47
2.7.1 Silver Particle Interlayer Strengthening	48
2.7.2 BSCCO Particle Size Consideration	50
2.7.3 Film Thickness Consideration	51
2.7.4 Consolidation Temperature Consideration	51

2.8	Material Characterization	52
2.8.1	Structural Characterization.....	52
2.8.2	Mechanical Characterization.....	53
2.8.3	Magnetic Characterization.....	54
CHAPTER III. AC-ELECTRIC-FIELD MODIFIED ELECTROPHORETIC DEPOSITION OF BiSrCaCuO FILMS		59
3.1	Introduction	59
3.2	Platy BSCCO Particle Alignment by DC Electric Field	61
3.2.1	DC Electric Field Strength Dependency	61
3.2.2	Electric Flux Incident Angle Effect	73
3.2.3	Influence of Inter-particulate Separation	76
3.2.4	Particle Aspect Ratio Consideration	81
3.3	C-axis Texturing Enhancement with Additional AC Electric Field Parallel to Substrate Surface	85
3.3.1	AC Electric Field Strength Effect	88
3.3.2	AC Electric Field Frequency Influence	91
3.3.3	DC Electric Field Strength Dependency	95
3.3.4	AC Field Influence on Average Deposition Rate ...	98
3.4	BSCCO Suspension Stability Study	104
3.5	Summary	108
CHAPTER IV. POST-DEPOSITION TEXTURING AND STRENGTHENING ...		110
4.1	Introduction	110
4.2	Thermomechanical Consolidation Enhanced C-axis Texturing	111
4.2.1	Uni-axial Pressure Dependence	113
4.2.2	Consolidation Temperature Influence	119
4.2.3	Silver margin Influence	125
4.2.4	Particle Size Influence.....	132
4.3	Sintering Enhanced C-axis Texturing	134
4.3.1	BSCCO Particle Size Influence	138
4.3.2	Silver Sheath Effect	140
4.4	Ag/BSCCO/Ag Tape Strengthening	143
4.4.1	BSCCO Particle Size Influence	145
4.4.2	Silver Particle Interlayer Strengthening	153
4.4.3	Film Thickness Influence	157
4.4.4	Consolidation Temperature Influence	160
4.5	Summary	163
CHAPTER V SUPERCONDUCTIVITY CHARACTERIZATIONS		168
5.1	Introduction	168
5.2	Superconductivity Stability Improvement by AC- electric-field Modified Electrophoretic Deposition ...	171
5.2.1	Temperature Dependence	172
5.2.2	Magnetic Field Dependence	179
5.3	Processing Parameter Influence on Superconductivity ...	183
5.3.1	Particle Size Influence	185
5.3.2	Uni-axial Pressure Effect	192
5.3.3	Consolidation Temperature Effect	196

5.3.4 Sintering Parameter Effect	201
5.4 Summary	207
CHAPTER VI COMPUTER SIMULATION MODEL FOR ANGULAR MOTION	
BEHAVIOR OF PLATY PARTICLE IN ACEPD	210
6.1 Introduction	210
6.2 Platy Particle Alignment By DC Electric Field	215
6.3 Angular Motion Behavior Of Platy Particle With Additional AC Electric Field Parallel To Substrate Surface	218
6.3.1 AC Electric Field Strength Effect On Platy Particle Orientation Control	219
6.3.2 AC Frequency Dependence Of Angular Motion Behavior Of Platy Particle	223
6.3.3 DC Electric Field Strength Effect On Angular Motion Behavior Of Platy Particle	226
6.3.4 DC Electric Field Strength Influence On Angular Motion Of Platy Particle Under High AC Electric Field And Frequency	230
6.3.5 Original Particle Orientation Influence On The Angular Motion Behavior Of Platy Particle	232
6.4 Summary	235
CHAPTER VII. CONCLUSIONS	237
APPENDIX A MAJOR X-RAY DIFFRACTION PEAKS OF BSCCO PHASES	241
APPENDIX B BEAN CRITICAL STATE MODEL	242
APPENDIX C COMPUTER SIMULATION PROGRAM CODES FOR ANGULAR MOTION BEHAVIOR OF PLATY BSCCO PARTICLE BY ACEPD	245
REFERENCES	247
BIOGRAPHICAL SKETCH	257

LIST OF TABLES

<u>Tables</u>	<u>Page</u>
1-1 The various winding forms of superconducting tape/wire for different electrical/magnetic applications.....	5
3-1 The Zeta potential of superconductor 2212 and 2223 powder suspensions.....	107
3-2 The dissolution concentrations of ions for BSCCO 2212 and 2223 in water with different pH values.....	107
4-1 Comparison of fracture and adhesion strength of Ag-sheathed BSCCO tapes prepared with and without fine Ag-particle interlayer introduced at the middle of BSCCO thick film.....	154
5-1 The superconductivity of peeled Ag/BSCCO/Ag tapes fabricated using BSCCO powder with different average particle sizes.....	188

LIST OF FIGURES

<u>Figure</u>	<u>Page</u>
1-1 The examples of high- T_c superconductor tape/wire applications: (a) Tokamak nuclear fusion reactor and (b) electromagnetic thruster (EMT).....	3
1-2 The schematics of general oxide-powder-in-tube fabrication processing for HTS wires and tapes.....	10
1-3 The schematics of high temperature superconductor BiSrCaCuO's (a) crystallographic structures and (b) the anisotropy.....	15
1-4 The schematic of sequential micro-lamination of electrophoretic deposition method and thermomechanical consolidation for Ag-sheathed superconducting BSCCO tapes fabrication.....	19
2-1 The Scanning Electron Microscopy microphotograph showing platy geometry of BiSrCaCuO particles	28
2-2 The schematic of electrophoretic deposition setup with in-situ monitoring capability of applied voltage and current.....	31
2-3 The schematic of substrate holder for electrophoretic deposition experiments with glass dielectric shields that allows only one face of substrate exposed to suspension solution.....	34
2-4 The schematic of electrode configurations: (a) far-apart electrodes without dielectric shielding over the near-edge area showing less electric flux parallelism; (b) closer electrodes with dielectric shielding showing better electric flux parallelism.....	35
2-5 The schematic of the substrate orientation experiment: the substrate is horizontally tilted with respect to the other electrode.....	37
2-6 The schematic of substrate holder with the AC electrodes for c-axis texturing enhancement experiments by additional AC electric field modified electrophoretic deposition: (a) side view and (b) top view.....	41

2-7	The sintering programs for synthesis of Ag-sheathed BSCCO films: (a)SINT9 for EPD and TMC films and (b)SINT31~34 for optimizing superconductivity and ACEPD films	45
2-8	The schematics of (a)the fabrication procedure and (b)the standard dimensions of Ag/BSCCO/Ag tape specimens for T-peel test.....	49
2-9	The schematic of specimen setup for SQUID magnetometer MPMS5S showing specimen surface perpendicular to the applied magnetic field.....	56
3-1	The plot of (a)c-axis texturing enhancement factor C_x , and (b)the c-axis to a-axis texture ratio as a function of the applied DC electric field strength, respectively, using suspension concentration 0.2 gram/liter of unmilled BSCCO powder.....	62
3-2	The schematic of dominant particle-geometry-preference-induced electric dipole moment associated with the long dimension of particle major faces for a platy BSCCO particle initially orienting at angle with respect to the applied DC electric field direction in dispersion solution.....	72
3-3	The schematic of plate-like BSCCO particle electrophoretic deposition with a-axis texturing enhancement by strong DC electric field.....	74
3-4	The inclined angle effect on particle texturing: (a) schematic of electrode configuration, and (b) the plot of C_x as a function of inclined angle i.e., particle major face texture reduction with decreasing inclined angle of the Ag substrate surface with respect to strong DC electric field direction.....	75
3-5	The plot of the DC electric field dependency of (a) normalized Lotgering factor, and (b)c-axis to a-axis texture ratio deposited from two different suspensions showing that the films deposited from lower concentration 0.2 gram/liter always have higher c-axis texture ratios than those from high concentration 1gram/liter.....	78
3-6	The schematic of the relation among the inter-particulate distance and the dipole-dipole interactions affecting re-orienting particle	

major face parallel to the applied electric field.....	80
3-7 The plot of (a) normalized Lotgering factor, (b)c-axis to a-axis texture ratio as a function of the applied DC electric fields using two 0.2 gram/liter suspensions of different average particle sizes.....	82
3-8 The c-axis texturing enhancement by the modified electrophoretic deposition with AC electric fields parallel to substrate surface at frequency 150 Hz and $E_{DC}=40\text{v/cm}$: (a) the c-axis texturing enhancement factor and (b) (0010) to (200) texture ratio versus the applied AC electric field.....	89
3-9 The schematic of platy BSCCO particle having their long dimension aligned with the dominant electric field in dispersion solution: (a) weak DC electrophoretic field, and (b) strong DC electrophoretic field.....	92
3-10 The plot of the c-axis texturing enhancement factor as a function of the applied AC electric field frequency at constant DC 40 v/cm and AC field strength 200 v/cm, using 0.2 g/lit. BSCCO particle dispersion solution with average particle size 0.98 μm	94
3-11 The schematic of the interaction between the field induced effective dipole and the applied AC electric field showing the angular switching nature of the dipole related to the resonant frequency for maximum a-axis alignment as averaging over the switching angles.....	96
3-12 The c-axis texturing enhancement factor as a function of the applied DC electric field for modified electrophoretic deposition at E_{AC} 300 v/cm, 60 Hz, using 0.2 g/liter BSCCO dispersion solution of 0.98 μm average particle size.....	97
3-13 The average deposition rate dependency on the applied AC electric field Strength at constant suspension concentration, particle size, AC field frequency, DC field, and AC/DC electrode gap.....	100
3-14 The zigzag migration model for AC electric field modified electrophoretic deposition of platy BSCCO particles.....	102

3-15	The schematics of platy BSCCO particle electrophoretic deposition with AC electric field assisted c-axis texturing enhancement.....	103
3-16	X-ray diffraction patterns of the green films prepared via: (a)DC field (40 v/cm) only ; and (b)AC electric field modified ($E_{DC}=40$ v/cm, $E_{AC}=200$ v/cm, 200 Hz) electrophoretic deposition	105
4-1	The uni-axial pressure effect on c-axis texturing enhancement factor of BSCCO thick films using samples with the same dimensions at room temperature.....	114
4-2	The schematic of consolidation enhanced c-axis texturing via platy particle slip mechanism for inter-particle micropore compaction in BSCCO films during uni-axial cold pressing: (a)before and (b)after.....	117
4-3	The schematic of high-pressure-produced particle bending and cracking: (a)before uni-axial pressing, and (b) pressed.....	118
4-4	The consolidation temperature effect on c-axis texturing enhancement factor C_x of hot pressed BSCCO thick films with the same dimension at constant pressure 500 MPa.....	120
4-5	The Differential Thermal Analysis curves showing the melting point and weight variation with temperature for $Bi_2Sr_2CaCu_2O_x$	121
4-6	The angular distribution of c-axis texture at two different temperatures: (a)the schematic of angular relationship for x-ray diffraction, and (b)the curves of c-axis texturing enhancement factor versus in plane angles of the BSCCO films with the same initial microstructure in as-deposited BSCCO thick films at room temperature 25°C and 400°C	127
4-7	Schematic showing the silver-margin-hindering effect on the film deformation along the short dimension of the tape during the uni-axial pressing:(a) cross-sectional view along short dimension, and (b) cross-sectional view along the long dimension without Ag margins.....	129
4-8	The SEM photographs showing the surface morphology of a cold pressed BSCCO thick film at 200 MPa, room temperature.....	131

4-9	The plot of c-axis texturing enhancement factor Cx versus two average particle sizes, 0.36 μm and 0.98 μm for the open and Ag-sheathed BSCCO thick films as-deposited and pressed at 200 MPa, 250C for 5 minutes.....	133
4-10	The plot of c-axis texturing enhancement factor versus BSCCO particle size for the samples with and without Ag sheaths for as-deposited and sintered stages, showing large BSCCO particle films and Ag-sheathed tapes always have higher Cx.....	136
4-11	The x-ray diffraction patterns for pre-sintering consolidated BSCCO thick films showing the fraction of randomly-oriented fine particle: (a) higher in small particle sized film and (b) lower in large particle size film.....	139
4-12	The schematic of fine BSCCO particles accommodated in the micro-pore experiencing less effective Ag-sheath thermal expansion shear stresses during sintering-assisted c-axis texturing.....	141
4-13	Scanning electron microscopy cross-sectional view of Ag/BSCCO/Ag tape.....	146
4-14	The x-ray diffraction patterns of peeled Ag/BSCCO/Ag tapes fabricated using BSCCO powders with average particle size of (a) 0.98 μm and (b) 0.36 μm	147
4-15	The T-peel test curves of Ag/BSCCO/Ag tapes of the 10 μm thick films with average BSCCO particle size of (a) 0.98 μm and (b) 0.36 μm	149
4-16	The Scanning Electron Microscopy fracture micrographs of Ag/BSCCO/Ag tapes fabricated using BSCCO powders with average particle size of (a) 0.98 μm and (b) 0.36 μm	151
4-17	The optical microscopic photographs showing BSCCO thin film formation (colorful area) at the Ag/BSCCO interface revealed from the openings of BSCCO thick films (black area).....	156
4-18	The T-peel test curve of the Ag-sheathed BSCCO thick film with 5 μm thickness prepared from 0.36 μm fine particle showing higher adhesion strength and better uniformity than those of 10 μm thick film.....	158

4-19	The T-peel test curve of Ag/(5 μm)BSCCO/Ag tapes fabricated via thermomechanical consolidation using BSCCO powder with average particle size of 0.98 μm	161
5-1	The x-ray diffraction patterns of peeled Ag-sheathed BSCCO thick films prepared by the same thermomechanical consolidation and sintering conditions and the electrophoretic deposition (a) with and (b) without AC-electric-field assisted c-axis texturing.....	173
5-2	The temperature dependence of (a)normalized magnetization, (b)critical current density, and (c) peak magnetization decreasing rates of Ag-sheathed BSCCO thick films prepared by electrophoretic deposition with and without AC-electric-field assisted c-axis texturing.....	174
5-3	The temperature dependence of (a) penetration field, H_{penet} , and (b) the H_{pen} decreasing rates for Ag-sheathed BSCCO thick films prepared by the electrophoretic deposition with and without the AC-electric-field assisted c-axis texturing.....	176
5-4	The magnetic field dependence curves of critical current density measured at different temperatures for the Ag-sheathed BSCCO thick films prepared by electrophoretic deposition with and without AC-electric-field assisted c-axis texturing.....	180
5-5	The normalized critical current density dependence on the applied magnetic field measured at different temperatures for the Ag-sheathed superconducting BSCCO tapes, prepared by electrophoretic depositions with (solid curves) and without (dashed curves) additional AC electric field assisted c-axis texturing.....	181
5-6	The magnetic hysteresis loops of peeled Ag/BSCCO/Ag tapes fabricated using BSCCO powders with average particle size of (a) 0.98 μm and (b) 0.36 μm	187
5-7	The room-temperature consolidation pressure effect on the superconductivity of the simultaneously sintered Ag-sheathed BSCCO thick films: (a)magnetic fields and (b)magnetization corresponding to the peak and penetration values in the magnetization hysteresis loops.....	194

5-8	The thermomechanical consolidation temperature effects on the superconductivity of Ag-sheathed BSCCO thick films, pressed at the 500 MPa for 1 hour and simultaneously sintered: (a) magnetic field & (b) magnetization corresponding to the peak and penetration values in magnetization hysteresis loops.....	198
5-9	The effect of thermomechanical consolidation temperature on the critical temperature transition ΔT_c for the samples prepared at the same pressure, holding time, and simultaneously sintering.....	199
5-10	The AC magnetic susceptibility χ' as a function of temperature of Ag-sheathed BSCCO-2212 samples (cut from the same tape) prepared by different two-stage sintering programs: (a) SINT31, (b)SINT32, (c)SINT33 and (d)SINT34.....	203
5-11	The magnetization hysteresis loops of Ag-sheathed BiSrCaCuO thick films with the same dimensions prepared by different sintering programs: (a)SINT32, (B)SINT33, and (c) SINT34.....	206
6-1	The schematic showing particle-geometry-preference-induced electric dipole moment formation in additional AC electric field modified electrophoretic deposition: (a) particle-electrode configuration, (b)electric forces cooperation, and (c)electric dipole formation.....	211
6-2	The plot of computer numerical simulation expressing platy BSCCO particle orientation behavior as a function of time in electrophoretic deposition at $E_{DC} = 40$ v/cm	216
6-3	The schematic showing the relation between electrophoretic deposition configuration and the simulation data plot of particle angular motion behavior with vibration axis:(a)parallel, (b)positively inclined, and (c)negatively inclined to the applied AC electric field orientation.....	220
6-4	The plot of computer numerical simulation expressing platy BSCCO particle orientation behavior as a function of time in modified electrophoretic deposition at $E_{DC} = 40$ v/cm, 200 Hz, $E_{AC} =$ (a)40, (b)100,(c)200, (d)300, and (e)500 v/cm.....	221

- 6-5 The plot of computer numerical simulation expressing platy BSCCO particle angular vibration motion behavior as a function of time in modified electrophoretic deposition at E_{DC} 40 v/cm, E_{AC} 200 v/cm, frequencies: (a)100, (b)200, (c)300, (d)400, (e)500, and (f)1000 Hz.....224
- 6-6 The plot showing the attenuated angular vibration amplitude of the platy particle as a function of applied AC electric field frequency obtained from Figure 4-22, and original angle at $\pi/2$ radian with respect to AC electric field.....225
- 6-7 The plot of computer numerical simulation expressing platy BSCCO particle orientation behavior as a function of time in modified electrophoretic deposition at E_{AC} 200 v/cm, 200 Hz, E_{DC} = (a) 0, (b)20, (c)40, and (d)200 v/cm227
- 6-8 The plot of DC electric field strength effect on the angular vibration motion behavior of platy particle at constant E_{AC} = 200 v/cm, 200 Hz at steady state: (a) time-averaged vibration orientation, (b)angular vibration amplitude, and (c)the time need to reach steady state, analyzed from simulation results in Figure 4-24.....228
- 6-9 The plot of computer numerical simulation expressing platy BSCCO particle orientation behavior as a function of time in modified electrophoretic deposition at E_{AC} 500 v/cm, 1000 Hz, E_{DC} = (a) 40 v/cm, and (b)20 v/cm231
- 6-10 The plot of computer numerical simulation expressing platy BSCCO particle orientation behavior as a function of time in modified electrophoretic deposition at E_{DC} 40 v/cm, E_{AC} 200 v/cm of 200 Hz and initial angles: (a) $\pi/6$, (b) $\pi/4$, (c) $3\pi/4$, and (c) $\pi/2$ with respect to E_{AC} 233

Abstract of Dissertation Presented to the Graduate School of
the University of Florida in Partial Fulfillment of the
Requirement for the Degree of Doctor of Philosophy

CHARACTERIZATION AND MICROSTRUCTURAL CONTROL OF SHEATHED
SUPERCONDUCTING BiSrCaCuO THICK FILMS BY AC-ELECTRIC-FIELD
ASSISTED ELECTROPHORETIC DEPOSITION

By

Cheng-Feng J. Yue

August 1998

Chairperson: Rajiv K. Singh

Major Department: Materials Science and Engineering

The goal of this research is to fabricate and characterize the Ag-sheathed BiSrCaCuO (BSCCO) tapes using a combination of alternating current electric field assisted electrophoretic deposition (ACEPD) and thermomechanical consolidation (TMC) technique. In this method, an alternating current (AC) electric field was applied in conjunction to the direct current (DC) electric field. This AC field parallel to substrate surface was found to assist c-axis texturing of BSCCO film.

Higher uni-axial pressure and temperature for thermomechanical consolidation enhance and reduce the size and number density of micro-pores. The effect of processing variables on the microstructure of BSCCO tapes was investigated in detail. The high AC field operating at high frequencies and low DC field were found to improve the c-axis texture. To improve the c-axis texture, several novel concepts were investigated in this research, namely, (i) AC-

assisted EPD and (ii) thermomechanical consolidation. Such improved green film microstructure led to better superconductivity stability. The introduction of Ag-particle interlayer into the middle of BSCCO film forms the strong two-dimensional Ag-BSCCO composite, leading to the improved fracture strength and adhesion.

T-peel fracture test, scanning electron microscopy, x-ray diffractometry, and SQUID magnetometry characterization results were correlated to c-axis texturing enhancement and BSCCO tape/wire processing parameters. The effects of superconductivity changes by pre-sintering microstructure control with thermomechanical consolidation parameters were discussed.

The AC field assisted electrophoretic deposition mechanism for c-axis texture enhancement was modeled by simulating the trajectory of anisotropic particle in suspension. Differential equations to demonstrate the angular motion behavior of the particle was developed. Good agreement was observed before the experimental results and numerical calculations.

CHAPTER I INTRODUCTION

The discovery of high critical temperature (T_c) superconductor (HTS) BaLaCuO by Bednorz and Müller in mid-1986 has opened a possibilities in applications involving transport of high critical current. Ultrahigh magnetic field can be only generated by applying tremendous amount of electric current through the solenoid, coil or toriodal coil. Normal electric conductors such as silver or copper have limited current capabilities due to their finite resistance. Cooled in expensive liquid helium, low temperature superconductors (LTS) can only operated at extremely low temperature such as 4 K. In contrast, HTS materials are able to operate above the 77 K, which is the boiling temperature of inexpensive liquid nitrogen. Unlike strong, flexible and isotropic LTS of simple metals or alloys, HTS materials are generally brittle and anisotropic ceramics of complex compounds with complicated crystal structure. The materials processing has been a challenge for making strong, flexible tape/wire for the practical applications. The key to the realization in numerous applications is development of textured microstructure which is discussed in detail in the following sections.

1.1 High Temperature Superconductor Tape/Wire

High- T_c BSCCO superconductor can be used in many applications, such as wires or tapes in electric power transport, electromagnet, motor, generator, magnetic energy storage devices, frictionless bearing, transmission lines transformer, and power electronic components,... etc. [Wu87, Sheng88, Hells92, Iri94, Bra95, Stakl95]. HTS tapes/wires with core of polycrystalline thick films should be capable of carrying high currents. However, they do not have the same level of performance and quality as that in single crystal forms. Polycrystalline HTS tapes/wires possess critical current densities which may be several order of magnitude less than obtained in single crystals ($\sim 10^6$ or 10^7 Ampere/cm²) or in epitaxial thin films. This is due to the lack of appropriate processing technology to control size, orientation and grain boundaries.

In magnetic applications, magnetic resonance imaging (MRI), Tokamak nuclear fusion reactor [Figure 1-1(a)], synchrotron radiation source, neutron accelerator, magnetic levitation transport vehicle (MLT) and electromagnetic thruster (EMT) [Figure 1-1(b)] have been being intensively studied [Osam94]. For electric applications, studies for potential applications in superconductor generator, direct electric energy storage, and transformer, etc. have been investigated. In the case of generators: metallic conductors can not used for carrying ultrahigh

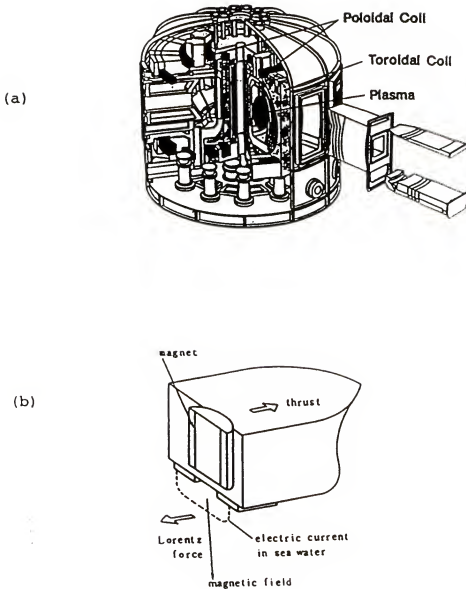


Figure 1-1 Examples of high- T_c superconductor tape/wire applications: (a) Tokamak nuclear fusion reactor and (b) electromagnetic thruster (EMT)

current density due to the resistive heating problem. As the thermal energy lost of resistive heating by cooling away is larger than that generated by the generator, the high power generator become energy consumption machine. For electromagnetic applications, HTS devices have been studied for transmission lines and in development of highly sensitive antenna capable of receiving extremely weak telecommunication signal. For global telecommunication applications, the ratio of noise to signal should be significantly reduced by using superconducting receiver. In electronic circuits for communication, the thermal electron can produce the electromagnetic noise. The superconductor circuits functions with highly sensitive receivability which affords the good quality of mobile telecommunication at any remote locations, and reduces the complication of satellite design for high signal output power. Superconductor linear motor has been considered for mechanical devices capable of high speed transport. Mass transport systems using electric power can reduce the air pollution produced by internal-combustion vehicles and the waste of natural resources in the Earth. In military underwater vehicle applications, the EMT systems provide quiet mobility and high acceleration capability for weapon platforms which gain many tactical and strategic advantages. The tape/wire winding types are summarized in Table 1-1 as planar(circular or rectangular) coil, solenoid, toroidal coil and poloidal coil for various applications. However, HTS for these applications are mostly

Table 1-1 The various winding forms of superconducting tape/wire for different electrical/magnetic applications.

	coil	solenoid	toroidal coil	poloidal coil
transmission line/antenna	yes			
Inductor		yes	yes	
current storage	yes			
motor	yes		yes	
generator	yes		yes	
MagneticResonanceImaging		yes		
electromagnet		yes		
MagneticLevitationTransport		yes		
Electromagnet Transport		yes		
Synchrotron Radiation Source			yes	
Neutron Accelerator			yes	
Transformer			yes	
Tokamat Fusion Reactor			yes	yes
Bearing	yes			yes

polycrystalline material, which so far do not have the same level of performance and quality as that in single crystal forms. This is due to the lack of appropriate processing technology to control size, orientation and boundary of anisotropic grains in order to improve the current transport property of superconducting thick films. All these applications require the superconductor materials in the forms of planar coil, solenoid, toroidal coil or poloidal coil.

1.1.1 High- T_c Superconductors

Among the high T_c superconductor, $YBa_2Cu_3O_{7-x}$ (YBCO, $T_c=95^\circ K$), $TlSrCaBaCuO$ (TSCBCO, $T_c=120^\circ K$) & $HgBa_2CaCu_2O_{6+x}$ (HBCO, $T_c=110^\circ K$) systems, and $BiSrCaCuO$ (BSCCO 2212 & 2223 phases, $T_c=85\sim 95K$ & $115^\circ K$, respectively) attract more attention of many researchers. However, YBCO has twinning and very oxygen sensitive problems. It is very difficult for TCBCO and HBCO systems to be processed due to toxic and volatile elements. The potential advantages of BSCCO system over popular YBCO system are higher T_c , higher critical current density, less reactivity with CO_2 or H_2O and no need of special oxygen treatments at intermediate temperature.

Polycrystalline HTS thick films, wires or tapes have been extensively studied since the discovery of HTS oxides [Wu87, Tabuc88, Malar90, Pau92, Kat92, Willi95, Iye95]. The zero resistance and high current carrying capability below the

critical temperature allows HTS to be used for electrical and magnetic applications. Among all coppers oxide based superconductor systems, Bi-Sr-Ca-Cu-O (BSCCO) has the highest critical temperature (T_C) reported to date (110 K for 2223 phase) without toxic or very volatile components in this complex compound system. BSCCO has higher T_C , less reactivity with water or CO_2 , and no requirements for special oxygenation treatment at intermediate temperatures; thus, it has potential advantages over the more popular Y-Ba-Cu-O system. The high T_C of BSCCO also means potentially high J_C which is useful in many applications.

Many thick film processing methods have been studied for the microstructure control of superconductors as YBaCuO and BiSrCaCuO systems [Greut90,Goy95,Li97,Non89,Coo88], since the discovery of HTS. BiSrCaCuO (BSCCO) powders is one of the promisingly superconducting material used in the thick film synthesis for tapes/wires fabrication. The microstructure control, in terms of arrangement of the superconducting particles, during the thick film synthesis is the basic one of the critical issues to obtain high J_C . Since BSCCO crystal possesses an extremely anisotropic structure and properties [Tomi92,Cardo93]. The BSCCO's J_C parallel to ab-plane is one order in magnitude higher than that perpendicular. BSCCO particle is plate-like in shape which the major faces are parallel to the ab-plane and the particle thickness is along c-axis direction. The granular texture is pertinently related to J_C , while superconductivity stability with respect

to temperature and magnetic field depend on the intergranular and intragranular structures. The improvement of superconductivity stability becomes the priority task to study. By appropriate fabrication technique, the enhancement of c-axis texture in green films should hold the key to improve J_c and superconductivity stability.

Silver substrates have been used in many HTS tape and wire fabrication due to high electric conductivity, thermal conductivity, and adequate mechanical strength. Ag does not chemically react with HTS oxide. Oxygen can diffuse through Ag cladding layer during heat treatment, and close oxygen diffusion as cooled down. It was suggested that the Ag particles can lower the reaction temperature [Griv94], reduce weak-link behavior [Gao90], enhance flux pinning [Savv91], and can change lattice parameter change [Wu94].

In practical environment, ambient gases and moisture exist everywhere which may chemically react with high critical temperature superconductor materials and eventually result in degradation of superconductivity. Preventing from environmental attack and contamination, the protection shielding of superconducting thick films via appropriate fabrication technique is important. Few research reports have emphasized the green film microstructure control for improving the film/sheath interface adhesion and film fracture strength of the metal-sheathed HTS superconducting tapes/wires/wires.

1.1.2 Polycrystalline Thick Film Synthesis

Many techniques have been studied for the fabrication of HTS oxide wires and tapes [Larb93, Rile94, Bhar95, Diet90, Wang95, Toms97]. In each method, processing-dependent properties are always pertinent to the microstructure. The transport critical current density is the most important measurement characteristic. The Oxide-Powder-In-Tube (OPIT) method has been used to produce BSCCO wires [Tenb90, Sand91, Larb93, Rile94]. In this method, oxide powder is filled into a metal tube, then the tube is sealed and drawn into a fine wire (shown in Figure 1-2). The drawing process can consolidate and texture the thick film. Repeated heat treatments after each drawing process to produce desired superconducting property are required, although it is costly processing technique. Intermediate annealing are often incorporated between successive deformation steps. The critical current density (J_C) of the multifilamentary wire made by this method were reported as 1.1×10^4 A/cm² at 77 K and 1 T magnetic field for (Pb)2223 based tape [Sato90]. However, the J_C was reported to be one order of magnitude lower at 77 K and 0.1 T for 2212-based tape [Enom90]. This method repeatedly needs mechanical working followed by heat treatment which results in "sausaging" and unstable quality. OPIT method uses mechanical force such as drawing for grain texturing which is only effective for the small region near the metal/HTS interface. The of c-axis texture in HTS thick

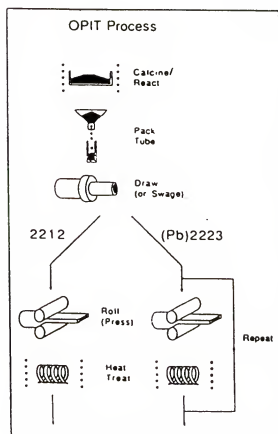
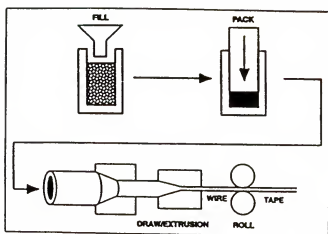


Figure 1-2 The schematics of general oxide-powder-in-tube fabrication processing schemes for HTS wires and tapes.

film core is still rather poor. High deformation can also introduce cracking in the HTS film which may not be healed by the following heat treatment.

Slip-casting [Bhar95] and doctor-blade-cast process [Diet90] have also been reported for the fabricating HTS oxide tapes. Similar to dip coating [Nona89], the slip-casting method has the tape/wire substrate slipping through the HTS powder slurry, thus the green film is coated on the tape/wire. After the organic solvent is dried out from the green film, sintering processing follows. The sintered tape/wire is then sheathed with the other metal tape. The tape/wire is finally consolidated and annealed. The resulted particle texture is similar to that of randomly-oriented bulk ceramics. The film thickness uniformity control is a challenging task in this technique. Using a flat-edge blade scratching over the slurry on tape surface to form a film, the doctor-blade-casting technique may have relatively better control in film thickness and particle texturing. Screen printing technique [Hornu93] has been combined with cold deformation and sintering to produce superconducting tapes. The HTS powder slurry is printed through a thin clothing screen of fine mesh size by a flat-edged blade. However, these techniques require a large amount of organic binders or plasticizers (e.g., 40 wt%) added to HTS to provide the plasticity for fabrication. These organic additives can not be completely burned out during sintering, without vaporization of volatile component like Pb. These residual

carbon and Pb loss are detrimental to the densification, texturing and composition control. Furthermore, the sintered film microstructure consists of large amount of micro-pores.

For similar reasons, the aerosol spray pyrolysis approach [Ward92,Wan95] using dilute slurry of HTS powder to make Bi-2223 tapes is not be suitable for making textured films. The resulting aerosol powder is spherical assembled by randomly-oriented HTS particles. Similarly, the spray pyrolysis of nitrate precursors solution [Coop88] has not found to fabricate high quality HTS films due to formation of mixed phases .

A "continuous tube filling and forming" (CTFF) process was studied to make BSCCO tapes by Tomsic et al [Toms97]. Superconductor powder was feed onto the silver tape between two reels, then the Ag strip is U-forming rolled into a tube. The third stage is U-closing rolling followed by wire drawing. It was regarded as a low-cost BSCCO tape process. Since repeatedly mechanical working and sintering were used in this process technique, the similar drawbacks in OPIT technique can also occur in CTFF technique. Viewed from SEM micrographs, the Ag/BSCCO interfaces are not very smooth. The texturing control is only based on the mechanical rolling process. The critical current density J_c at 77K was 2000~2200 A/cm².

Electrophoretic deposition (EPD) has also been developed as available method for deposition of superconductor particles [Sark91, Ho91, Kao93]. BSCCO particles can be

continuously [Woolf95] deposited on Ag substrates by DC electric field in suspension solution. The suspension solution is made by mixing HTS particle and organic solvent (e.g., ethanol) via ultrasonication. The particles are consolidated during electrophoretic deposition via the interaction between the electric dipole moment (associated with particle surface charge) and the applied electric field, in contrast to the mechanical forces used in OPIT technology. The particle coating thickness and deposition rate can be controlled through the conditions of EPD and suspension solution. Complicated shapes had been coated with ceramic thick film using EPD technique. This method can also be used for micro-laminating multilayered thick films with controlled microstructure. Samples at each stage are available for the non-destructive in-situ microstructural characterization. The ethanol in the as-deposited films can be easily dried in the air thus minimizing foreign contamination.

Electrophoretic deposition is a clean and microstructure controllable material synthesis method for ceramic thick films [Hamak40, Sarka92, Sarka94, Ryan79]. More researchers used this technique for BSCCO film deposition followed by consolidation [Gui88, Nash92], sintering [Wu87] or melting growth [McGinn89, Jin88, Salama89]. Micro-lamination of ceramic powders had been successfully used to coat on complicated shape body. However, so far, few research consider using EPD method for the green film microstructure control such as particle orientation control in order to fabricate highly c-axis

textured BSCCO films. Such green film microstructures are believed to reduce particle cracking and bending during consolidation. Not even thought of EPD for Ag particle interlayer coating to form two-dimensional composite before, such modification of BSCCO film microstructure is believed not only to re-enforce the mechanical characteristics of Ag-sheathed HTS thick films, but also to avoid blocking supercurrent transport by normal conductor silver.

Using electrophoretic deposition method, silver particle interlayer can be introduced into the HTS film to form virtually two-dimensional composite for improving the mechanical characteristics of the tape/wire. The thickness of Ag film can be fine-scaled controlled by the conditions of EPD and Ag particle suspension solution.

1.1.3 Arrangement and Boundary of Anisotropic Grains

HTS single crystal or bicrystal junction studies have revealed that the orientation arrangement and boundary of anisotropic HTS grains determine the critical current density of the superconducting tape/wire. Studies on single crystals and in the polycrystalline thick films have shown that the intragranular critical current density along ab-plane is higher than that in c-axis direction [Welp89]. The BSCCO crystal structure is shown in Figure 1-3. Studies have shown that the intergranular critical current density decrease with increasing degree of misorientation. All types of grain

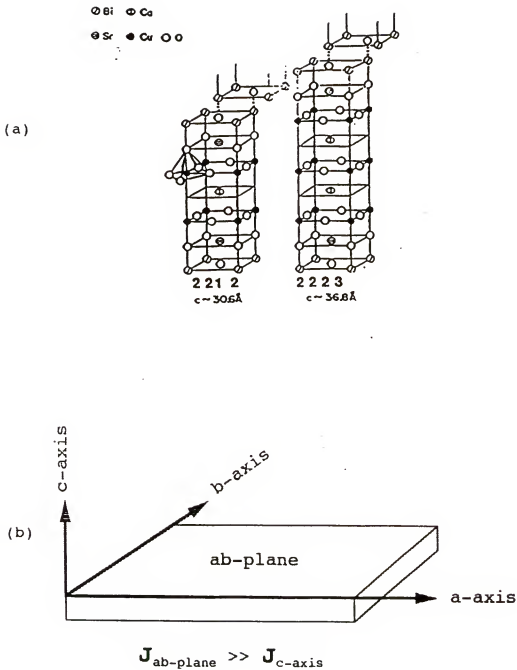


Figure 1-3 The schematics of high temperature superconductor BiSrCaCuO 's (a) crystallographic structures and (b) the anisotropy in particle shape and superconductivity.

boundaries generally decrease critical current density with misalignment angle up to 20° [Chaud87, Manh88, Dimos88&90], except for certain high-angle grain boundaries, owing to coincidence site lattices [Tomi92]. Regarding the major faces of plate-like grains as the dominant mechanism for transport J_c , the "brick wall" model was proposed for the microstructure-superconductivity behavior of HTS polycrystalline films [Bula92]. The (001) twist boundaries are considered as the major current paths according to "brick wall" model, while the most frequently observed small-angle c-axis tilt boundaries are regarded as main intergranular transport current paths in "railway switches" model [Hens93,95]. Thus, superconductive properties can be related to film microstructure features, such as grain size, orientation, and boundary morphology (tilt or twist types).

By mechanical working, the particle deformation defects such as broken, cracked and bent particles/boundaries in the superconducting thick films can cause the interruption of supercurrent and weakening of superconducting coupling [Yuh95, Ekin92, Yau94, Li97] which can thus reduce the critical current density and its stability under the temperature and magnetic field changes. These particle deformation defects in pre-sintering thick film microstructure are mainly produced by the mechanical processes. Post-sintering mechanical working can introduce more such grain deformation defects. Sintering and annealing can not completely eliminate such defects.

1.2 Motivation and Objectives

As previously mentioned, the enhanced c-axis texture arrangement and strongly coupling ab-plane boundaries with reduced microcracking and bending are the keys to improve the thick film microstructure for high critical current density. The c-axis texturing enhancement during the particle deposition, and the particle film consolidation without significant mechanical working should be achieved by pre-sintering processes. The development of the technique for particle orientation control during the electrophoretic deposition is the fundamental study for the successful pre-sintering processing. The theoretical study of such technology can lead to further improvement in this technology.

Besides, this pre-sintering processing should be compatible to the introducing processes of fine silver particle interlayer for forming multilayered superconducting composite tape/wires with stronger fracture strength. How the BSCCO particle film conditions affect on the film fracture strength is a significant issue to make strong sheathed tapes.

In addition, surface passivation of BSCCO films for protection from environmental attack is an important task. As the shielding material, silver sheath can protect superconducting oxides from chemical reactions with moisture

and CO₂ in the environment, and from the contamination during mechanical working and thermal processing. It is critical to study the factors influencing the adhesion of Ag sheathes and BSCCO film and the fracture strength of the sheathed thick film. It is important to understand how well the silver sheathing can be integrated into the fabrication of Ag-sheathed superconducting composite tapes/wires with controlled BSCCO film microstructure. To solve the above problems in making superconducting tape/wire practical, the research motivation then were brought up.

With the above motivation in mind, the objectives of this study can be described as the following:

- (i) To study a novel combination of AC-electric-field modified EPD and TMC processes to fabricate Ag-sheathed tapes by controlling the microstructure of BSCCO prior to thermal sintering. Then enhanced c-axis texture in the green microstructure is expected to lead to better superconducting properties. A schematic diagram to the processes involved in formation of the tapes is shown in Figure 1-4;
- (ii) To study the Ag sheathing process for protecting the BSCCO thick films from environmental attack and contamination;
- (iii) To investigate the fine silver particle interlayer processing for strengthening the BSCCO thick films and multifilament fabrication.

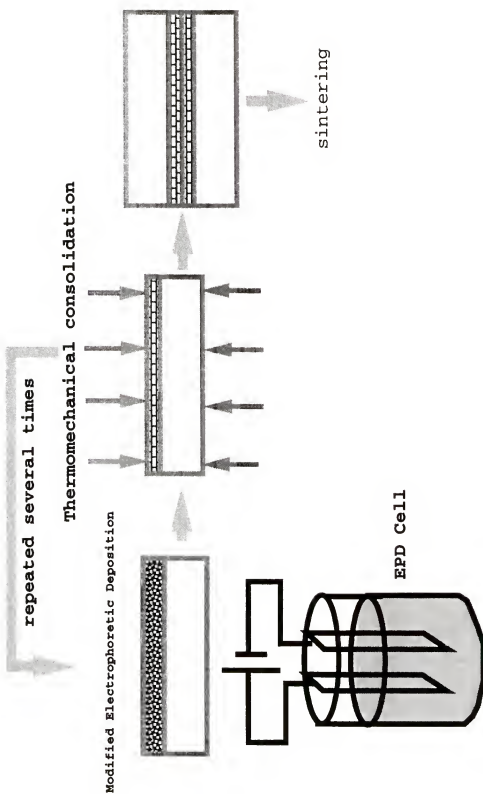


Figure 1-4 Schematic of sequential micro-lamination of electrophoretic deposition method and thermomechanical consolidation for Ag-shaeathed superconducting BSCCO tapes fabrication.

- (iv) To study AC electric-field assisted electrophoretic deposition technique for c-axis texturing.

1.3 Outline of This Dissertation

In this dissertation, Chapter I states the research motivation and objectives for this research, and provides background information about HTS tape/wire applications. It also reviews the literature reporting the fabrication techniques of polycrystalline HTS thick film in tape/wire, and the microstructure-property correlations of bicrystal studies, emphasizing HTS anisotropy.

Chapter II depicts the experimental approach to study microstructural controllability of Ag-sheathed BSCCO thick films. The experimental control factors are defined for each experiment. The superconducting tape/wire fabrication procedures were described in detail. The characterization methods are stated for microstructure, fracture, and grain texture using scanning electron microscopy, x-ray diffractometry. A modified Lotgering factor is used to evaluate the c-axis texturing enhancement factor for each major processing stage. The mechanical characterization and specimen setup employed in this study is described for T-peel test. For superconductivity characterization, magnetic measurement methods are discussed in terms of magnetization hysteresis loops and AC magnetic field susceptibility at

different temperature and applied field on the fully processed tapes/wires.

Chapter III presents the experimental results and discussion about the additional AC-electric-field modified electrophoretic deposition for c-axis texturing enhancement. The dependence of c-axis texturing on the controllable processing parameters were characterized from reproducible results of experiments. All possible physical forces acting on the BSCCO particles in suspension solution during EPD were considered and discussed in detailed calculations. The dominant mechanism for plate-like BSCCO particle orientation was modeled based on the interaction between the applied electric force and the induced electric dipole moment associated with BSCCO particle geometry. DC electric field dependency of c-axis texturing was investigated prior to AC field assisted texturing using EPD. Applying the knowledge learned from DC experiments, the ACEPD study was then conducted. From these experimental results, a physical model of the plate-like particle motion behavior was developed to explain the observed phenomena was analytically described.

Chapter IV systematically presents the post-deposition processing parameter influences on c-axis texturing control of green BSCCO films, and on the resultant superconductivity of sintered tape/wire. Following EPD, the c-axis texturing enhancement mechanisms by thermomechanical consolidation and sintering are illustrate to discuss. The influence of particle size, film geometry, silver sheath on c-axis texture

enhancement were also discussed. Mechanical characterization was reported mainly considering silver particle interlayer effect on Ag/BSCCO/Ag tape strengthening.

The superconductivity characterization is discussed in Chapter V. The superconductivity stability improvement by AC-electric-field assisted electrophoretic deposition is presented and related to the reduced particle deformation defects and the enhanced c-axis texturing of as-deposited films. The stability is evaluated by the superconductivity dependence on temperature and applied magnetic field strength. The influence of experimental control factors on superconductivity was discussed considering particle size/aspect ratio, consolidation parameters, and sintering conditions. The superconductivity are characterized in terms of the dependencies of peak magnetization, peak magnetic field, penetration field and hysteresis loop shape on processing parameters.

Chapter VI discussed and modeled the c-axis texturing enhancement mechanisms by the additional AC electric field assisted electrophoretic deposition, considering EPD parameters, suspension condition and electrode configuration. A physical model about angular motion behavior of particle-geometry-preference-induced electric dipole associated with a plate-like particle, influenced by dual electric fields (DC and AC) in suspension solution was derived to explain the observed results by computational simulation results.

Finally, the conclusions of this work and the future research will be presented in Chapter VII.

CHAPTER II EXPERIMENTAL APPROACH

2.1 Introduction

The experimental works in this study involve (i) electrophoretic deposition of $\text{Bi}_2\text{Sr}_2\text{CaCu}_2\text{O}_x$ (BSCCO) thick films, (ii) thermomechanical consolidation of the sheathed tape/wire, (iii) heat treatment for the consolidated tape/wire, and (iv) property measurements.

Based on the processing controllability, the considered factors to enhance c-axis texture were (i) particle aspect ratio control, (ii) inter-particulate interaction, and (iii) the flux density, parallelism and orientation of the applied electric field. In turn, these factors can be controlled by (i) particle size, (ii) suspension concentration, (iii) applied electric field strength and (iv) electrode configuration. The resultant microstructure of the pre-sintering thick films was then characterized by x-ray diffractometry (XRD), scanning electron microscopy (SEM). In this work, two unique electrokinematic mechanisms were considered to control the particle orientation to be deposited on substrates. They are related to the dispersed particle shape effect and the dipole-field interactions: (i) particle-geometry-preference-induced electric dipole moment associated with extended electric double layer surround a plate-like BSCCO particle

and (ii) the angular motion behavior of plate-like BSCCO particles due to complicated interactions between this induced electric dipole and the applied AC/DC electric fields.

In the BSCCO thick film adhesion characterization, the T-peel test was carried out for the adhesion strength comparison between tapes with fine-particle films and coarse-particle films. Fine silver particle interlayer was introduced into the middle of the BSCCO film to enhance the adhesion and fracture strength of the tape. The adhesion between Ag/BSCCO and the fracture strength of BSCCO films were studied concerning film thickness. Considering processing parameter effect, thermomechanical consolidation effects on BSCCO/Ag interface adhesion strength and BSCCO fracture strength were also investigated. To confirm the adhesion strengthening effect, all fracture of the peeled tapes were examined whether the de-adhesion of Ag/BSCCO interface occurs or not.

Magnetic characterization was used for evaluation of superconductivity such as critical current density based on Bean critical state model^[Bean63]. The peak magnetization, the corresponding magnetic field, and the penetration field can be measured from the magnetization hysteresis loop. To compare the c-axis texturing enhancement by ACEPD, the dependencies of critical current density and penetration magnetic field strength on temperature and the applied field were measured.

2.2 Sequential Micro-lamination of Electrophoretic Deposition and Thermomechanical Consolidation

This HTS film processing method is schematically illustrated in Figure 1-3. First, BSCCO particle film layer was deposited on Ag tape by EPD for 10 minutes, and thermomechanical consolidation (TMC) was then conducted on this layer at 200°C, 200 MPa for 10 minutes.

X-ray diffractometry can be conducted on the BSCCO film for c-axis texture evaluation. In the next stage, the consolidated film was used as the substrate for the second EPD of the same condition, then followed by the same TMC process. Repeating the above processes, the thick film of 10 μm can be built up with microstructure control. Finally, the second Ag sheath was placed on the film by the same TMC condition.

Using the optimized processing parameters for c-axis texturing enhancement, the EPD and ACEPD techniques were applied to make Ag-sheathed HTS tapes, respectively. Then both tapes were heated treated by the sintering program SINT34: heating ramp rate 300°C/hour, 870°C for 0.5 hour, slow cooling rate 2°C/hour, 840°C for 24 hours in the air, then quenched in ethanol. Both deposition methods had the same DC condition: E_{DC} 40 v/cm, and DC electrode separation 1.5 cm. In ACEPD, the E_{AC} is 200 v/cm at 150 Hz, AC electrode separation 6 mm.

2.3 Preparation of Superconductor Powder Suspension

Superconductor BSCCO powder suspensions were prepared from commercial $\text{Bi}_2\text{Sr}_2\text{CaCu}_2\text{O}_8$ (BSCCO-2212) powder manufactured by Superconducting Components, Inc. The average particle size of the as-received powder was $0.98\text{ }\mu\text{m}$.

For obtaining controlled EPD films, the stability of BSCCO suspension solution was studied, using the ZetaPlus Particle Analyzer. The Zeta potential of BSCCO particles in ethanol indicates the stability of the suspension solution. The high Zeta potential ($>25\text{mV}$) is generally indicative of stable suspensions. ICP (Inductively Coupled Plasma) studies were also conducted to determine the leaching effects in the solution. The chemical stability of BSCCO particle surface was analyzed by detecting the cation concentrations in the ethanol medium.

A powder of average particle size $0.36\text{ }\mu\text{m}$ was prepared by ball milling as-obtained BSCCO powder ($0.98\text{ }\mu\text{m}$ particle size) in ethanol medium with zirconia balls for 240 hours[Ichin88]. The ball milling process primarily breaks the major faces of BSCCO particles into smaller faces, whereas the thickness of particles basically remains the same in the order of 100 nm . The Plate-like nature of BSCCO particles is shown in Figure 2-1. Thus, reducing particle size is equivalent to decreasing the aspect ratio of particles. Two suspension concentrations, 1.0 and 0.2 gram/liter were used to represent the high and low concentrations, respectively.

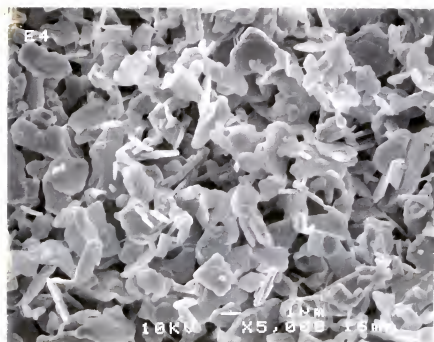


Figure 2-1 The Scanning Electron Microscope microphotograph showing the platy geometry of BSCCO particles.

To prepare a suspension, the BSCCO powder was accurately weighed, and then dispersed in ethanol using ultrasonication bath operating at low power. The output power of Fisher's ultrasonication generator was kept constant. The temperature of the bath was maintained at 18°C. Ice cubes were placed into the water bath for cooling the suspension, since the ultrasonication generates heat. A thermometer was used to monitor the suspension temperature. After ultrasonication, electrophoretic deposition was immediately conducted.

Four set of suspensions were prepared for the experiments. They are: (i) 0.2 gram/liter of average size 0.98 μm , (ii) 1.0 gram/liter of average size 0.98 μm , (iii) 0.2 gram/liter of average size 0.36 μm , and (iv) 1.0 gram/liter of average size 0.36 μm .

2.4 Modified Electrophoretic Deposition

At the initial stage of the c-axis texturing effect study by electrophoretic deposition technique, the strength and orientation of the applied DC electric field, DC electrode configuration and suspension conditions were first considered for particle orientation controllability investigation. The second stage was to investigate the additional AC electric field effect on c-axis texturing enhancement. The AC field was applied near and parallel to the substrate surface. In this study, the strength and frequency of AC electric field were used as the control

factors. In the following sub-sections, the experimental are described.

2.4.1 Particle Orientation Controllability by EPD Parameters

C-axis texture fraction in the as-deposited film was measured by x-ray diffractometry to determine the effect of various EPD condition on c-axis texturing, via affecting the major face orientation of plate-like BSCCO particles migrating toward the substrate. In this set of experiments, the electrophoretic deposition parameters, such as DC electric field strength (5~100 v/cm), substrate orientation (0~90° with respect to anode), suspension concentration (0.2 and 1 g/liter) and the average particle size (0.36 and 0.98 μm) of suspensions were used as processing control factors, while electrode configuration, EPD time and suspension temperature were kept constant. In each EPD experiment, only one of these parameters was changed.

The experimental setup used for preparing the BSCCO thick film consists of an electrophoretic deposition cell with in-situ voltage and current monitoring, substrate holder, and a height-adjustable stage shown Figure 2-2. A voltammeter was connected in parallel, and a high accuracy ammeter was connected in series with the electrophoretic deposition circuit. The DC electric field was applied between

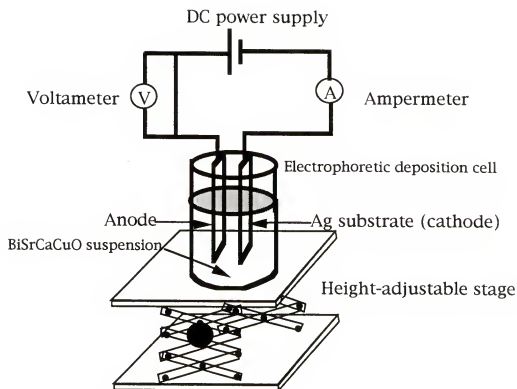


Figure 2-2 Schematic of electrophoretic deposition setup with in-situ monitoring capability of applied voltage and current.

two vertically parallel electrodes. One of the electrode is the substrate. The DC power source (EC Apparatus Corporation's EC-400) is only operated at the constant voltage mode in conducting EPD experiments.

In c-axis texturing enhancement evaluation, a normalized c-axis texturing factor designed as " C_x " is used to compare the c-axis texture fraction of textured films with that of random powder sample:

$$C_x = P/P_o \quad (2-1)$$

which P = the ratio of the sum of (00L) peak intensities to that of all peaks for the textured films as

$$P = [\sum I_{(00L)} / \sum I_{(HKL)}]_{\text{textured}} \quad (2-2)$$

and P_o is the ration for randomly-oriented powder sample as

$$P_o = [\sum I_{(00L)} / \sum I_{(HKL)}]_{\text{random}} \quad (2-3)$$

The concept was alternatively derived from Lotgering factor and was used to evaluate the c-axis texture fraction [Lotger59, Li97]. The resultant c-axis texture ratios with respect to the a-axis texture was represented as x-ray peak intensity ratio of $I(0010)$ to $I(200)$. They were plotted as a function of the controlled EPD condition.

2.4.1.1 Substrate Configuration Condition

In this experiment, the c-axis texturing enhancement factor C_x was measured on two sets of BSCCO green films deposited by EPD, using one bare Ag substrate and one dielectrically shielded Ag, respectively. The dielectrically shielded substrate holder was specially designed for this set of experiments as shown the Figure 2-3. Only one face of the silver tape was exposed to the suspension solution, i.e., the back and the edges (0.5 mm width) of the Ag tape were covered by dielectric glass slices. These dielectric shields were made of glass slices glued by epoxy to prevent any penetration of ethanol in between the electrode and glass slices.

Figure 2-4 shows the dielectric shields and electrode configuration can improve the electric flux parallelism. The results were plotted together in Figure 3-8 (a).

2.4.1.2 DC Field Strength Effect

In this EPD experiment, C_x was measured on the BSCCO films deposited at different DC electric field strengths (10, 30, 55, and 100 v/cm), while the other control factors were kept constant. The substrate is connected at the cathode. Suspension of 0.98 μm average particle size and 0.2 g/liter was used. The particle's major face alignment orientation in suspension determines the deposited texture.

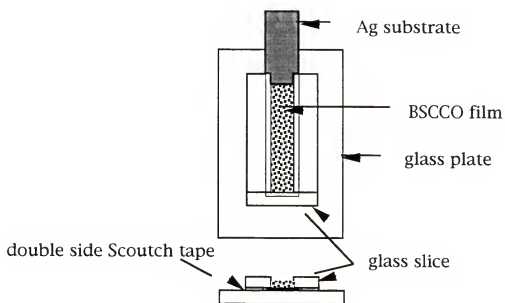


Figure 2-3 Schematic of the substrate holder for electrophoretic deposition experiments with glass dielectric shields that allows only one face of substrate exposed to dispersion solution.

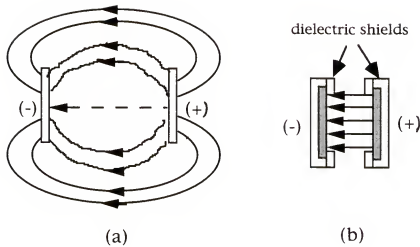


Figure 2-4 Schematic of electrode configurations: (a) far-apart electrodes without dielectric shielding over the near-edge area showing less electric flux parallelism; (b) closer electrodes with dielectric shielding showing better electric flux parallelism.

2.4.1.3 Electric Flux Incident Angle Effect

BSCCO films were deposited on the substrates orienting at different horizontal angles. These angle between the substrate (cathode) surface and the anode surface changed from 0° , 30° , 60° and 90° as shown the schematic of Figure 2-5. The C_x was measured and plotted versus these tilt angles. This experiment was designed to further confirm the associated texturing effects by the alignment of E_{DC} -induced particle-geometry-preference dipole moments along the applied electric field.

2.4.1.4 Influence of Interparticulate Separation

Two sets of $0.98\ \mu\text{m}$ particle sized suspensions with concentrations $0.2\ \text{gram/liter}$ and $1.0\ \text{gram/liter}$ were used for the DC field strength dependency of thick film texturing study. C_x of the as-deposited films was determined and plotted versus E_{DC} . The high suspension concentration stands for high inter-particulate interaction or short interparticulate separation in BSCCO suspension.

2.4.1.5 Influence of Particle Size

This set of experiments is designed to observe the texturing effect of particles in two suspensions with different average particle sizes, $0.98\ \mu\text{m}$ and $0.36\ \mu\text{m}$, which represent two different average aspect ratios of BSCCO particles. The electrophoretic deposition conditions were the same as those for the experiments of texturing dependency on

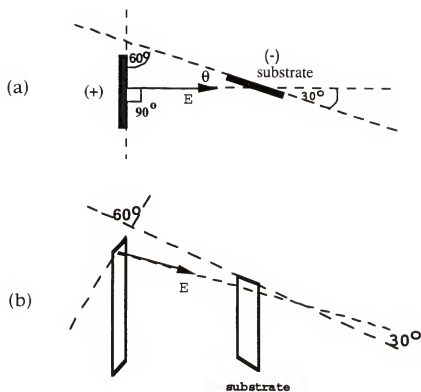


Figure 2-5 Schematic of the substrate orientation experiment: the horizontally tilted substrate with respect to the other electrode. (a) top view, and (b) perspective view.

DC electric field strength. From the films deposited in suspensions of two different particle sizes, the C_x dependency on E_{DC} was determined to plot.

2.4.2 C-axis Texturing Enhancement by Additional AC Electric Field Parallel to Substrate Surface

Based on the results from the previous experiments, the electrophoretic deposition was modified by applying an additional AC electric field parallel to the substrate surface (ACEPD) to enhance c-axis texture of plate-like BSCCO particles. The AC power supply used in the experiments is Accurate AC Power Source from Triathlon Inc. The maximum output voltage is 200 volts and frequency 270Hz. Suspension conditions was kept constant. For better orientation controllability, the average particle size $0.98\ \mu\text{m}$ of BSCCO powder was chosen, and the suspension concentration was 0.2 g/liter. Alternative current (AC) field was employed to prevent the deposition of BSCCO particles on the AC electrodes. The c-axis texturing enhancement factor C_x and the ratio of x-ray diffraction intensity peaks $I(0010)/I(200)$ was measured from the ACEPD films which was deposited at different AC electric field conditions, such as field strength E_{AC} (0~300 v/cm), frequency (60~250 Hz), and the E_{DC} was kept at 40 v/cm for most of the experiments (except for DC effect experiment on ACEPD). ACEPD time was 50 minutes for each experiment. Electrode configuration was kept constant as

AC/DC electrode gap of 2.5 mm, DC electrode separation of 1.5 cm, and the AC electrode length of 2.5 cm.

In AC field strength effect experiment, the C_x and the $I(0010)/I(200)$ ratio were measured from the ACEPD films prepared at $E_{AC}=10, 30, 50$ and 100 v/cm at constant frequency 150 Hz. For AC field frequency effect experiment, the C_x and $I(0010)/I(200)$ ratio were measured at E_{AC} 200 v/cm for different frequency $50, 100, 150$, and 200 Hz. The average deposition rate by ACEPD was also determined at different $E_{AC}=100, 200$ and 300 v/cm, while E_{DC} was kept at 40 v/cm. In DC field strength effect experiment, the C_x was measured at different $E_{DC}=20, 30, 40$, and 50 v/cm with constant AC condition (300 v/cm, 60 Hz).

The average deposition rate was determined from the film deposited at different AC electric field strength: $0, 100, 200$, and 300 v/cm at 150 Hz and E_{DC} 40 v/cm. The average deposition rate [gram/(cm².minute)] of the BSCCO thick film was calculated based on the weight and area of film, and deposition time. The weight of each silver tape was measured before and after the electrophoretic deposition. The weight difference was taken as the BSCCO thick film weight on a certain shape and area. The thick film geometry and area were determined by the dielectric insulation shielding mask.

In the next section, the electrode configuration experiment method was described considering the improved electric flux parallelism, and the gap between the AC and DC electrodes.

2.4.3 Electrode Configuration for Uniform Electric Field

In addition to the substrate holder with dielectric shields, a pair of vertically parallel AC electrodes were equipped to the holder close to the substrate surface shown in Figure 2-6. Both pair of electrodes were dielectrically insulated from each other. As shown in the schematic, the AC electrodes also were dielectrically shielded, and only exposed their parallel faces to each other. The gap, $|e|_{AC/DC}$, between AC electrode and substrate in most of experiments was 2.5 mm shown in Figure 2-6. The ratio of AC electrode width to the inter-electrode gap was also kept constant. This ratio influences the particle orientation control for c-axis texturing. The homogeneity and parallelism of AC electric flux are improved, as the width-to-gap ratio is higher [Purce65]. Depicted in Figure 2-6, the ratio is designed as W/d , which d is the gap width of parallel AC electrodes. AC/DC electrode gap is 2.5 mm, DC electrode separation is 1.5 cm, and the AC electrode length is 2.5 cm.

2.5 Thermomechanical Consolidation Assisted Texturing

The effects of (i) uni-axial pressure and (ii) temperature on c-axis texturing enhancement factor C_x were studied in two sets of film consolidation experiments. These

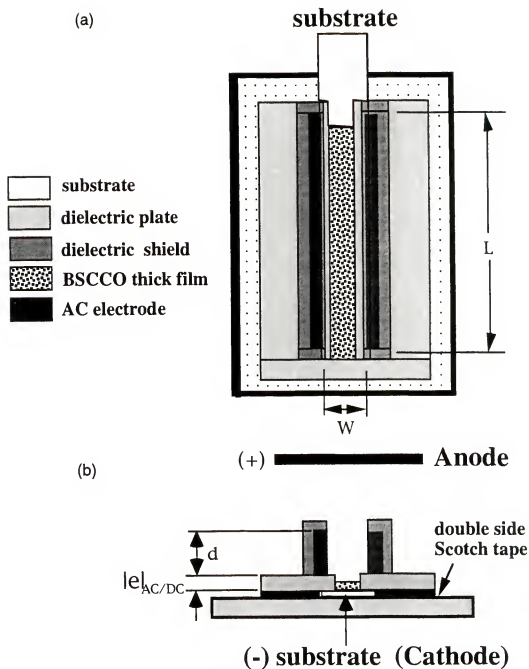


Figure 2-6 Schematic of substrate holder with the AC electrodes for c-axis texturing enhancement experiments by additional AC electric field modified electrophoretic deposition: (a) side view and (b) top view.

square specimens of the same area 0.25 cm^2 were cut from the open film tape. The tape was prepared using the EPD conditions: 1 g/liter, $0.98 \text{ }\mu\text{m}$ particle size, 100 v/cm, 50 minutes, resulting in the highest a-axis texture ratio. The smooth surfaces of both pressing dies were polished by $0.25 \text{ }\mu\text{m}$ abrasive. Especially during heat pressing, the press machine load on the pressing dies was consistently monitoring to keep at designated value. In the next sub-sections, the TMC parameter effect on c-axis texturing enhancement is described in detail.

2.5.1 Uni-axial Pressure Dependency

Three square open BSCCO film specimens cut from the same tape were uni-axially pressed at the pressures of 132, 264, and 528 MPa at room temperature for 1 hour, respectively. To ensure the uniform pressing on the thick films, the two surfaces of both pressing dies were carefully examined to be parallel to each other during all pressing.

2.5.2 Consolidation Temperature Dependency

The heating temperatures applied in this set of experiments were room temperature 25°C , 100°C , 200°C , and 400°C , while the uniaxial pressure was the same as 300 MPa, and the holding time period was 1 hour. The heat was generated by resistive heating elements within the pressing

blocks, and conducted through the pressing dies. After the thermomechanical consolidation, the pressing dies were quenched by water. The temperature of samples was dropped down to 35°C in 5 minutes. Before sintering, one set of the consolidated samples were taken for x-ray diffractometry. The c-axis texturing effect then was analyzed to compare the heating temperature effect on the c-axis texturing enhancement of green films. The other set of samples was Ag sheathed, i.e., the other silver strip was used to clad the BSCCO thick film then for pressing. After sintering at the same conditions, the Ag-sheathed samples were run T-peel test for tape adhesion strength characterization. Where the fracture was located can indicate if the adhesion strength of Ag/BSCCO interface is strong enough or not.

The critical current density J_c of these sintered samples were measured using SQUID magnetometer. The J_c , penetration field strength and peak field strength were determined from the resulting magnetization hysteresis loops. All these magnetic properties then were plotted as functions of consolidation temperature.

2.5.2.1 Angular Distribution of C-axis Texturing

Two specimens with the same dimensions were pressed at the same consolidation condition at different temperatures, then XRD was performed along three in-plane orientations, $\phi = 0^\circ$, 45° and 90° from the long dimension of each BSCCO film. C_x

values were recorded to plot the C_x as a function of ϕ . Ag margins were oriented along the long dimension of BSCCO film. The angular dependence of c-axis texturing enhancement factor for such a specimen configuration is important in microstructural uniformity control of real polycrystalline superconductor tape fabrication. The origin of the resulting angular dependence was discussed considering particle orientation behavior under the uniaxial pressure in the polycrystalline thick films.

2.6 Sintering Enhanced C-axis Texturing

Sintering processing is expected to further densify BSCCO film microstructure with higher c-axis texture fraction. Particle size and silver sheath effects on sintering texturing enhancement will be investigated. The sintering program designed in this study was schematically shown in Figure 2-7.

2.6.1 Green Film/Tape Condition Influences

2.6.1.1 BSCCO particle size influence

Using the same sintering program, the c-axis texturing of different average BSCCO particle sizes (0.98 μm and 0.36 μm) was investigated in the first set of experiments; the other set of experiments was designed to observe the silver sheath effect on c-axis texturing, after the tapes were peeled by Instron Universal Tester. The pressing conditions

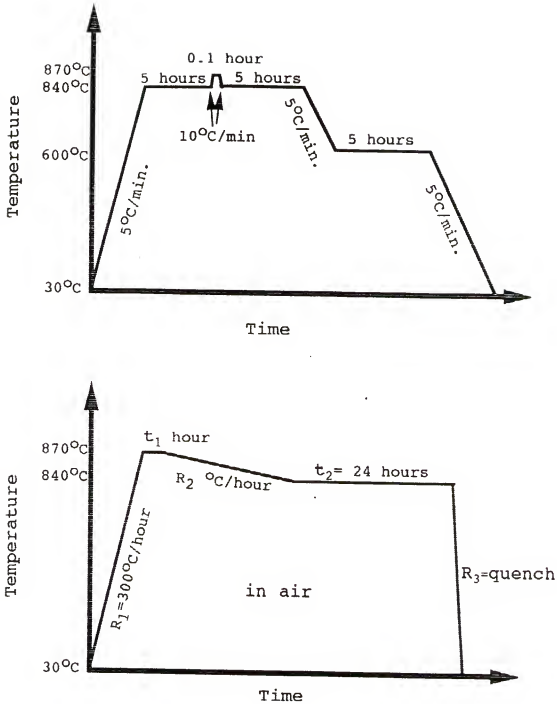


Figure 2-7 The schematic of sintering programs for synthesis of Ag-sheathed BSCCO films: (a)SINT9 for EPD and TMC films and (b)SINT31~34 for optimizing superconductivity and AMEPD films.

(200 MPa, 25°C, 5 minutes holding) and sample dimensions (0.5cm x 2.5cm, film thickness 10 μm) for making these tapes were the same. After sintering (program SINT9), the c-axis texturing effect of the open films with two average BSCCO particle sizes (0.98 μm and 0.36 μm) were studied.

2.6.1.2 Silver sheathing effect

With the same sintering conditions as the previous set of experiments, sample dimensions, and processing history, the other set of samples were sheathed with silver tapes. After peeling, the particle textures of the samples were examined by X-RAY diffractometry. The resultant data was then compared with those of open film samples.

2.6.2 Sintering Parameter Effect on Superconductivity

Two-stage sintering programs were used to study the sintering parameter effect on the superconductivity of the Ag-sheathed green film with the same microstructure shown in Figure 2-7 (b). Two sintering parameters were controlled: (i) the holding period t_1 (0.1 or 0.5 hour) of the first sintering stage, and (ii) the cooling rate R_2 (2 or 10°C/hour) from the first sintering stage to the second. The critical temperature T_c and ΔT_c were determined by measuring AC susceptibility versus temperature. The magnetization hysteresis loops of the sintered samples were measured by SQUID magnetometry. The magnetization per unit volume was plotted as a function of the applied DC magnetic field.

2.7 Ag/BiSrCaCuO/Ag Tape Strengthening

In this set of experiments, a fine silver particle interlayer was introduced into middle of BSCCO film by electrophoretic deposition. Thus, the continuous superconducting tape fabrication using electrophoretic deposition becomes feasible. As mentioned in Chapter I, the silver is the candidate of metal used in superconducting composite tape, and a expensive metallic material. The advantages of this electrophoretic deposited silver film are (1) effective strengthening the peeling-stress-concentrated zone of Ag-sheathed BSCCO film, (2) uniformly distribution, (3) compatible for BSCCO thick film fabrication technique, (4) cheap equipment cost and (5) merely small amount of silver used.

Commercially available BSCCO powder (99.9% purity and average particle size =0.98 μm) was ball-milled to obtain powder with an average particle size 0.36 μm . The two particle-sized powders were dispersed separately in ethanol with the help of an ultrasonic generator and films were deposited on 25 μm thick silver foils by electrophoretic deposition technique. The deposition conditions were: particle suspension solution concentration 0.2 g/liter, dc electric field 100 volt/cm, an Ag substrate at the negative electrode, and vertically parallel electrode separation distance of 2.8 cm. In an another set of experiments, fine Ag

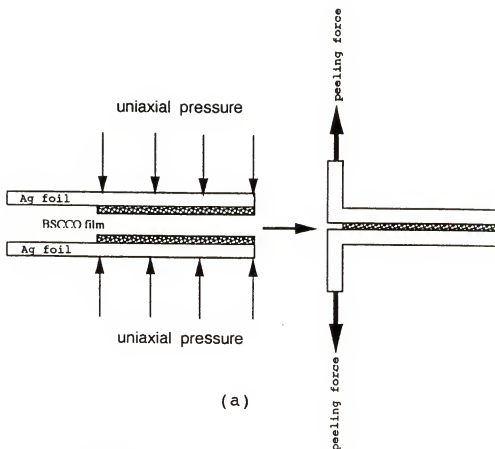
particles were electrophoretically deposited on BSCCO films using Ag particle suspension solution in iso-propanol.

T-peel test was used to characterize the tape adhesion strength for the two sets of experiments with two different BSCCO particle sizes, respectively. The critical current density of these two sets of samples was also measured using SQUID magnetometry, and extended Bean model.

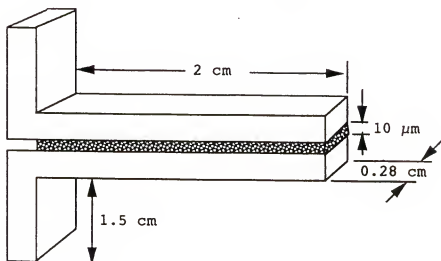
The characterization results were analyzed considering the BSCCO particle size effect, BSCCO particle interaction with fine silver particles, and the nature of single crystalline BSCCO material.

2.7.1 Silver Particle Interlayer Strengthening Investigation

A fine silver particle interlayer was electrophoretically introduced into the middle of BSCCO film shown in Figure 2-8. Four BSCCO films were deposited on two separate Ag substrates. Then fine Ag particle (0.193 μm) film was electrophoretically deposited on one of these BSCCO films. The deposition parameters during Ag deposition were the same as used during BSCCO deposition. Two pairs of BSCCO films, with and without Ag interlayer, were uni-axially pressed at 200 MPa and sintered at 840°C for 10 hours in 0.21 atmosphere of O_2 . The samples were then cooled slowly to 600°C and held there for 5 hours in 0.17 atm O_2 ambient. T-peel tests were conducted on Ag-sheathed BSCCO tapes using



(a)



(b)

Figure 2-8 The schematics of (a) the fabrication procedure and (b) the standard dimensions of Ag/BSCCO/Ag tape specimens for the T-peel test.

the Instron 1122 Universal tester. The fracture analysis of the peeled samples was conducted using scanning electron microscopy (SEM). X-ray diffraction was employed to determine the texturing of the films. The superconducting properties of BSCCO tapes were measured using superconducting quantum interference device (SQUID) magnetometer and were analyzed based on the extended Bean critical state model [Bean64,Gyorg89].

Silver particle suspension preparation was the beginning of this study. Two average particle sizes, 0.19 μm and 1.0 μm were used to prepare the suspension solutions in different organic solvents. All suspensions were prepared as the concentration of 0.2 gram/liter applying the same ultrasonication conditions in terms of ultrasonication power, time (30 minutes), and temperature (25°C). The suspension beaker was cooled in water bath. The evaluation of suspension stability was based on the suspension lifetime measurement. The results showed that 0.19 μm with concentration 0.2 gram/liter was very stable in iso-propanol organic solvent.

2.7.2 Average Particle Size Consideration

As mentioned in the above section, the effect of silver particle interlayer on the adhesion strength of BSCCO tapes with two different average particle sizes were investigated. The average silver particle size was 0.19 μm in 0.2

gram/liter concentration. The silver interlayer was located between two BSCCO thick films of 5 μm each shown in Figure 2-8. The silver particle interlayer was electrophoretically deposited onto the as-deposited BSCCO thick film with average particle size 0.98 μm , then was combined with the other BSCCO tape of the same particle size and film thickness for uniaxial pressing (200 MPa, 25°C, 1 hour). The same procedure was performed on the other set of experiments with average BSCCO particle size 0.36 μm .

Considering the possibility of film microstructure variation across the thickness, the film thickness study method is described in the next section.

2.7.3 Film Thickness Effect

A BSCCO film thickness of 5 μm was prepared with the same conditions as 10 μm thick film. T-peel test was conducted on this Ag/(5 μm thick)BSCCO/Ag tape. The resulted curves of the peel load versus the peel separation for both thickness were compared.

2.7.4 Effect of Consolidation Temperature

Heating during consolidation at 300°C for 1 hour, the Ag-sheathed BSCCO tape with 5 μm film thickness was prepared at the same condition as that for the film thickness effect experiment. The average BSCCO particle size was 0.98 μm .

2.8 Material Characterization

To determine the particle texture in the pre-sintering BSCCO films and grain texture in sintered BSCCO films, the structural characterization such as x-ray diffractometry was carried out. As the other structural characterization method, Scanning Electron Microscopy was used to observe the surface microstructure of BSCCO films and to calibrate the particle size measured by ZetaPlus Particle Analyzer.

Superconductivity characterization was carried out using a Superconductor Quantum Interference Device (SQUID) Magnetometry for critical temperature determination and critical current density, J_c . The temperature and magnetic field dependencies of J_c were characterized, as well as the penetration field strength.

2.8.1 Structural Characterization

Basically there were two major structural characterization techniques, x-ray diffractometry and scanning electron microscopy, used in the microstructure study of silver-sheathed BSCCO thick films prepared modified electrophoretic deposition and thermomechanical consolidation.

(i) X-ray Diffractometry

All samples for texturing characterization were carried out by the x-ray diffractometry. The c-axis texturing effect was evaluated by the peak intensity ratio of (002) to (200)

and (115) peaks in the x-ray diffraction pattern. Generally, x-ray was shone along two orientations of BSCCO tapes, i.e., longitudinal and transverse. From x-ray diffraction data, the texture situation can be detected, and related to the processing effects, intergranular connection, and the superconductivity of the anisotropic BSCCO thick films.

(ii) Scanning Electron Microscopy

Scanning Electron Microscopy (SEM) was used to observe peeled fracture and average particle size calibration. Transgranular or intergranular fracture can be characterized to related to the material microstructure and the BSCCO mechanical properties.

All SEM specimens were mounted on aluminum cylinder using graphite paste without any coating on surface. The SEM used in this study were JOEL Superscope 35CF and JOEL 6400 High Resolution SEM.

2.8.2 Mechanical Characterization

In this study, the mechanical characteristics concerned were T-peel fracture strength and adhesion strength of Ag-sheathed BSCCO films, and how this adhesion strength distributed along the longitudinal or axial direction of the tested Ag-sheathed tape. All samples for this mechanical characterization were prepared with the standardized dimensions shown in Figure 2-8. The adhesion of BSCCO/Ag interface and the fracture strength of BSCCO thick film will be investigated employing mechanical test. The mechanical

test method employed in this study was T-peel Test [Oba93, Sere94] referred ASTM Standard Test Designation D 1876-93 (page 115). The testing instrument was Instron Universal Tester. The two aligned strips of the T-shaped specimen were grasped by the grips of the Instron Tester for applying peeling force.

Some double-sided Scotch tapes were used between the specimen and the Instron's grippes in order to firmly hold the specimen without any slip during the testing.

The samples were carefully prepared. The dimensions of the T-peel test tapes were strictly determined in order to compare the fracture strength of BSCCO thick films, since the factors affecting peel tests are (1) bond width, (2) bond thickness, (3) adhesive modulus (or stiffness of adhesive), (4) angle of stripping, and (5) rate of stripping [Alner65]. In the case of Ag/BSCCO/Ag tapes, the BSCCO thick film is acting as the adhesive for bonding two silver strips; the "bond" refers the portion of BSCCO thick film bonding two Ag sheathes.

The location of peel fracture can be used to indicate whether the adhesion strength of Ag/BSCCO interface is stronger than BSCCO film.

2.8.3 Magnetic Characterization

Quantum Interference Device (SQUID) magnetometer MPMS5 from Quantum Design Incorporation was used for the magnetic characterizations. Samples were usually cut as a few millimeter rectangular shapes from the sintered tapes. A

straw was used as specimen holder shown in Figure 2-9. The specimen's major faces was set either perpendicular or parallel to the applied magnetic field direction, depending on the experiment requirement.

(1) AC Susceptibility Measurements

Alternative magnetic fields of 0.04, 0.4, and 4 gauss were taken terms to measure the AC susceptibility of the sintered superconducting tapes. The applied magnetic fields were applied normal to the specimen surface. All samples were cooled down to 5 Kelvin at zero magnetic field (zero field cooled). Then AC susceptibility was measured versus temperature from 5 to 120 Kelvin. The data point to average was set at 30, and the number of scan was set at 4. The temperature corresponding to the magnetic phase transition from superconductivity to normal conductivity can be revealed from the real number part of the resulted curves, i.e., the temperature corresponding to the start of the highest slope. The humps in the imaginary curves of the tapes indicated the AC loss.

(2) Magnetization Hysteresis

Magnetic hysteresis loops were measured on the samples with different processing conditions. In all H-M hysteresis loop measurements, the sample surface was always set up perpendicular to the applied magnetic field direction. The effects of

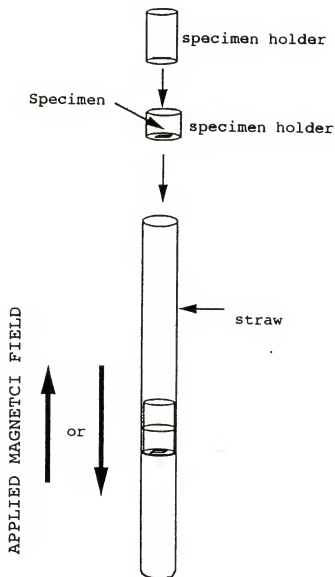


Figure 2-9 The schematic of specimen setup for SQUID magnetometer MPMS5S showing specimen surface perpendicular to the applied magnetic field.

(i)particle size and

(ii)AC field assisted c-axis texturing enhancement of pre-sintering microstructure

on critical current density and the related dependencies of temperature and magnetic field were investigated. From these magnetic hysteresis loops and the Bean Model [Bean62, Gyor89], the critical current density of the measured BSCCO thick films can be calculated.

In a magnetic hysteresis loop, every magnetization value corresponding to a series of magnetic field strengths were measured, and plotted to form such a loop. The maximum range of measuring magnetic field strengths was ± 50000 Oersted, or ± 5 Tesla. The measured magnetization unit is emu. For the critical current density calculation, the volume of the measured thick film needs to be taken into account for converting the emu unit into emu per unit volume, that is, emu/cm^3 . Measured by the SEM cross-section sample after hysteresis loop measurement, the film thickness is also needed to calculate the critical current density.

Before magnetic hysteresis loop measurement, each sample loaded into the SQUID chamber is DC centered to make sure the sample position is located at the center between the sensing coils. With DC appropriate centering procedure, the maximum of DC signal can be correctly detected by the sensing coils. Several control sequence programs were preset before running magnetic hysteresis loop measurement. With tape surface perpendicular to the applied DC magnetic field direction, all

samples were zero field cooled down to 5 Kelvin for magnetic hysteresis loop measurement.

(3) Critical Current Density Estimation

Extended Bean critical state model was used to calculate the critical current density J_c in Ampere/cm² [Gyor89, Dove89]:

$$J_c = 20 \Delta M / [t(1-t/3p)] \quad (2-4)$$

which ΔM is the difference between the positive and negative branches in a given field, and t (cm) and p (cm) ($t < p$) are the face dimensions of the rectangular sample. The J_c along the film surface is generated by applied the magnetic field perpendicular to the film surface.

CHAPTER III AC-ELECTRIC-FIELD MODIFIED ELECTROPHORETIC DEPOSITION OF BiSrCaCuO FILMS

3.1 Introduction

The first stage of the texturing study of electrophoretic deposition is to consider the plate-like particle alignment effect by the applied DC electric field. Then the angular motion behavior of the plate-like particle in AC-electric-field modified electrophoretic deposition (ACEPD) was studied indirectly from the c-axis texturing enhancement factor C_x . The ACEPD electrodes were configured so as that the AC electric field was applied parallel to the substrate surface and perpendicular to the DC electric field. With parallel electric flux, the EPD film texture should be mainly dominated by the major face orientation of plate-like particles, which are migrating toward the smooth and flat substrate surface.

The dependence of c-axis texturing reduction on the applied DC electric field strength was investigated and discussed in order to understand the influence of DC field on the major face alignment effect of plate-like BSCCO particles. The other physical forces (such as fluid dynamic drag force and Brownian motion, etc.) influencing on the

plate-like particle orientation in the suspension were also discussed in detail.

Based on the DC field study results, the c-axis texturing enhancement by ACEPD then was investigated and discussed. To provide a guidelines for further improvement in superconducting properties by improving pre-sintering BSCCO thick film microstructure, a dynamic model was proposed for this study.

With improved pre-sintering film microstructure in terms of c-axis texturing enhancement, the higher critical current density of BSCCO tapes with less magnetic field dependence and reduced thermally-activated flux depinning properties were achieved and discussed in Chapter V. This novel superconducting tape fabrication technology was found very important for c-axis texturing enhancement and densifying with less (or without) particle microcracking and bending.

Then in Chapter VI, the physical modeling of these mechanisms were derived from first principle. Computer numerical simulations were conducted based on these derived nonlinear differential equations. Plots of these simulations illustrated the angular motion behavior of plate-like BSCCO particles in dispersion solution during modified electrophoretic deposition. Particle-geometry-preference-induced electric dipoles associated with plate-like BSCCO particles in ethanol dispersion was proposed to explain the origin of the physical model.

3.2 Plate-like BSCCO Particle Alignment By DC Electric Field

In these sets of experiments, only DC electric fields were applied for electrophoretic deposition of BSCCO dispersions with the same average particle size $0.98\ \mu\text{m}$ in $0.2\ \text{g/liter}$ suspension. The results of electrophoretic deposition condition effects and suspension conditions effects were plotted and discussed. The influence of the other physical forces were also discussed in the next section.

3.2.1 DC Electric Field Strength Dependency

Under DC electric field, the a-axis texturing enhancement with increasing applied electric field has been observed. With average particle size of $0.98\ \mu\text{m}$, the c-axis texturing enhancement factor C_x in the thick films prepared from the dispersion decreases with increasing applied DC electric field strength as shown in Figure 4-1(a). $I_{(0012)}/I_{(200)}$ ratios also decreases with increasing applied DC electric field, that is, a-axis texture to c-axis texture ratio decreases with DC electric field. These results suggest that the applied electric field dependency of a-axis

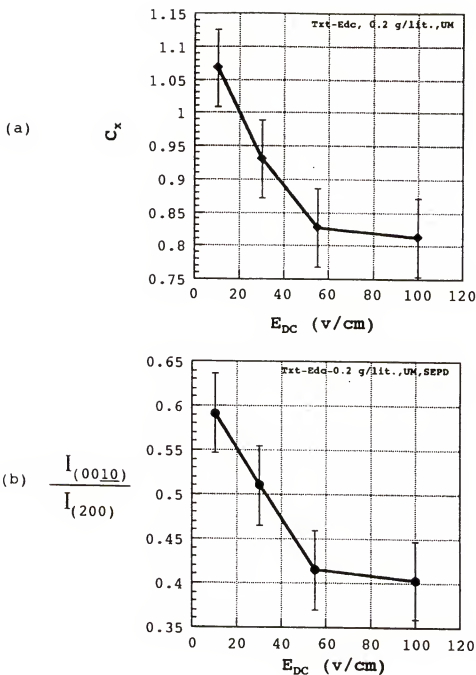


Figure 3-1 The plot of (a)c-axis texturing enhancement factor C_x , and (b)the c-axis to a-axis texture ratio represented by $I_{(0010)}/I_{(200)}$ as a function of the applied DC electric field strength, respectively, using dispersion concentration 0.2 gram/liter of unmilled BSCCO powder.

texturing is a general effect for the electrophoretic deposition plate-like BSCCO particle dispersion. The a-axis texture represents particles deposited with their major face perpendicular to the substrate surface.

The above experimental results are discussed in the following paragraphs.

The resulting reduction in c-axis texture fraction and in the ratio of c-axis texture to a-axis texture with increasing DC electric field is due to the plate-like BSCCO particle major faces (// ab-plane, i.e., two parallel largest surface area) re-orienting parallel to the applied field direction. The orientation of particles approaching toward substrate determines that of the deposited particles. There are many BSCCO particles having the longest dimension along a-axis direction. If many BSCCO particles move with their a-axis in the applied DC field direction, a-axis texture enhancement would be resulted. The way that the applied DC electric field can re-orient the major face of plate-like BSCCO particles in the dispersion could be due to the interaction between induced dipole and the applied electric field [Purce65]. One logical explanation is that the induced electric dipole associates with a plate-like BSCCO particle preferentially formed along the long dimension of the major face of plate-like BSCCO particle. It is well known that the anions in the electric double layer, which are associated with the spherical-particle surface charge, can be deformed to extended along the applied electric field

orientation[Sarka96]. Furthermore, the plate-like particle shape of BSCCO takes into account the polarization process. The detailed mechanisms will be discussed later.

Primary factors affecting the BSCCO particle orientation are considered as: (i) electric forces, (ii) fluid dynamic forces, and (iii) particulate interaction. The following discussion can lead to the conclusion that electric force is the dominant factor for plate-like BSCCO particle orientation control.

It is also expected that fluid dynamic forces may affect plate-like BSCCO particle orientation during the electrophoretic deposition. Major fluid dynamic force possibly affecting BSCCO particle orientation is due the torque induced by dynamically unbalanced distribution of fluid dynamic drag. Under certain fixed fluid dynamics conditions, the degree sequence of fluid dynamic drag on a plate-like body from the surrounding organic medium liquid [Golds38] are: (1) the highest with their major faces perpendicular to the migration path toward the substrate surface, (2) less with inclined major faces to moving direction, and then (3) the least with the major faces parallel to the migration direction. It is important to further consider Reynolds number in the studied case. If the Reynolds number is high enough ($>10^4$) [Courc79] and the BSCCO particle major faces are parallel to the moving direction, fluid dynamic drag induced torque on such oriented particles can affect particle orientation. However, the velocity of

BSCCO particle migration in electrophoretic deposition cell is very low. The Reynolds number should be very low as the following estimation. The Reynolds number is defined as

$$Re = UD/v \quad (3-1)$$

which v ($= \mu/\rho$ = viscosity/density) kinematic viscosity of ethanol (C_2H_6O of density $\rho = 789 \text{ kg/m}^3$)

U is a velocity characteristic of the overall flow field, (i.e., particle migration velocity)

D is a length which characterizes the size of the structure in the flow (inter-electrode distance).

The value U can be estimated from the particle velocity.

$$U = (\text{average deposition rate}) / (\text{BSCCO density}) \quad (3-2)$$

$$= (2 \times 10^{-5} \text{ g/min.cm}^2) / 7 (\text{g/cm}^3) \sim 4.7619 \times 10^{-10} (\text{m/sec})$$

D may be estimated as the separation between two electrodes.

$$D = 2.8 \times 10^{-2} (\text{m})$$

Viscosity μ of ethanol can be calculated from the viscosity equation [Velz72]

$$\mu = 10^A \{ (1/T) - (1/T_0) \} \times 10^{-3} \quad (\text{N}\cdot\text{sec/m}) \quad (3-3)$$

The coefficients $A=687$ and $T_0=301$ Kelvin are for ethanol. ρ is ethanol density 789 kg/m^3 . By inserting the numbers into the above equation, the μ can be obtained $1.1543 \times 10^{-3} \text{ N}\cdot\text{sec/m}$ at $T=293\text{K}$. Thus, the kinematic viscosity is $1.463 \times 10^{-6} \text{ m}^2/\text{sec}$ at 20°C . Usually, the liquid viscosity on solid surface is one sixth of liquid, that is, ethanol/BSCCO kinematic viscosity could be $2.4383 \times 10^{-7} \text{ m}^2/\text{sec}$. So, Reynolds number can be estimated as

$$Re = (4.7619 \times 10^{-10} \text{ m/sec}) (2.8 \times 10^{-2} \text{ m}) / (2.4383 \times 10^{-7} \text{ m}^2/\text{sec})$$

$$=5.4683 \times 10^{-5}$$

This Reynolds number is too small ($\ll 10^4$) for the fluid dynamic drag can be very large. As $Re < 10^{-1}$, the resulted drag coefficient C_D is about for cylindrical bodies with rectangular cross-section 60[Muns94]. The drag force F_{drag} can be calculated using the following equation

$$C_D = F_{drag} / (0.5 \rho V^2 L^2) \quad (3-4)$$

Assume that C_D is 10^{10} for $Re=5.4683 \times 10^{-5}$,

$L=1 \mu m$ particle size, and

$V=$ characteristic velocity $= 4.7619 \times 10^{-10} (m/sec)$,

the drag force could be

$$F_{drag} = C_D (0.5 \rho V^2 L^2)$$

$$\begin{aligned} &= (10^{10}) \{0.5 \times 789 (kg/m^3) \times [4.7619 \times 10^{-10} (m/sec)]^2 \times [10^{-6} (m)]^2\} \\ &= 7.89 \times 10^{-14} \text{ (Newton)} \end{aligned}$$

Considering the possible maximum torque exerted by the drag force

$$P_{drag} = F_{drag} (\text{particle maximum dimension})$$

$$= [7.89 \times 10^{-14} \text{ (Newton)}] [10^{-6} (m)] = 7.89 \times 10^{-20} \text{ (N}\cdot\text{m)}$$

This torque on a BSCCO particle by fluid dynamic drag force needs to be compared with that by electric force. The maximum torque by electric force can be expressed as

$$\tau = P_e E \quad (3-5)$$

which $E=$ applied electric field, usually 100 v/cm , and electric dipole moment can be estimated as

$$P_e = \text{electric dipole moment} = sq \quad (3-6)$$

$$= (\text{separation of counter-charge center}) \cdot (\text{charge})$$

$$\begin{aligned}
&= (0.1 \text{ particle dimension}) [2(10^{-3}) (\text{surface atomic density})] \\
&= (0.1 \times 10^{-6} \text{m}) \{2(10^{-3} \text{ charge/atom}) [2(\text{atoms/lattice}) / (5.3 \times 10^{-10} \text{m})^2]\} (1.6 \times 10^{-19} \text{ Coulomb/charge}) \\
&= (1 \times 10^{-7} \text{m}) (2.2784 \times 10^{-4} \text{ Coulomb}) \\
&= 2.2784 \times 10^{-11} \text{ (Coulomb} \cdot \text{m)}
\end{aligned}$$

then the possibly largest torque on dipole can be estimated as $\tau = \mathbf{P}_e \times \mathbf{E}$ (3-7)

$$\begin{aligned}
&= \mathbf{P}_e E \cdot \sin(\text{angle between dipole and electric field}) \\
\tau &= (2.2784 \times 10^{-11} \text{ Coulomb} \cdot \text{m}) (10^4 \text{ v/m}) [\sin(90^\circ)] \\
&= 2.2784 \times 10^{-7} \text{ (Coulomb} \cdot \text{v} = \text{Newton} \cdot \text{m)}
\end{aligned}$$

This possible maximum torque by electric force is much larger than $7.89 \times 10^{-20} \text{ (N} \cdot \text{m)}$ by fluid dynamic force. Therefore, the fluid dynamic force effect on BSCCO particle orientation can be neglected further in this study.

Brownian motion of particles in the fluid may influence the orientation of plate-like BSCCO particles. The maximum torque by the collision between particles is estimated theoretically in the following. The average force on a BSCCO particle by collision can be calculated from average Brownian motion velocity and mean free path of a particle using statistic thermodynamics theories. The average particle velocity between collisions with the other particles (including medium's molecules) can be expressed as [Bird60]

$$u_{\text{avg}} = (8k_B T / \pi m)^{1/2} \quad (3-8)$$

where k_B = Boltzmann constant = 1.38062×10^{-23} joule/K,

T = temperature (K), and

m = particle's mass (kg).

The mean free path of the particle can be written as

$$\lambda = 1/[(2)^{-1/2} \pi d^2 n] \quad (3-9)$$

which d is the particle size (in meter), and n is the number density of particle in m^{-3} . Considering plate-like BSCCO particles of average size $1 \mu m \times 1 \mu m \times 0.1 \mu m$ are used to make 0.2 g/liter (or 0.2 kg/m^3) concentration dispersion in ethanol medium. The density of BSCCO is about 7 g/cm^3 ($= 7000 \text{ kg/m}^3$). The weight of each particle is

$$\begin{aligned} m &= (\text{particle volume}) (\text{particle mass density}) \\ &= (10^{-19} \text{ m}^3) (7000 \text{ kg/m}^3) = 7 \times 10^{-16} \text{ (kg/particle)} \end{aligned}$$

The number density of BSCCO particle can be estimated as

$$n = 0.2 \text{ (kg/m}^3) / (7 \times 10^{-16} \text{ kg/particle}) = 2.8571 \times 10^{14} \text{ (particles/m}^3)$$

Then, the mean free path can be calculated as

$$\begin{aligned} \lambda &= 1/[(2)^{1/2} \pi d^2 n] \\ &= 1/[(2)^{1/2} \pi (10^{-6} \text{ m})^2 (2.8571 \times 10^{14} \text{ m}^{-3})] \\ &= 7.8779 \times 10^{-4} \text{ (m)} = 787.79 \text{ (}\mu\text{m)} \end{aligned}$$

This value is larger than average inter-particulate separation of $15.183 \mu m$. The average velocity for Brownian motion of BSCCO particles is then

$$\begin{aligned} u_{\text{avg}} &= [8(1.38062 \times 10^{-23} \text{ joule/K}) (293 \text{ K}) / \pi (7 \times 10^{-16} \text{ kg})]^{1/2} \\ &= 3.8361 \times 10^{-3} \text{ (m/sec)} \end{aligned}$$

Therefore, the mean free time can be calculated as

$$\begin{aligned} t_{\text{mfp}} &= \lambda / u_{\text{avg}} = (7.8779 \times 10^{-4} \text{ m}) / (3.8361 \times 10^{-3} \text{ m/sec}) \\ &= 0.20536 \text{ (sec.)} \end{aligned}$$

The average velocity can be treated as the velocity reached after the particle had been accelerating by a collision for $(t_{\text{mfp}}/100)$. Hence, using Newtonian motion principles, the acceleration can be estimated as

$$\begin{aligned} a &= u_{\text{avg}} / (t_{\text{mfp}}/100) = (3.8361 \times 10^{-3} \text{ m/sec}) / (2.0536 \times 10^{-3} \text{ sec}) \\ &= 1.868 \text{ (m/sec}^2\text{)} \end{aligned}$$

The force exerting on particle during collision would be

$$\begin{aligned} F_{\text{Brownian}} &= ma = (7 \times 10^{-16} \text{ kg}) (1.868 \text{ m/sec}^2) \\ &= 1.3076 \times 10^{-15} \text{ (kg} \cdot \text{m/sec}^2 = \text{Newton)} \end{aligned}$$

Finally, the torque on BSCCO particle due to Brownian motion can be calculated as

$$\begin{aligned} \tau_{\text{Brownian}} &= F_{\text{Brownian}} \times (\text{maximum dimension of BSCCO particle}) \\ &= [1.3076 \times 10^{-15} \text{ (N)} \times 10^{-6} \text{ (m)}] \\ &= 1.3076 \times 10^{-21} \text{ (N} \cdot \text{m)} \end{aligned} \tag{3-10}$$

This resulted torque due to Brownian motion is many order magnitude lower than that by electric force. Therefore, the influence by Brownian motion can be neglected. The next factor affecting the BSCCO particle orientation is particulate interaction (or actually dipole-dipole interaction). Since the electric field generated by a dipole is much smaller than the applied field^[Israe92], the effect of

dipole-dipole interaction on BSCCO particle orientation can be ignored.

The effect of particle surface electrochemical change on particle orientation was then considered. Under the applied electric field strength, the electric double layer should have not yet been broken down. That is, the layer of adsorbed anions on particle surface is still stable under the applied field in the study. Neither particle surface charge distribution can not be changed by the applied electric field, nor can electrochemical reactions vary such surface charge distribution. No electrochemical reactions are involved in organic ethanol medium, either [Sarka96]. So electrochemical factor were not considered as to particle orientation control.

According to the lyosphere distortion and electric double layer thinning mechanism for spherical particles proposed by Sarkar et al. [Sarka96], the electric double layer of plate-like particles was elongated in the direction of the applied electric field. In such distorted lyosphere, the tail with higher concentration of cation bonded tends to elongate toward the anode, and the head with lower concentration of cations tends to thin toward cathode direction. Since the BSCCO particle shape is plate-like, the "lyosphere distortion" phenomena can be modified in the case of plate-like particles. Misaligned to electric field direction with tilt angles, the plate-like particle has adsorbed anions surround it tending to elongate along the particle major

surface, while the distance between the anions and particle surface is kept the same. This is because the dissolved electric force in particle surface normal direction to displace anions is much smaller than that particle surface charge attraction force shown in Figure 3-2(a). No Zeta potential changes perpendicular the particle surface; therefore there is no need of overcoming the energy barrier for dipole formation in the direction along the major face of particles. In this manner, the dipoles along the plate-like particle major face responds to the applied field. Among these induced electric dipoles, an net effective dipole which possesses the largest dipole moment in the orientation of the longest dimension along its major face can dominate over the others for particle re-orientation shown in Figure 3-2(b). Thus, the longest dimension of the BSCCO particles tends to re-orient toward the applied electric field direction by the virtually two-dimensional distortion of electric double layer along the longest dimension of major face. As mentioned earlier, due to fluid dynamic forces, those plate-like particles align their major faces along the applied electric field direction can have higher mobility. Incorporating these two type of forces (electric & hydrodynamic) on the plate-like particles, the higher the applied electric force, the more elongation of the electric double layer around the plate-like particle which results in stronger electric dipole moment to align the particle's major faces tilting the applied electric field direction. Therefore, the dipole will

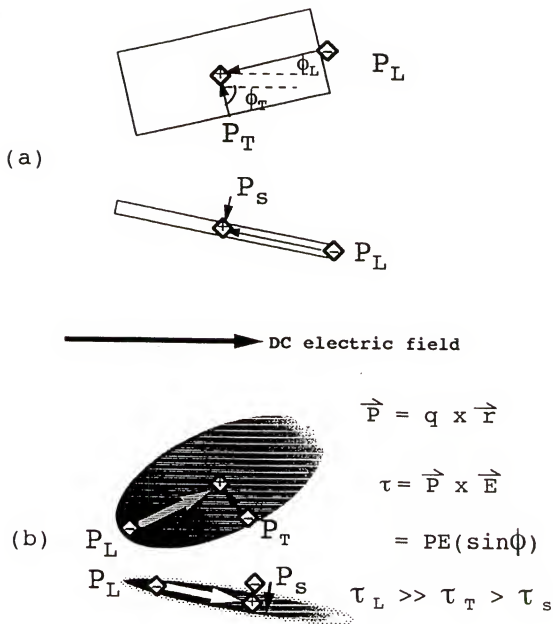


Figure 3-2 The schematic illustrates the dominant particle-geometry-preference-induced electric dipole moment over the others can align the particle major face along the applied DC electric field in dispersion solution: (a) original angle ϕ with respect to E_{DC} , and (b) the largest electric dipole moment associated with the longest dimension of particle major face.

finally align the applied electric field direction. It is reasonable that many plate-like BSCCO particles have their longest dimension along a-axis, thus, the a-axis texture ratio of the as-deposited thick films increases with higher applied electric field strength as shown in Figure 3-3.

A-axis texturing was the focused point in this discussion. At the low field of 10 v/cm, the induced dipole moments (in their longest dimension along their a-axis) associated with many BSCCO particles are not large enough to align by very low applied electric field. Therefore, the a-axis texture is relatively less at low applied electric fields. However, at higher electric field 100v/cm, the strong interaction among large induced dipole moments dominated over the interaction between dipole moment and the high applied electric field, and the alignment by the applied electric field enhanced.

The parallel electric field lines ensures the effect of particle major face alignment along the applied electric field. Special electrode configuration design mentioned in Chapter III is essential for the electric parallel flux enhancement.

3.2.2 Electric Flux Incident Angle Effect

This experiment further proves the concept of particle major face alignment along the applied electric field (Figure 3-4(a)). C_x in the BSCCO thick films decreased with the tilt

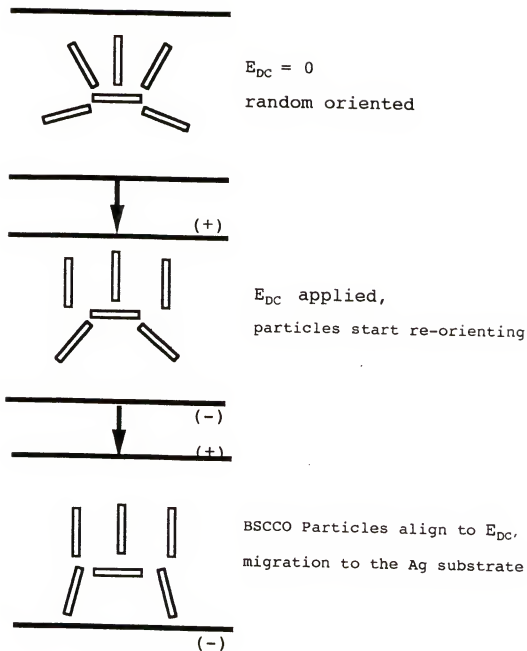
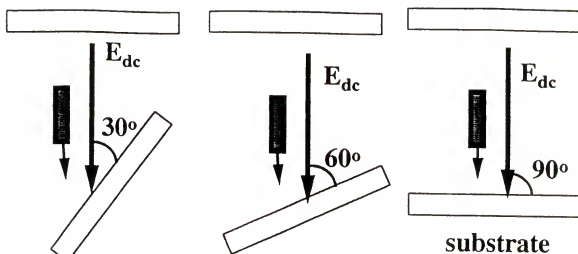


Figure 3-3 The schematic of platy BSCCO particle electrophoretic deposition with a-axis texturing enhancement by strong DC electric field.



$$\left[\frac{I_{(200)}}{I_{(002)}} \right]_{30^\circ} < \left[\frac{I_{(200)}}{I_{(002)}} \right]_{45^\circ} < \left[\frac{I_{(200)}}{I_{(002)}} \right]_{90^\circ}$$

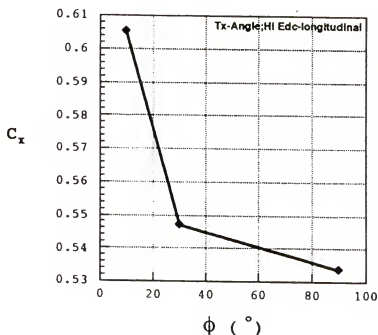


Figure 3-4 The inclined angle effect on particle texturing: (a) schematic of electrode configuration, and (b) the plot of C_x as a function of inclined angle i.e., particle major face texture reduction with decreasing inclined angle of the Ag substrate surface with respect to strong DC electric field direction.

angle between the applied DC electric field and substrate surface as shown in Figure 3-4 (b). The resulting experimental plot showed that the a-axis to c-axis texture ratio also increases with increasing angle ϕ between the substrate surface and the applied electric field direction shown in Figure 3-4 (b). That is, as decreasing in the inclined angle of the applied electric field toward substrate surface, more particles having their major faces parallel to applied electric field can be deposited as c-axis texture. At large tilt angles, those incident particles with their a-axis aligned the applied electric field direction can result in a-axis texturing enhancement. This experimental results indeed further confirms the particle major face alignment along applied electric field direction, and implies the concept about the particle-geometry-preferred induced dipole explains plate-like BSCCO particle orienting behavior during electrophoretic deposition.

The effect of other suspension conditions on BSCCO particle orientation control by EPD, such as suspension concentration (i.e., inter-particulate separation), and average particle size (i.e., particle aspect ratio), are discussed in the following sections.

3.2.3 Effect of Iner-particulate Separation

The effect of BSCCO particle dispersion concentration on particle texturing with increasing DC electric field strength was investigated and the results are shown in Figure 3-5. As

mentioned in the experimental approach, as the reduced dispersion concentration can result in the further average inter-particulate separation. The similar dependencies of C_x and the c-axis to a-axis texture ratio on DC electric field strength are valid for different suspension concentrations. Applied the same electrophoretic deposition conditions, the higher c-axis texture ratios in BSCCO thick films were always deposited from the dispersions with lower concentration (shown in Figure 3-5(b), that is, smaller inter-particulate separation resulted in higher a-axis texture ratio. Slight c-axis texturing enhancement was only observed in the film deposited from low concentration at lowest DC electric field strength 20 v/cm. The other films consist of higher a-axis texture ratio or lower c-axis texture ratio than that of random-oriented powder sample. Figure 3-5 also showed that the DC electric field dependence is more pronounced in low concentration suspensions. This implies that plate-like BSCCO particles in lower concentration dispersion have more freedom to re-orient by the applied electric field.

The phenomena that slightly higher a-axis texturing enhancement in higher concentration dispersion can be related to the stronger interactions among closer dipoles (associated with BSCCO particles) due to shorter inter-particulate distances. The smaller inter-particulate separation

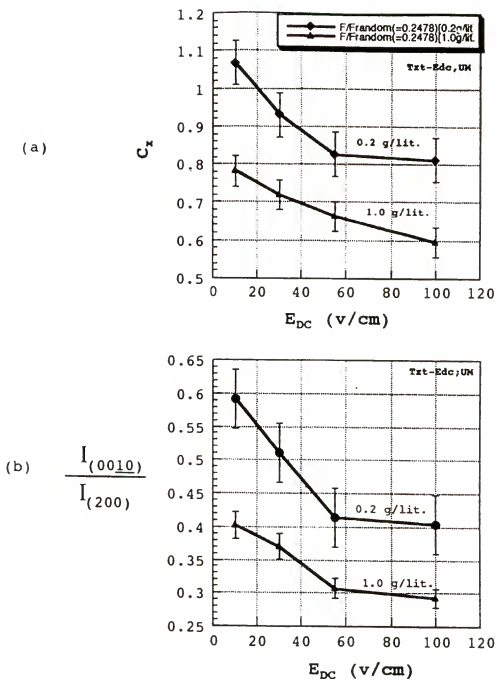


Figure 3-5 The plot of the DC electric field dependency of (a) c-axis texturing enhancement factor C_x , and (b) c-axis to a-axis texture ratio deposited from two different dispersions showing that the films deposited from lower concentration 0.2 gram/liter always have higher c-axis texture ratios than those from high concentration 1 gram/liter.

(i.e., in higher concentration suspension), the stronger attraction among in-line oriented particles interaction via van der Waal interaction mechanism [Israe92] illustrated in Figure 3-6, while the stronger repelling among parallel dipoles also enhanced the holding the particle with such orientation [Purce65]. It requires less force exerted by the applied electric field to hold such closer induced dipole moments (depicted in Figure 3-6) [Israe92] along the field direction. Hence, closer inter-particulate separation can enhance the particle major face alignment by the applied electric field, i.e., the particles with shorter inter-particulate separation can align their one long dimension within the major face along the applied electric direction. This results in more a-axis texture, since many particles have their longest dimension along a-axis orientation.

In the other hand, the high dispersion concentration results in less pronounced electric field dependence of a-axis texturing can be explained as the following. Due to closer inter-particulate separation, the stronger inter-particulate interaction brought about less particle freedom to re-orient along the applied electric field direction. Therefore, the same field strength can only result in less a-axis texturing in higher concentration. That means, the more plate-like particles' major face can be aligned along the applied electric field direction.

The BSCCO's average particle size influence on the texturing was also investigated in the next section.

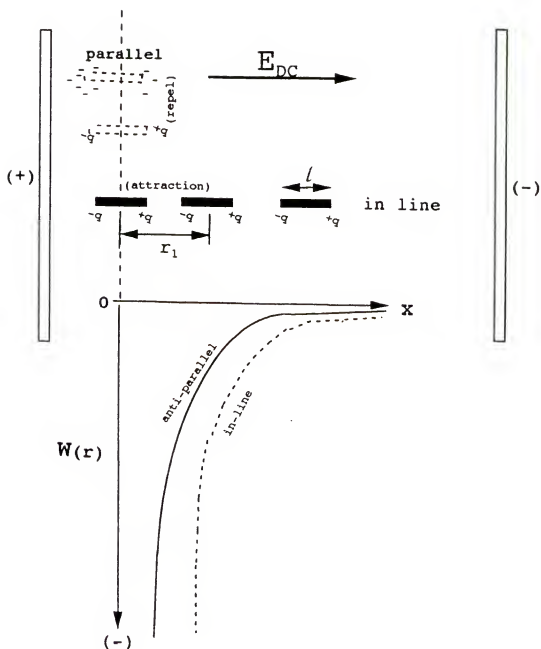


Figure 3-6 The schematic of the relation among the inter-particle distance and the dipole-dipole interactions affecting re-orienting particle major face parallel to the applied electric field.

3.2.4 Particle Aspect Ratio Consideration

As shown in Figure 3-7(a), the c-axis texture enhancement factor C_x increased about twice higher with reduction in average particle size from 0.98 μm to 0.36 μm deposited from 0.2 gram/liter concentration dispersions at different applied DC electric fields. The c-axis texture enhancement factors C_x of the films deposited from smaller particle sized dispersion were ranged from 2.59 to 2.02, and the $I_{(0010)}/I_{(200)}$ ratios were ranged from 4.56 to 2.52, while the C_x for larger particle size were from 1.06 to 0.78 and $I_{(0010)}/I_{(200)}$ ratios were from 0.592 to 0.414. That is, by only reducing average particle size down to 36.7%, the c-axis texturing effect was enhanced up to six times higher. However, the x-ray diffraction spectra of BSCCO films prepared from smaller particle sizes showed that higher background noise, even the specimen dimensions and sample setup are the same. The ultra fine-particles have too low crystallinity to contribute to x-ray diffraction signal.

The $I_{(0010)}/I_{(200)}$ ratio dependence and the c-axis texturing enhancement factor dependence on DC electric field strength for larger particle films is more pronounced than that for smaller particle films. These results indicated the orientation of larger particles is easier to be controlled by the applied electric field. It implies that the induced dipole moment associated the larger BSCCO particle is also

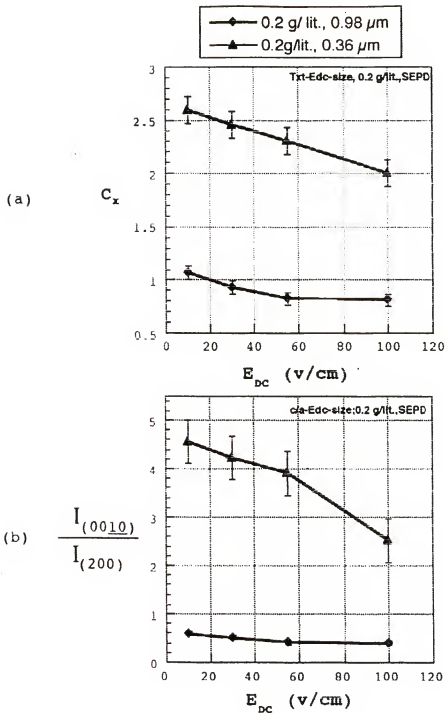


Figure 3-7 The plot of (a) normalized Lotgering factor, (b) c-axis to a-axis texture ratio as a function of the applied DC electric fields using two 0.2 gram/liter suspensions of different average particle sizes.

larger than that with smaller particle. Under the same applied electric field, the larger the dipole moment, the greater the torque is exerted by the applied dielectric field. Such results are consistent with the concept derived from the particle-geometry-preference-induced dipole moment domination.

There are three considerations for the particle size effect on c-axis texturing enhancement: (i) particle aspect ratio effect, (ii) the higher probability of smaller particle to be deposited at the accommodating sites on substrate surface where major face is allowed parallel to the substrate surface, i.e., c-axis texture deposition occurs, and (iii) strong interactions among closer neighboring particles due to higher number density of smaller particles as weight density the same as larger particle's. In the following paragraphs, these considerations will be discussed.

The aspect ratio of a plate-like BSCCO particle is the ratio of its length on the major face to its thickness. For most of BSCCO particles, the particle thickness varies little. So, smaller particle size is simply meaning lower aspect ratio of particle. With lower particle aspect ratio, the electric field induced dipole moment is smaller; thus the electric-field-driven rotation mobility of smaller particles is lower than that of larger particles. The influence of the applied electric field on such smaller electric dipole moment (of smaller particle) is therefore weaker than that on larger dipole moment (of larger particle).

With the electric double layer associated with a plate-like BSCCO, an oblate ellipsoid approximation is employed for the particle-geometry-preference-induced dipole moment domination, shown in Figure 3-2(a). Among field-induced dipoles, the electric dipole moment along the largest dimension of the major face can dominate over the others. The higher the aspect ratio (longest axis to shortest axis), the more dominant of such induced dipole moment is. This particle aspect ratio effect results in lower a-axis texture ratio. That is, the c-axis texturing is relatively enhanced in the thick films deposited from suspensions of smaller average particle size.

Smaller sized particles possess smaller induced electric dipole moment due to the particle-geometry-preference (discussed in the latter section). Less dipole-field interaction results in less effective torque for particle re-orientation by the applied field. In the other hand, those ultra-fine particles of worse crystallinity can only have contribution to the noise for x-ray diffraction signal as higher noise ratio in Figure 4-14(b).

At the same weight concentration 0.2 gram/liter, the dispersion made of smaller average particle size has higher particle number concentration (number of particles per unit volume). Similarly as discussed in the section of dispersion concentration effect on a-axis texturing, the higher the number concentration, the stronger the interactions among particles is, and thus, the less freedom for the particles to

align their induced dipole moments (i.e., their major faces) along the applied electric field direction.

As the average particle size reduced to one third of the original value, the particle number concentration could increase up three times, because the one third reduction in particle size is simply breaking the major faces of plate-like BSCCO particles into three pieces. The reduction in average particle size is actually to increase the aspect ratio of plate-like BSCCO particles. Since, observed by SEM, the thickness of plate-like BSCCO particles remained after ball milling, which only reduced the size of the particle major face (parallel to ab-plane of the BSCCO crystallography). This phenomena could be explained by the fact that plate-like BSCCO particle were primarily subjected to impact cracking perpendicular to their major faces during the ball milling, resulting in easy breaking down the major faces of particles, although the study on $\text{YBa}_2\text{Cu}_3\text{O}_{8-7}$ single crystals showed that fracture toughness along planes parallel to ab-plane is about one half value of that perpendicular to ab-plane. [Rayne91].

3.3 C-axis Texturing Enhancement with Additional AC Electric Field Parallel to Substrate Surface

Based on the above experimental results and discussion, the tendency of plate-like particle major face texturing with the applied DC electric field in BSCCO particle dispersion solution can be employed to modify the electrophoretic

deposition texturing. The novel method to modify conventional electrophoretic deposition technology will be presented and discussed in the following sections.

To enhance c-axis texturing of BSCCO polycrystalline films using electrophoretic deposition technique, the plate-like BSCCO particles have to orient their major faces parallel to substrate surface during electrophoretic migration. By applying an additional AC electric field parallel to the substrate surface, no BSCCO particles deposited on the AC electrodes. An angular motion behavior model of the plate-like BSCCO particle in modified electrophoretic deposition was derived to explain the observed results. Computer simulation of the above physical model was conducted for fundamental understanding the orientation control of plate-like BSCCO particles in dispersion solution.

Learning from the effects of electrophoretic deposition parameters and suspension solution conditions on particle texturing of BSCCO thick films, the suitable processing conditions were applied for ACEPD technique. Thermomechanical Consolidation method was also used to consolidate the green films (for further reducing the inter-particulate micropores), and to make silver-sheathed superconducting BSCCO tapes. Both c-axis texturing enhancement factor and the ratio of a-axis texture to c-axis texture were plotted as functions of the applied ACEPD conditions. Using these conjugated data for the experimental results, The particle

re-orientation by the applied electric fields can be correlated to particle alignment during electrophoretic deposition

As the AC field strength is higher than DC electrophoretic field, an additional stronger AC electric field parallel to the substrate surface was found capable of converting the a-axis texturing enhancement effect into c-axis texturing enhancement effect. C-axis texture was also evaluated by the c-axis texturing enhancement factor, C_x , defined in Chapter II.

Depending on the AC electric field conditions, the particle texture in BSCCO thick films can be electrophoretically controlled by using an additional AC electric field which is perpendicular to the electrophoretic field (2.5 mm) near the substrate and parallel to the substrate surface shown in Figure 2-6. With the same suspension conditions and DC electrophoretic field, the effect of AC electric field strength on the electrophoretic deposition rate was also investigated to relate to the mechanism of modified electrophoretic deposition. As variable texturing control factors, the strength and frequency of the applied AC electric field, DC electric field strength and the distance between AC electrodes and substrate were discussed. The detailed mechanism of c-axis texture enhancement by ACEPD is discussed in Chapter VI.

The strength of the applied AC electric field was investigated first in these series of experiments.

3.3.1 AC Electric Field Strength Effect

With a constant low DC electric field 40 v/cm, the AC electric field strength applied were from 2.5 to 7.5 times higher than DC's in this experiment set, while the gap between AC and substrate surface, and dispersion concentration were also kept constant. The c-axis texturing enhancement factor C_x was investigated versus AC field strength. The study results of the c-axis texturing enhancement factor dependence on the applied AC electric field strengths of 0, 20, 40, 60, 100, 200, 250 and 300 v/cm at AC field frequency 150 Hz were shown in Figure 3-8(a). The $I_{(002)}/I_{(200)}$ ratio dependence on AC field shown in Figure 3-8(b) is similar to that of c-axis texturing enhancement factor. It was found c-axis texture increase is accompanied by the reduction of a-axis texture due to the AC electric field assistance. The values of randomly-oriented powder samples and DC-field-only samples were included into these curves for comparison. From Figure 3-8(a), it is clear that C-axis texture enhancement factor C_x increased with the applied AC electric field strengths up to 2.87 at 200 v/cm, then C_x slowly dropped with the higher AC field. Generally, c-axis texture enhancement factors were 2.3~2.87 increasing with AC fields. The $I_{(002)}/I_{(200)}$ ratios rises up to 1.9 with AC field strength 250 v/cm assistance, while (002) peak is too low to be detected on the normal EPD (DC field only) film. This indicates that the AC field assistance leads

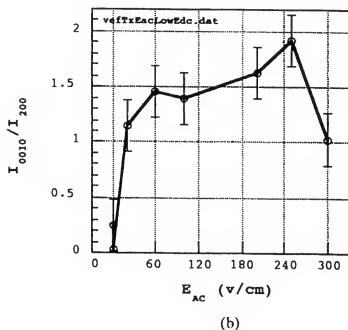
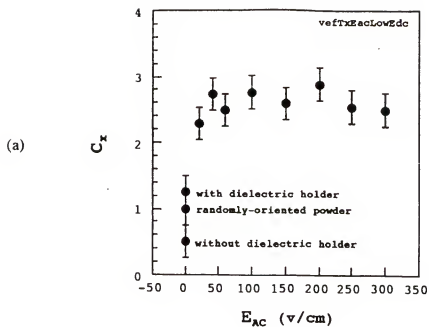


Figure 3-8 The c-axis texturing enhancement by the modified electrophoretic deposition with AC electric fields parallel to substrate surface at frequency 150 Hz and $E_{DC}=40$ v/cm: (a) the c-axis texturing enhancement factor and (b) (0010) to (200) texture ratio versus the applied AC electric field.

to more BSCCO particle re-orientation with their major faces aligning to AC electric field direction (parallel to substrate surface); i.e., more particles have higher probability to deposited as c-axis texture on substrate. The results of this experiment set also confirmed the concept about particle-geometry-preferred induced dipole moment domination.

The drop in c-axis texture enhancement factor corresponding to 300 v/cm. There is deteriorating effect on plate-like particle alignment along AC field direction by applying too high AC electric field strength at that frequency. The first possibility can be considered in the interaction between induced electric dipole (associated with particle) and the applied AC field. As AC fields are higher than a critical value at a given frequency, BSCCO particles start to be magnified their amplitude of angular vibration due to the increased angular vibration inertia of BSCCO particles. Applied AC electric fields below the critical value, the increasing field strength can increase the angular vibration inertia of BSCCO particles to overcome the viscosity, and thus enhances the particle orientation controllability by applied AC field. That is, the axial orientation of the particle's angular vibration approaches AC field orientation as the AC field is increasing but still below the critical value.

The other possibility for this deteriorated texturing effect could probably be due to breaking down the over-

extended "wings" (induced along the E_{AC} orientations) of the anion layer adsorbed surrounding some BSCCO particles, then this selective broken-down effect could lead to coagulation between neighboring particles along the AC electric field orientations. The orientation of coagulated particle clusters can not be controlled anymore. Hence, the too high AC electric field can result in less particles orienting their major faces along AC electric field, namely, $I_{(002)}$ reduction resulted. This possibility is unlikely, since a-axis texturing still can be obtained in DC electric field strength as high as 500 v/cm in electrophoretic deposition by the author.

The cooperation of AC and DC electric field strengths determines the particle major face orientation as shown in Figure 3-9. In high AC and low DC electric fields case, the c-axis texture can be enhanced [Figure 3-9(a)]. As the DC field strength is higher than AC field's, the resultant particle texture would be enhanced as a-axis texture or the texture with particle major faces perpendicular to substrate surface shown in Figure 3-9(b).

3.3.2 AC Electric Field Frequency Dependency

AC frequency effect on BSCCO particle orientation controllability was studied in this set of experiments. Deposited at strong AC electric field 200 v/cm and medium DC field 40 v/cm, the c-axis texturing enhancement factor C_x of

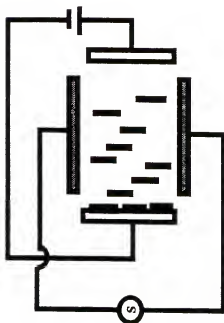
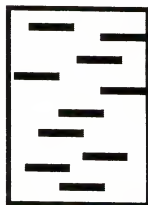
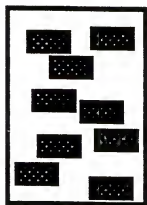
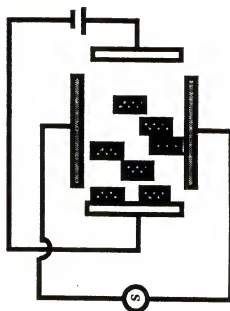
(1) High E_{AC} & low E_{DC} (2) High E_{DC} & low E_{AC} 

Figure 3-9 The schematic of platy BSCCO particle having their longest dimension aligned with the dominant electric field in suspension: (a) weak DC electrophoretic field, and (b) strong DC electrophoretic field.

BSCCO thick films increases with increasing AC frequency from 50 Hz to 250 Hz, then decreases with further higher frequency 250 Hz shown in Figure 3-10. It seems there is a maximum in C_x corresponding to 200 Hz. This phenomena suggested that there might be a resonant frequency for the natural vibration frequency of induced electric dipoles and the AC electric field frequency. Away from this resonant frequency, field-induced dipole moments associated with BSCCO particles have less rotation mobility to re-orient their longest dimension aligning along AC electric field direction, that is, less particles can be migrate toward substrate with their major faces parallel to the substrate surface. However, this can not be confirmed due to restriction by the capability of the AC power supply which has maximum operation frequency only 270 Hz. The drop in C_x at the highest frequency 250 Hz could be an experimental error. Whether the resonant frequency exists or not can be examined by computer simulation modeling. According to the physical model of dispersed particles, there is no such nature angular vibration frequency for dispersed particles due to Brownian motion is random motion of very fine body. Particles interact with the surrounding medium via fluid dynamic force and thermal vibration. The resonant vibration behaviors usually occur by applying a restoring force in the physical systems. The restoring force can periodically changes with the response of the object exerted by the force. Thus, the restoring force is acting like a switching force.

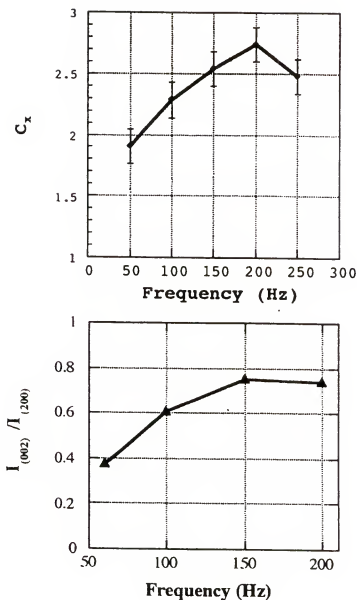


Figure 3-10 The plot of (a) the c-axis texturing enhancement factor as a function of the applied AC electric field frequency and (b) $I_{(002)}/I_{(200)}$ as a function of AC field frequency at constant DC 40 v/cm and AC field strength 200 v/cm, using 0.2 g/lit. BSCCO particle dispersion solution with average particle size 0.98 μm .

Electric-field-induced electric dipoles of adsorbed ion layer around BSCCO particle are supposed to have a damping frequency in the suspension solution. The damped angular vibration behavior of induced electric dipoles associated with a plate-like BSCCO particle can be depicted as shown in Figure 3-11. AC electric force could angularly vibrate this electric dipole along the given axial orientation determined by the cooperation of AC and DC electric fields, while the medium is damping the amplitude of particle's angular vibration. The angular vibration frequency of BSCCO particles should be determined by the acceleration from the applied switching force, i.e., AC electric field strength. The particle angular vibration amplitude is determined by the switching period of the alternative applied force, i.e., AC electric field frequency. As the AC electric field frequency increasing, the angular vibration amplitude of particle is decreasing accordingly. Such decrease in particle vibration angle resulted in higher probability of particle major faces orienting parallel to substrate surface, namely, enhancing c-axis texturing.

3.3.3 DC Electric Field Strength Dependence

Figure 3-12 shows the c-axis texturing dependence on the applied DC electric field strength during ACEPD at constant AC electric field 300 v/cm and 60 Hz, using suspension solution 0.2 g/liter of 0.98 μm average particle size. The

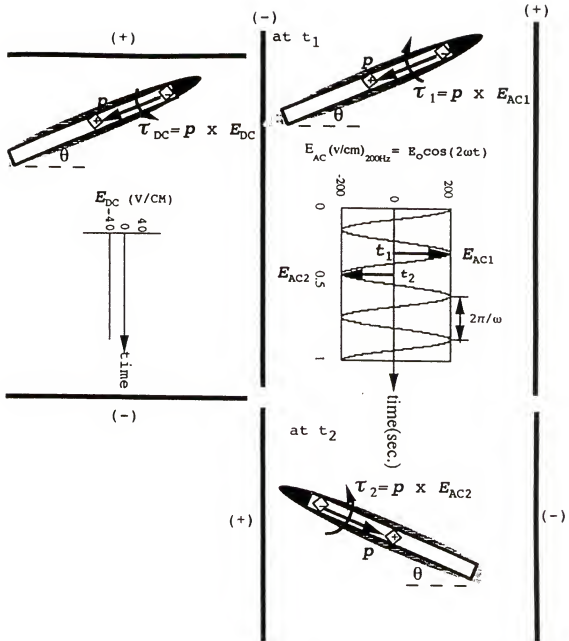


Figure 3-11 The schematic of the interaction between the field-induced effective electric dipole and the applied (a) DC electric field E_{DC} showing no angular vibration, or (b) AC electric field E_{AC} showing the angular switching nature of the electric dipole P .

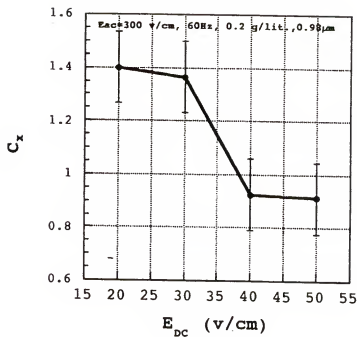


Figure 3-12 The c-axis texturing enhancement factor as a function of the applied DC electric field for modified electrophoretic deposition at E_{AC} 300 v/cm, 60 Hz, using 0.2 g/liter BSCCO dispersion solution of 0.98 μ m average particle size.

resulted curve of C_x versus the applied DC electric field strength indicates that initially C_x (>1) slowly decreases with very low E_{DC} (10~20 v/cm), then C_x more rapidly decreases with E_{DC} of 30~40 v/cm, followed by slow C_x (<1) decreasing with E_{DC} (40~50 v/cm). By interpolating, the critical DC electric field strength to reduce C_x from unit to less than one is at $E_{DC}=38$ v/cm. The critical E_{DC} value should depend on AC field condition and suspension condition.

The observed DC field dependence of C_x can be attributed to the time-averaged orientation of the major face of plate-like BSCCO particles becomes less parallel to the AC field orientation (i.e., substrate surface) with increasing DC electric field strength in the direction perpendicular to substrate surface. Although the E_{AC} strength is much larger than that of E_{DC} , the accumulated acting time in the same direction is smaller for E_{AC} . Thus, critical C_x transition (from c-axis texturing enhancement to degradation) occurs within a small increase in E_{DC} range of 10 v/cm. It is remembered that $C_x = 1$ means the c-axis texture of randomly-oriented plate-like BSCCO powder sample.

3.3.4 AC Field Influence on Average Deposition Rate

During the experiment set of perpendicular AC electric field assisted c-axis texturing, the resultant weight of the deposited BSCCO thick films was measured and deposition time was recorded to determine the average deposition rate. The

relationship between average deposition rate and the applied AC electric field strength was shown in Figure 3-13. From these results associated with the previous experimental results, the plate-like BSCCO particle behavior in modified electrophoretic deposition by the AC field parallel to substrate surface can be further illuminated.

As discussed in the previous experiment set, the c-axis texture enhancement factor C_x increases with increasing applied AC electric field strength, while the average deposition rate [gram/(cm².min.)) also increases with AC field strength (Figure 3-13). This phenomena can be explained by the particle's zigzag migration model at low DC electrophoretic field. The zigzag motion is the result of the particle angular vibration and electrophoretic migration. At low DC electric field (eg., ≤ 40 v/cm) applied in traditional electrophoretic deposition, most BSCCO particles can hardly align their long dimension of major face along the applied DC electric field direction, i.e., the toward-substrate direction. Generally for those plate-like particles with the long dimension of the major face parallel to the migration direction, the migration mobility is the highest compared with the other particle orientations with respect to the net migration direction (that is, DC field direction). Since the particle-geometry-related fluid dynamic drag force have significant influence on particle mobility, but not significant on particle orientation. However, as the AC electric field was increasingly applied, those plate-like

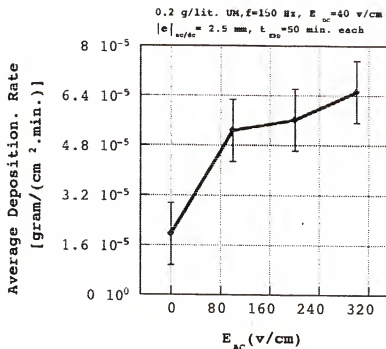


Figure 3-13 The average deposition rate dependency on the applied AC electric field strength at constant suspension concentration, particle size, AC field frequency, DC field, and AC/DC electrode gap

particles orient their major faces closer to AC field orientation in a swimming way, while the particle net migration was still kept forward the substrate surface. As a result, these particles zigzag toward the substrate as schematics shown in Figure 3-14.

Based on the above results and discussions, the schematic model of plate-like BSCCO particle orientation behavior of modified electrophoretic deposition can be concluded in the following paragraphs shown in Figure 3-15. The vertical bars represent the AC electrodes, and the horizontal bars stand for DC electrodes. At t_0 , the particle orientations are random. At t_1 , as strong AC electric field and weak DC electric field are applied to the BSCCO particle dispersion in electrophoretic deposition cell, particle-geometry-preference-induced electric dipole associated with each plate-like particle will align along AC field direction, and angular vibration along a axis parallel AC field, as well as influenced by DC electric field. At this stage, the BSCCO particles have not started electrophoretic migration yet. Until t_2 within half a period of AC polarity reversal, the particle migration begins. At t_3 of the next half period of AC field reversal, the polarity of induced electric dipole switches followed by alternations in the particle migration direction and the angular vibration. Thus, plate-like BSCCO particle migrate in the zigzag manner. Finally, as the particles orient with the long dimension of their major face parallel to substrate surface on the way of electrophoretic

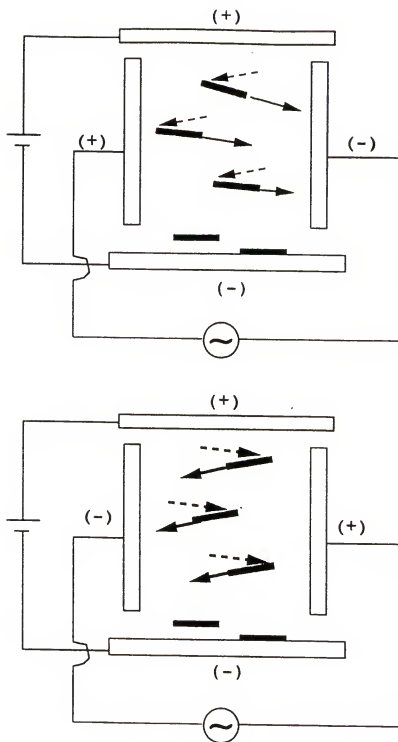


Figure 3-14 The zigzag migration model for AC electric field modified electrophoretic deposition of platy BSCCO particles.

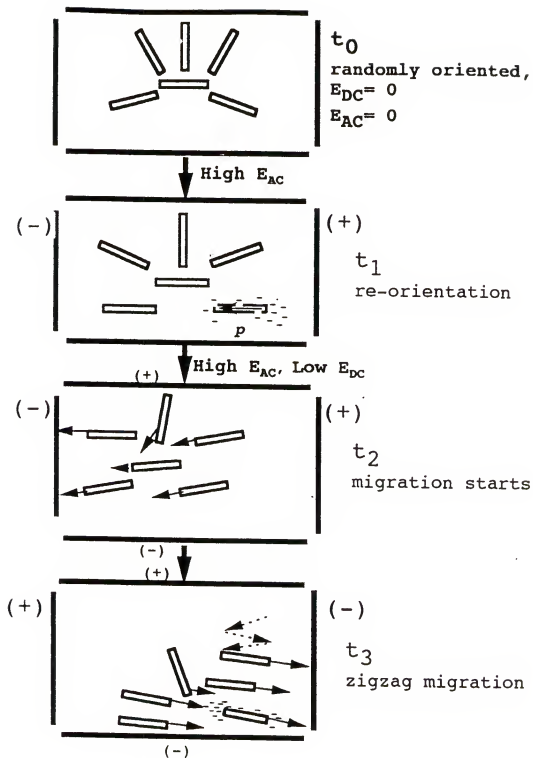


Figure 3-15 The schematics of platy BSCCO particle electrophoretic deposition with AC electric field assisted c-axis texturing enhancement .

migration toward substrate surface, the c-axis textured thick film then can be deposited. Accumulating up to a certain BSCCO film thickness (probably less than a few μm thick), the substrate surface no longer smooth for c-axis texturing, the total C_x could be reduced. So sequential micro-lamination of modified electrophoretic deposition and thermomechanical consolidation should take over the film construction processing.

Figure 3-16 shows the x-ray diffraction patterns of BSCCO thick films with and without additional AC electric field modified electrophoretic deposition. It appears that no obvious raising intensity of c-axis peaks index [001] series in the film prepared with AC field modified electrophoretic deposition, but the c-axis texturing enhancement factor C_x actually higher than that without AC field assistance. This result shows that the c-axis texturing was actually increased with the assistance of the AC electric field parallel to the substrate surface. The fraction of near-c-axis textured plate-like BSCCO particles in ACEPD films should be higher than that without ACEPD. Those near-c-axis texture in ACEPD films can be converted into c-axis via the re-orientation mechanisms by uni-axial mechanical forces during thermomechanical consolidation. Thus, the same TMC condition for ACEPD films resulted in higher c-axis texturing effect with much less particle cracking and bending.

The study of BSCCO suspension stability was conducted and discussed in the next section.

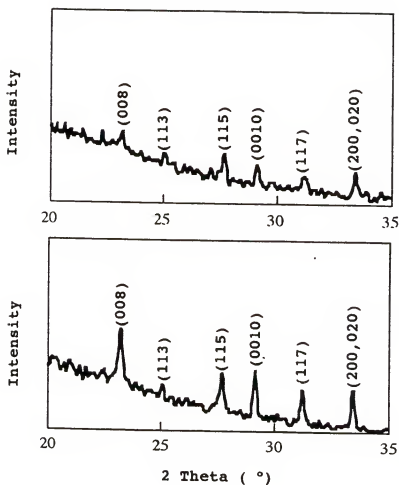


Figure 3-16 X-ray diffraction patterns of the green films prepared via: (a) DC field (40 v/cm) only electrophoretic deposition; and (b) AC electric field modified ($E_{DC}=40$ v/cm, $E_{AC}=200$ v/cm, 200Hz).

3.4 BSCCO Suspension Stability Study

The stable suspension solution is the base for successful electrophoretic deposition. Different organic solvent mediums were used to make BSCCO suspension solutions. The ethanol suspension was found the most stable not only in terms of sedimentation test, but also in the results of Zeta potential measurement data shown in Table 3-1. The measured Zeta potential in ethanol suspension are about 59 mV and 43 mV for BSCCO 2223 phase powder and 2212 phase powder, respectively. Both are much larger than the critical value 25 mV for stable suspension solution. In 25-75 ratio mixed water-ethanol suspension, the Zeta potential for 2223 particles and 2212 particles are 17.3 and 5.5, respectively. These Zeta potential values are too low for stable suspension.

Since surface composition stability in organic medium was also considered, the leaching effects of BSCCO particle was investigated. Using the ICP (Induced Coupling Plasma) analyzer, the dissolubility of tiny amount of particle composition in solutions can be detected. The ICP analyzer detected that very small amount of cations composing BSCCO were dissolved in water shown in Table 3-2. However, in ethanol, the dissolution of cation was not detected. These experimental results displayed that ethanol suspension of BSCCO particles is suitable for electrophoretic deposition. In the other aspect, the water leaching effect on BSCCO

composition lead to acknowledge the environmental attack in the practical service of superconducting tape/wire by moisture. Thus, Ag sheathing appears to be required for fabricating this HTS tape/wire.

Table 3-1 Zeta potential of BSCCO superconductor powder suspensions

HTS Powder	Medium	Zeta Potential (mV)
2223	ethanol	59.1± 0.8
	25-75 water-ethanol	17.3± 2.4
2212	ethanol	43.3
	25-75 water-ethanol	5.5

Table 3-2 Dissolution of cations of BSCCO 2223 and 2212 powder suspensions in 25-75 ethanol-water medium

Sample	pH	Concentration of Dissolved Ion (ppm)				
		Bi	Pb	Sr	Ca	Cu
2223	10.2	1.20	1.00	6.36	4.12	0.25
2212	10.1	1.29	1.00	39.49	19.34	0.26

3.5 Summary

In this study, the systematic investigations of electrophoretic deposition processing parameter effects on plate-like BSCCO particle texturing in as-deposited thick film had been conducted. The particle alignment control in the BSCCO particle suspension solution was found as the key to deposit c-axis texture enhanced films. The cooperation of AC and DC electric fields determine the plate-like particle orientation. Using additional AC electric field parallel to the substrate surface, the c-axis texturing enhancement factor C_x increased with higher E_{AC} strength. Higher AC frequency also was found to increase C_x due to reducing the particle angular vibration amplitude. At a given constant AC field condition, the C_x can be lowered by increasing the E_{DC} strength in low value range. The average ACEPD deposition rate increased with the increasing E_{AC} strength. Conforming the angular motion behavior of plate-like particle, a zigzag migration model was proposed to explain this phenomena. All these ACEPD experimental results were discussed using the physical model schematically illustrated to explain the particle motion behavior in the suspension. The derivation the physical model and computational simulations for the angular motion behavior of plate-like particle were presented in Chapter VI.

It was found that DC electric field can align plate-like BSCCO particle along the field direction, i.e., the longest

dimension of particle's major face aligned with the DC field direction. This is due to the interaction between the particle-geometry-preference-induced electric dipole and the applied DC electric field. The higher the DC field strength, the more particle aligning their major face along the applied electric field, resulting in more particle deposited with their major faces perpendicular to the substrate surface. This experimental result was also confirmed by the experimental result of the decreasing ratio of c-axis to a-axis texture with DC field. The electric flux incident angle experiment further confirmed the particle's major face alignment with the applied electric flux/field. The electrode configuration was improved to ensure the particle orientation control. The dielectrically-shielded edges and the back of EPD electrodes improved the electric flux parallelism. The influences of fluid dynamic force and Brownian motion on BSCCO particle orientation were also discussed in detail, and showed that these forces are negligible as compared with the applied electric force.

The BSCCO suspension solution stability was investigated by Zeta potential measurement and cation dissolubility in suspension mediums. This study provided the base of preparation condition of stable BSCCO suspension. The studies of stable suspension condition effects on EPD texturing showed that low concentration and larger average particle size are favored for the control of particle alignment by the applied electric field.

CHAPTER IV POST-DEPOSITION TEXTURING AND STRENGTHENING

4.1 Introduction

The texturing processing after the electrophoretic deposition can further enhance the c-axis texture fraction in the BSCCO films. These post-deposition texturing processes are thermomechanical consolidation (TMC) and sintering. In the TMC, mechanical force and thermal energy are combined to consolidate the particle films, resulting in increased c-axis texture fraction. The c-axis texturing enhancement mechanism by TMC were investigated and discussed considering the particle texture ratio dependence on the TMC conditions. Schematics were employed to illustrate the inter-particle sliding and thermally-activated particle softening during TMC processing. In sintering texturing study, the effects of particle condition and Ag sheathing on sintering texturing were investigated and discussed. Ag/BSCCO interface was found a favorable site for c-axis grain growth. For tape/wire strengthening study, a silver particle interlayer was two-dimensionally introduced by EPD technique to strengthen the Ag-sheathed BSCCO films. The experiments of sample preparation condition effects on film fracture strength and BSCCO/Ag interface adhesion strength were also investigated. This novel HTS film strengthening method can be used in

continuous fabrication of multifilament tape/wire. The detail of processing, experimental results and discussions in each section.

4.2 Thermomechanical Consolidation Enhanced C-axis Texturing

Consolidation of pre-sintering BSCCO thick films is an important procedure in superconducting tape fabrication. The relationship between processing parameters and c-axis texturing enhancement were investigated for the microstructure controllability study. The studies of conventional dry pressing of ceramic powder bulk usually considered the spherical particle shapes and room temperature situation. Those technologies developed for traditional ceramic processing can not be appropriately applied for BSCCO tape fabrication. The consolidation processing of plate-like particle thick films on metallic substrates needs to be studied with a new view. By analyzing the experimental results, the appropriate thermomechanical consolidation conditions can be integrated into the tape fabrication processing. In the studies of thermomechanical consolidation, the correlation of consolidated microstructure and the TMC processing parameters was investigated to understand the c-axis texture controllability by mechanical force and thermal energy assistance. The effect of the c-axis texture in the as-deposited BSCCO film on thermomechanical consolidation was

investigated for the further microstructure improvement by either thermal and/or mechanical method.

With lower c-axis texture fraction than randomly-oriented powder, the BSCCO powder was electrophoretically deposited at cathode by applying -100 v/cm for 25 minutes using 0.2 gram/liter unmilled suspension at room temperature. Then the sample was cut into 6 square pieces (0.5cm X 0.5cm for each) for this experiment set. This BSCCO films on cut samples were rectangular-shaped with dimension 0.5 cm X 0.4 cm. The larger dimension is parallel to the original axial orientation of the as-deposited film. The initial particle texture and dimensions were the same to all cut samples before thermomechanical consolidation. Being all flat and smooth, the surface of each press die were kept parallel to the substrate surface during uni-axial pressing in order to have uniform pressure distribution. In the second set of experiments, heating during the uni-axial pressing on three BSCCO thick films assists to achieve higher c-axis texturing enhancement than those cold-pressed only. The density of green ceramic body was found to increase with the pressure[Parth⁹⁴] due to reduction in porosity. C-axis texturing effects related to the thermomechanical consolidation processing parameters (pressure and temperature) were investigated. The consolidation temperature influence on angular uniformity of c-axis texturing with respect to BSCCO tape's axial direction was also investigated.

Based on the same initial as-deposited BSCCO thick film microstructure with low c-axis texture, the effects of uni-axial pressure and consolidation temperature on c-axis texturing enhancement were respectively investigated. C-axis texturing enhancement was evaluated by the C_x factor mentioned in Chapter III. The effects of pressure and temperature on resultant superconductivity of Ag-sheathed BSCCO thick films sintered by the same program were also investigated and discussed in Chapter VIII.

4.2.1 Uni-axial Pressure Dependence

Experimental Results:

In the first set of thermomechanical consolidation experiments, the cold pressure effect on particle c-axis texturing enhancement of open BSCCO thick films along the longitudinal direction of the original green tape are shown in Figure 4-1. It is clear that c-axis texturing enhancement factor increases (1.6 to 3.6) with the uni-axial pressure (132 to 528 MPa) in Figure 4-1(a), accompanying that non c-axis texture ratios decrease with increasing uniaxial pressure shown in Figure 4-1(b), although the detail relationship is not linear due to complicated particle re-orienting processes in uni-axial pressure compaction. However, the c-axis texturing enhancement factor seems to approach the saturation value as pressure increases. This is similar to the pressed density dependence on pressure [89Reed1]. On x-ray diffraction patterns, (115) texture peak

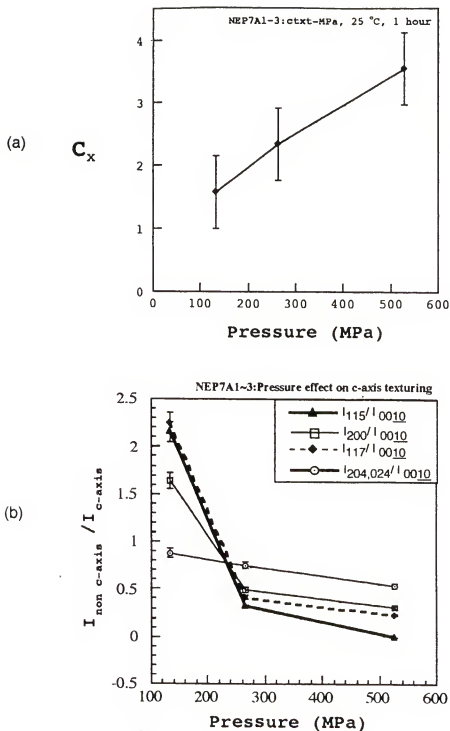


Figure 4-1 The effect of uni-axial pressing on c-axis texturing presented by (a) normalized Lotgering factor, and (b) non-c-axis to c-axis peak intensity ratios versus pressure at room temperature for 1 hour.

even becomes undetectable for the BSCCO film pressed at 500 MPa. Three different pressures (132, 264 and 528 MPa) were applied for cold pressing experiment at room temperature. The average x-ray diffraction peak intensity ratio of $I_{\text{non c-axis}}/I_{\text{c-axis}}$ in the BSCCO/Ag film pressed by 264 MPa is only 28.5% of that by 132 MPa, while that by 528 MPa is 15.4%, . That is 4 times higher pressure resulted in (i) about 6.5 times higher I_{0010}/I_{115} ratios and (ii) 2.25 higher c-axis texturing enhancement factor C_x . In random-oriented sample, the (115) peak is the highest one, and (0010) is the highest one in {001} peaks. As plotted in Figure 4-1(a), the c-axis texturing enhancement effect approached the saturation (maximum $C_x = 4.0355$) with increasing pressure. Since pressed by higher uni-axial pressure, the BSCCO thick films became denser and there was less space for BSCCO particles to re-orient their major faces (parallel to ab-plane) parallel to BSCCO/substrate or BSCCO film/press-die interface.

Discussion:

Besides, only c-axis texture can be effectively enhanced by the uni-axial pressing with pressing die surface parallel to the BSCCO/Ag interface. This is because the geometrical shapes of BSCCO particles are plate-like. With BSCCO/Ag interface and film/pressing-die parallel and approaching to each other, such a uniaxial pressing can re-orient the major faces of plate-like particles parallel to flat faces of the press dies, namely, the substrate surface. For those a-axis

textured particles (i.e. major faces perpendicular to substrate or press die surface) in the as-deposited BSCCO films, the major faces of these particles can be re-oriented parallel to substrate surface due to the film's expanded deformation stains are parallel to substrate surface.

From microscopic view schematic shown in Figure 4-2, the pores always exist above and below the major faces of plate-like particles in the as-deposited BSCCO films, except the particles perpendicular to the substrate/film interface. For the vertical oriented plate-like particles, the BSCCO film deformations are reduction in thickness, i.e., the increased dimension parallel to the substrate/film interface can tilt these vertically-oriented particles and further turn tilted particles into c-axis texture. These pores provide the spaces for plate-like particles to re-orient or to slip the major faces toward parallel to the BSCCO/Ag interface.

However, if the pressure is too high, some BSCCO particles can be bent, or cracked (even into pieces) as shown in Figure 4-3. This pressing-produced particle defects can not be recovered by sintering processing, and affect the sintered film microstructure. The critical current density through the bent zones can be reduced, and even can not pass through the cracked zones. Thus, as discussed in Chapter V, the superconductivity of the sintered microstructure with these particle defects become worse and unstable. Beside the cold pressure effect, the heating temperature on constant pressure consolidation are discussed in the next section.

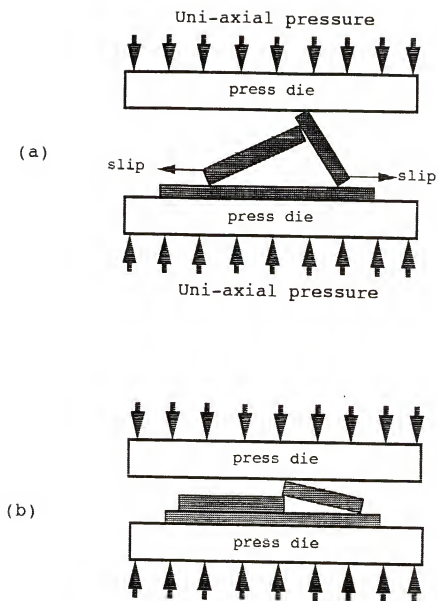


Figure 4-2 The schematic of consolidation enhanced c-axis texturing via platy particle slip mechanism for inter-particle micropore compaction in BSCCO films during uni-axial cold pressing: (a) before and (b) after.

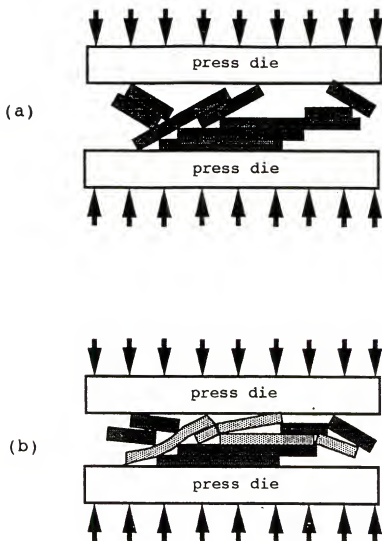


Figure 4-3 The schematic of high-pressure-produced particle bending and cracking: (a) before uni-axial pressing, and (b) pressed.

4.2.2 Consolidation Temperature Influence

Experimental Results:

Heated at different temperatures, the rectangular BSCCO films were then pressed at 500 MPa for 1 hour followed by x-ray diffractometry. As thermal energy provided into the high pressure (500 MPa) consolidation process, the c-axis texturing was enhanced at the temperatures (25°, 200°, 300° and 400°C) much lower than BSCCO-2212 melting point shown in Figure 4-4(a). The samples were initially held at 10 MPa, then pressing dies were heated up. As temperature reaches the designed value, the uni-axial pressure increased again to the set value and was held for 1 hour. During thermomechanical consolidation, the load applied on the press dies and temperature had been monitoring to kept constant. Angular distribution effect on c-axis texturing was also investigated with considering temperature influence.

The melting point of BSCCO-2212 phase is determined as 891°C obtained from Differential Thermal Analysis curves shown in Figure 4-5. The DTA data were measured using TG/DTA Analyzer Model SSI 320 from Seiko Instrument Incorporation. The lower curve indicates that voltage used for heating to keep the controlled temperature. At melting point, isothermal reaction occurred, so that the voltage reach a valley value. As the temperature went up above melting point, evaporation of BSCCO raised up dramatically and; thus, reduced the

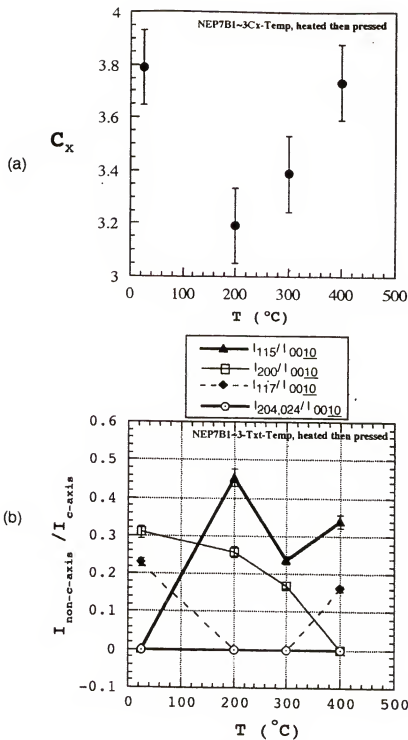


Figure 4-4 The effect of consolidation temperature on c-axis texturing presented by (a)c-axis texturing enhancement factor, and (b) non c-axis to c-axis peak intensity ratios versus temperature at constant uni-axial pressure 500 MPa for 1 hour.

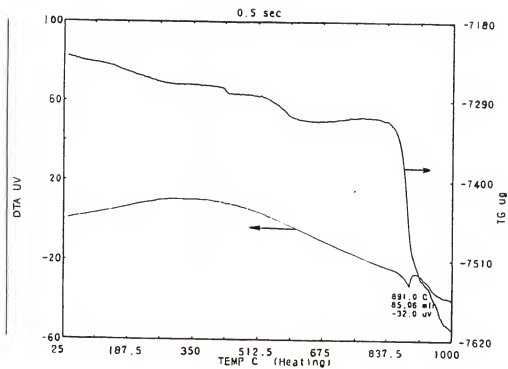


Figure 4-5 The Differential Thermal Analysis curves showing the melting point and weight variation with temperature for $\text{Bi}_2\text{Sr}_2\text{CaCu}_2\text{O}_x$.

voltage of heating current needed to keep the stable temperature.

The c-axis texturing enhancement factor are 3.788 to 3.73 corresponding to consolidation temperature 25°C to 400°C. Comparing C_x values for 200°C and 400°C, the C_x increases only by 17% as the temperature was twice high. This result indicated that the thermal energy has less pronounced effect on c-axis texturing enhancement (at constant high pressure) than the mechanical force at constant low temperature. The C_x values of 3.205, 3.3872 and 3.7402 for the films consolidated at 200°C, 300°C and 400°C, respectively, are slightly lower than that at room temperature. Different from uni-axial pressure effect, the c-axis texturing enhancement dependence on consolidation temperature is upward increasing [Figure 4-4(a)]. Although variation in some data points, the general tendency of the ratios of $I_{\text{non c-axis}}/I_{\text{c-axis}}$ is various with consolidation temperature for this second set of thermomechanical consolidation experiments [Figure 4-4(b)]. Only the consolidation temperature dependence on the ratio of $I_{(200)}/I_{(0010)}$ showed clear decreasing tendency. However, $I_{(115)}/I_{(0010)}$ ratios in the heating-then-hot-pressing films were all higher than that at 25°C. No (024, 024) texture were detectable by x-ray diffractometry in these films. For 400°C heated film, the $I_{(117)}/I_{(0010)}$ and $I_{(115)}/I_{(0010)}$ ratios were increased, while its $I_{(200)}/I_{(0010)}$ ratio decreased to undetectable. Based on these inter-comparison of the ratios of $I_{\text{non c-axis}}/I_{\text{c-axis}}$, it was found that the reduction of (200)

texture contributed the most to the c-axis texturing enhancement in thermomechanical consolidation.

Discussion:

Due to initial heating on BSCCO film before applying 500 MPa, the softened particles at 200°C and at 300°C were more difficult to re-orient to form c-axis texture than those at room temperature.

It is well-known that the mechanical characteristics, such as yield point and elasticity, of all types of materials change with temperature. The mechanical behavior and interactions of BSCCO particles in the films can be influenced as temperature changes. Although no available basic study on thermomechanical behavior of single crystalline BSCCO, the plate-like BSCCO particles still can be treated as rigid flakes under low pressure at much lower temperatures than melting point. For higher temperature cases, the temperature effects on particle deformation and inter-particulate motion in the BSCCO film vary with heating temperature.

In addition to mechanical pressing, thermal energy also dramatically enhances the adhesion strength of BSCCO films after sintering (The results are presented in the later section). It is due to that thermal energy softens the BSCCO particles and substrate. Such softening effect can make particles deformed easilier into compact body by mechanical force. This enhanced mechanical deformation effect with

heating at high pressure can further (i) reduce porosity, (ii) increase the contact area of particles and film/substrate interface, (iii) enhance the inter-particulate bonding and substrate/particle interface adhesion, since high contact stress may cause chemical bonding between two very clean surfaces [89Reed2]. This actual mechanism of the inter-particulate contact area increasing could be resulted from the increased particle plasticity at higher temperature. The mechanism of the interface bonding enhancement can be related to (1) the increased physical binding levels at the interfaces, arising from the atomistic interlocking [Ohr92] of the particle surface structure, and (2) the pressure-enhanced surface interdiffusion [Bach89, Livin90, Ho96, Poa78] in atomistic scale at particle surface layer, if the melting point temperature of BSCCO particle can be descended by high enough pressure.

Larger plastic deformation of hot BSCCO particles by pressing can assist c-axis texturing via bending, squeezing, and twisting actions on plate-like BSCCO particles. Because, at higher temperatures, the thermal-energy-assisted particle deformation mechanisms have further contribution to the additional c-axis texturing enhancement than the mechanisms of inter-particulate slipping and micro-pore compaction only. These particle deformation mechanisms refer to particle bending, squeezing or twisting in the heat-softened polycrystalline film forced by applied pressure at higher temperatures. Unlike consistent texturing dependency on

pressure in Figure 4-1(b), some miscellaneous texture dependence on consolidation temperature are not consistent to each other as shown in Figure 4-4(b). Hotter BSCCO particles have increased plasticity, i.e., no longer treated as "rigid" particles at higher temperature. Starting pressing on such hot and soft BSCCO particles in films has less c-axis texturing enhancement via rigid particle slipping mechanism, since the inter-particulate slipping mechanism requires the "rigid" plate-like particles to play an important role in re-orienting their major faces parallel to substrate surface. In the other hand, the increasing sticking or friction on the contact area between two hot BSCCO particles and at the particle/substrate interface increased at higher temperature due to greater friction on softer contact area[Della91, Jahan94, Miyos88]. The high-temperature-increased friction makes particle slipping more difficult during pressing.

4.2.3 Silver Margin Effect Influence

In fabrication of Ag-sheathed BSCCO film tapes, the silver margins are required for joining the two silver strips at the tape edges. With this kind of film/substrate geometry configuration, the TMC enhanced c-axis texturing would be altered. However, so far, there is few study in this aspect. Therefore, the author conducted the following experiments and discussed the possible mechanism.

Experimental Results:

With rectangular BSCCO film area [Figure 4-6(a)], the angular distribution of c-axis texture decreases with the in-film angle shown in Figure 4-6(b). Two Ag margins are along the 0° direction (longer dimension). 0° in-plane angle is along the original longitudinal direction of film-deposited tape shown in Figure 4-6(a). With the experimental results shown in Figure 4-6(b), the angular distributions of c-axis texture along different in-plane orientations were represented by the c-axis texturing enhancement factors C_x at different in-plane angles. The C_x value generally decreases (from 3.7888, 3.6752 to 3.735) with the in-plane angle. There could be an experimental error in C_x at 45° . That is, c-axis texturing enhancement became more difficult as the in-film orientation gradually rotated from long dimension without Ag margin to short dimension with Ag margins. These results actually indicated that, as in-plane orientation approaching the transverse direction, the angular distribution of non-c-axis texture increases.

Consolidation temperature also influences the angular distribution of c-axis texture in the thermomechanical consolidation. It was also illustrated in Figure 5-6 that the BSCCO film has a greater angular dependence for the film pressed at 400°C than that at 25°C . The C_x value of the cold pressed film is always slightly larger than those of the hot pressed film at each angle. There is 10.7% C_x reduction in the transverse direction (90°) for thermomechanical

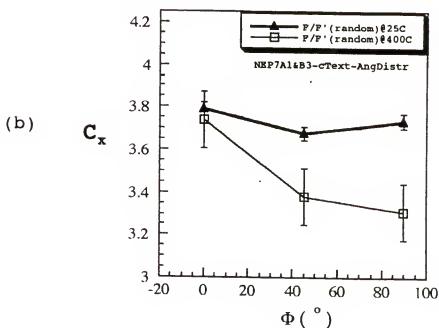
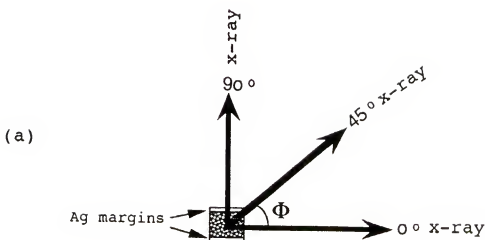


Figure 4-6 The angular distribution of c-axis texture at two different temperature : (a) the schematic of angular relationship for x-ray diffraction, and (b) the curves of normalized Lotgering factor versus in-plane angles in the samples cut from the same electrophoretic deposition tape prepared at a constant uni-axial pressure 500 MPa for 1 hour.

consolidated film at 400°C, while that of cold pressed sample is only 1.3%. The angular dependence of c-axis texturing can be related to the silver margins parallel long dimension orientation shown in Figure 4-6(a).

Discussions:

As the pressure applied through the press die surface, the body deformation of BSCCO film and the substrate can be depicted in the schematic of Figure 4-7. The Ag margins act as blocks hindering the outward in-plane expansion of film along the short dimension (or long edges), while the portion of BSCCO film along the long dimension still can extend to enhance c-axis texturing. At the intermedium angle, the degree of film deformation is also intermedium. Generally within a certain range, the greater in-plane deformation of BSCCO film is, the higher c-axis texturing enhancement can be developed. From the cross-sectional view shown in Figure 4-7 (a), the applied uni-axial load initially thinned BSCCO film and the Ag substrate area beneath BSCCO film, and leaves the Ag margins the same thickness until the pressure on the Ag margin area increases, then all parts thin together. However, as the later deformed Ag margins form as dams, further pressing on BSCCO film made less deformation along the short dimension shown in Figure 4-7(b). This phenomena resulted in in-plane angle dependence of film deformation. This Ag-margin-hindering effect on the angular dependence of deformation ratio in the rectangular thick film should be

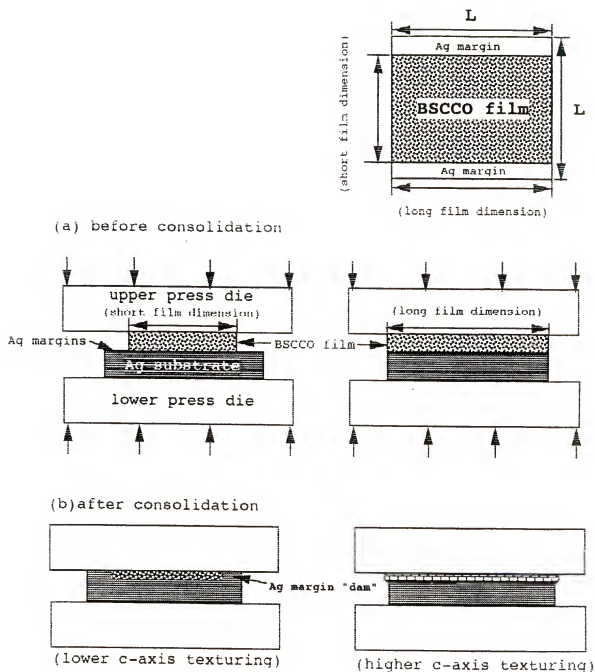


Figure 4-7 The schematic showing reducing effect of Ag margins on c-axis texturing enhancement of BSCCO particles along short dimension in thick film of Ag/BSCCO tape: (a) before pressing and (b) after pressing.

also related to the aspect ratio of the film (length/width). Thus, angular distribution of c-axis texturing has the similar tendency as the angular dependence of deformation ratio in the rectangular thick film.

Surface Morphology of Consolidated BSCCO Thick Films

It is important to report the surface morphology of consolidated BSCCO film where is the deposition site for the next ACEPD process in SMILE method. In Figure 4-8, the 4000 magnification SEM micro-photograph shows the surface morphology of open BSCCO films cold pressed by 200 MPa for 5 minutes at room temperature. There are continuous flat area within the same contour on the surface morphology of BSCCO film. Acting as flat substrate surface, these continuous flat area can favor the c-axis texturing enhancement of BSCCO particles by additional AC electric field modified electrophoretic deposition.

Most of the pinholes and among the continuous flat area has size $\leq 0.5 \mu\text{m}$ smaller than the size of average particle size, and shallow sites are within the depth range of $0.2 \mu\text{m}$. Hence, these pinholes or shallow sites did not significantly affect the c-axis texturing.

The experimental results of Sequential Micro-Lamination of Electrophoretic Deposition and TMC indeed showed the better c-axis texturing enhancement than those prepared by once TMC on the BSCCO film with the same total EPD time.



Figure 4-8 The SEM micrograph showing the surface morphology of a cold pressed BSCCO thick film at 200 MPa, room temperature.

4.2.4 Particle Size Influence

The BSCCO particle size effect on consolidation enhanced c-axis texturing was investigated using open BSCCO films and Ag-sheathed films shown in Figure 4-9. The Ag sheathes merely had very slight effect in increasing C_x values for both particle sizes. For small particle sized ($0.36\ \mu\text{m}$) films, the C_x enhanced by 116% from 1.25 of as-deposited value to 2.7 of consolidation at 200 MPa, 25°C for 5 minutes. In large particle size films, the C_x enhanced by 99.96% from 0.98 of as-deposited value to 2.0 of the same consolidation process. The normalized $\Delta C_x/C_x$ values appear about 16.04% larger for the films with small particle size than those with large particle size, in addition the actually values are larger for the small particle sized films.

Therefore, the c-axis texturing enhancement effect by cold uni-axial pressing is larger for the films with small particle size. This is due to small particles can be easier to proceed the interparticle slipping during the uni-axial mechanical force induced consolidation. In the as-deposited films with small particle size, the inter-particulate pores have comparable sizes as BSCCO particle size. These pores allow small particles to slip into these spaces during consolidation. In large particle size films, most pore sizes are smaller than particle, and the pore size reduced during consolidating. It is more difficult for large particle to perform inter-particle slipping into these shrinking pores at

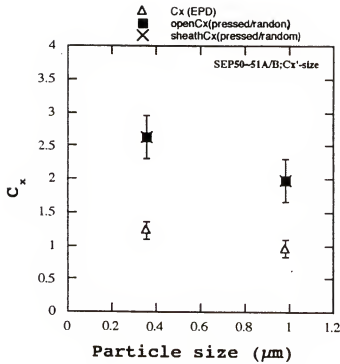


Figure 4-9 The plot of c-axis texturing enhancement factor C_x versus two average particle sizes, $0.36 \mu\text{m}$ and $0.98 \mu\text{m}$ for the open and Ag-sheathed BSCCO thick films as-deposited and pressed at 200 MPa, 25°C for 5 minutes.

intermediate pressure range. At higher pressure range, the large particles can be broken into smaller sized particles, then inter-particle slipping mechanism can provide further consolidation c-axis texturing.

4.3 Sintering Enhanced C-axis Texturing

The sintering effect on the c-axis texturing enhancement of BSCCO films was investigated for systematic study of microstructural controllability of BSCCO tape fabrication. Although pre-sintering microstructure control is the key concern in this dissertation research, as a systematic research, the relation between pre-sintering microstructure control parameters and the sintered BSCCO thick film microstructure also needs to be studied. Thermal energy is treated as the third processing "force" for BSCCO thick film microstructure control. The first one physical force used in this dissertation was electric force used in the first stage of fabrication, electrophoretic deposition of BSCCO particles on silver substrate. Mechanical force was the second physical force employed in compression of BSCCO particles as thick films at the stage of film consolidation. One set of sintering experiment was conducted to investigate the effects of average particle size, Ag sheathing and initial film microstructure on the c-axis texturing enhancement factor C_x via the same sintering processing. For pre-sintering microstructure control, the sequence of these superconducting

tape processing factors can influence the c-axis texturing of sintered BSCCO films. The second set of sintering parameter experiments was carried on to investigate the sintering parameter effects on superconducting characteristics such as transition temperature T_c and its transition ΔT_c . The detailed superconductivity characterization was discussed in Chapter V.

The effects of BSCCO particle size and Ag sheath on the c-axis texturing enhancement of sintered BSCCO thick films were investigated. Deposited by conventional electrophoretic deposition method, the samples prepared with and without Ag sheathes, or with two different particle sizes were simultaneously sintered by the same program [shown in Figure 2-8(a)]. Ag-sheathed BSCCO films were then peeled to expose for x-ray diffractometry. The room temperature consolidation condition was the same for all samples in this experiment set. The resulted C_x values were calculated from the XRD data, and compared to one another.

Experimental Results:

The experimental result shown in Figure 4-10 is particle size effect on c-axis texturing enhancement of sintered BSCCO films by the same sintering program. The average particle size of BSCCO used in this set of experiments were 0.98 μm and 0.36 μm . The consolidation conditions were 200 MPa for 5 minutes at 25°C for all samples. The C_x values of electrophoretic deposition films were 1.223 and 0.954 for

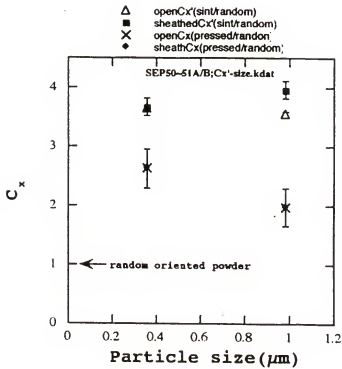


Figure 4-10 The plot of c-axis texturing enhancement factor versus BSCCO particle size for the samples with and without Ag sheathes for as-deposited and sintered stages, showing large BSCCO particle films and Ag-sheathed tapes always have higher C_x .

small and large particle sizes, respectively. The c-axis texturing enhancement factor C_x of the consolidated films with larger particle size is always lower ($C_x=1.9774$) than that ($C_x=2.6265$) with smaller particle size. Using such consolidated microstructure for sintering, the increased percentage of sintering effect on C_x still can be compared.

It is noticed that C_x equal to 4 represents all x-ray diffraction peaks are c-axis series (00L) similar to epitaxial thin film's. The c-axis texturing enhancement factor of open sintered films with small average particle size was 3.6283 slightly (2.1%) higher than 3.5484 for large average particle size. With the same sintering on Ag-sheathed films, the C_x 3.9645 of large particle sized film was found higher (by 8.2%) than 3.6642 for small particle size. The Ag-sheath effect on the rising C_x values of BSCCO films with larger particle size (0.98 μm) is more pronounced (by about 12% more in C_x) than that with smaller particle size (only 0.99% more), although the initial C_x for large particle sized films was lower (75.3% of that for small particle sized films) before sintering. In general, for BSCCO films prepared by conventional electrophoretic deposition at high electric field (lower C_x than random oriented powder), the C_x rising effect by sintering is lower than that by consolidation.

The detail discussion of the BSCCO particle size effect is presented in the next section. The superconductivity characterization results are presented in Figure 5-1, and discussed in Chapter VIII.

4.3.1 BSCCO Particle Size Influence

In this section, the BSCCO particle size effect on sintering enhanced c-axis texture was discussed. The particle size is pertinent to the particle deformation and re-orientation induced by sintering temperature. At sintering temperature, the consolidated particle films become soft and plasticity increases. Introduced by consolidation, the internal stresses are exerting on the near-c-axis-textured particles. Thus, such oriented particles tend to deform in order to relax the stresses. In turn, the particle's major face orienting parallel to the substrate surface, i.e., enhancing c-axis texture. The increment percentage of 12% in sintering assisted C_x value for large particle sized films was higher than that for small particle sized films of 0.99%. During sintering, the particles become soft and thus the inter-particulate pores shrink. Such inter-particulate pore sizes are larger in the larger-particle-sized films, thus larger shrinkage occurred. This leads to the greater c-axis texture enhancement. It could be also due to higher fraction of near-c-axis-textured BSCCO particles in the pre-sintering films with large particle size, i.e., more such oriented particles can be sintered to form c-axis texture. Since, the fraction of randomly-oriented fine particles in pre-sintering BSCCO films can be estimated as the fraction of average background intensity to total peak intensity summation shown in Figure 4-11. Small-particle-sized films actually contend

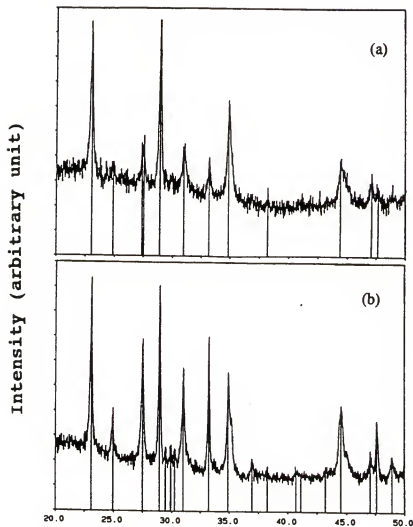


Figure 4-11 The x-ray diffraction patterns for pre-sintering consolidated BSCCO thick films showing the fraction of randomly-oriented fine particle: (a) higher in small particle sized film and (b) lower in large particle size film.

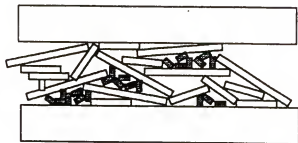
higher fraction (average 10.44% of peak intensity summation) of randomly-oriented fine particles, which can not contribute to c-axis texturing enhancement; while 3.7% of large-particle-sized films indicates less randomly-oriented fine particles.

Since most of large particles can experience the Ag thermal expansion induced stresses, while many small particles at micro-pore sites where the shear stresses due to Ag sheath thermal expansion can hardly reach to re-orient the fine particles as depicted in Figure 4-12. Therefore, the average particle size effect on c-axis texturing enhancement due to sintering processing is more pronounced for large-particle-sized films. Without the second Ag sheath, the BSCCO thick films did not experience more thermal stresses than double-sheathed films, so no further enhancement in c-axis texturing.

4.3.2 Silver Sheath Effect

The higher C_x for Ag-sheathed BSCCO films of both particle sizes results from further BSCCO particle c-axis texturing enhanced with additional Ag sheath during sintering. Considering large particle sized films, Ag sheathed film's C_x was found higher than that of open films. The heat conduction via open film surface is less than that through the Ag/BSCCO interface. Therefore, the sintering enhanced c-axis texturing was reduced for open films. The Ag

(a) pre-sintering BSCCO film microstructure



(b) outward stretched BSCO film microstructure by Ag thermal expansion

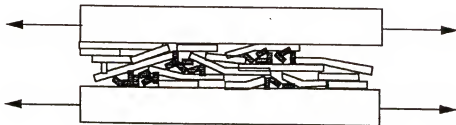


Figure 4-12 The schematic of fine BSCCO particles accommodated in the micro-pore experiencing less effective Ag-sheath thermal expansion shear stresses during sintering-assisted c-axis texturing.

surface contacting BSCCO films acts as a catalytic site for promoting sintering reaction at sintering temperature. Since silver has (i) the most excellent thermal conductor of all metallic materials, (ii) only 0.5% oxygen solid solubility of oxygen, and (iii) difficult oxidizability. Hence, those BSCCO particles contacting Ag surface are preferably to grow up two-dimensionally with ab-plane parallel to Ag surface, i.e., c-axis texturing growth on/near Ag surface as shown in Figure 4-17. The closer to the Ag sheath, the more BSCCO particles grow up as c-axis texture, due to temperature gradient across the BSCCO film. The film temperature closer to the Ag sheath is higher during elevating temperature for sintering. Based on the same principle, the additional Ag sheath provides more contact area for sintering-enhanced c-axis texturing and results in higher c-axis texturing enhancement.

Thermal expansion of double Ag sheathes can also further enhance the c-axis texturing during sintering shown in Figure 4-12. Open BSCCO films had less such thermal effect as Ag-sheathed films. Such in-plane thermal expansion difference induced stress from Ag sheathes during temperature raising could slightly further increase c-axis texture. Because thermal expansion coefficient of Ag sheath is higher than BSCCO particle films [Tenbr94]. The consolidated BSCCO films with two Ag sheathes experience larger in-plane stresses, which tend to two-dimensionally stretch the film outward as heating up, than open films (single Ag sheath). The Ag/BSCCO interface of the consolidated films is capable

of bringing up the thermally induced force to enhance c-axis texturing from the interface toward the film.

4.4 Ag/BSCCO/Ag Tape Strengthening

For many applications of superconducting tapes, the tapes are used in the form of coil, solenoid and toroidal coil. Tension, bending and twisting exist in these forms of applications. Therefore, the mechanical strength of the superconducting tapes is very important for practical applications. Especially, the Ag/BSCCO adhesion strength and fracture strength of Ag-sheathed superconductor thick films are the key to make strong superconducting tapes resistant to micro-cracking, which can interrupt parts of total electric current.

In this study of superconducting tape strengthening, the effects of microstructural factors such as particle size, macrostructure such as film thickness, and fabrication processing such as thermomechanical consolidation on mechanical characteristics were investigated for the understanding the mechanical characteristics controllability. T-peel test was employed to evaluate the adhesion strength and peel fracture strength of Ag-sheathed BSCCO tapes prepared with different method and microstructure.

Since continuous electrophoretic deposition of BSCCO thick films was considered to fabricate superconducting tapes, the way of metallic addition into superconducting

films for tape strengthening by forming metal/BSCCO composites should be also compatible with the BSCCO film deposition method. To strengthen superconducting tapes, a novel fabrication techniques for making multifilament metal-BSCCO composites was developed. The Ag-sheathed BSCCO thick films were strengthened by electrophoretically introducing thin interlayers of fine silver particles into the middle of BSCCO film during the deposition processes. The fine silver particle interlayer should economically and effectively strengthen the superconducting tapes without severely blocking the supercurrent through the BSCCO film, due to only two-dimensional Ag-interlayer to form composite structure. Within this method, particle size effect on strengthening was also investigated. To compare the silver interlayer strengthening effect, the Ag-sheathed BSCCO tapes without silver interlayer were fabricated with the same conditions and tested by T-peel method using the same specimen dimension.

Mechanical characteristics improvement was also related to the tape macrostructural and microstructural modifications in the section of Tape Strengthening. Fine-silver-particle interlayer strengthening effects on mechanical characteristics were discussed related to structural modification of the composite tapes. The resulted superconductivity was presented in Chapter V. In the next section, the detailed silver particle interlayer effect on the fracture strength and adhesion were discussed.

Figure 2-7 (a) shows schematically the Ag/BSCCO/Ag tape fabricated in the present study. To perform T-peel test studies, one end of the Ag sheaths was open in order to form T-shape specimen as shown in Figure 2-7(a). The electrophoretically deposited BSCCO films on two Ag sheets were face-to-face cold pressed and heat treated at elevated temperatures 840°C in 0.21 atm of oxygen ambience for 10 hours, then were slowly cooled to 600°C for 5 hours in 0.17atm O₂ ambience. The SEM cross sectional view of a fabricated Ag/BSCCO/Ag tape is shown in Figure 4-13. As seen in cross sectional view, the total thickness of BSCCO film is 10 μm and the Ag sheath thickness is 25 μm for each.

4.4.1 Average Particle Size Effect

Before studying Ag particle interlayer strengthening effect, the BSCCO particle size effects on the adhesion strength and T-peel fracture strength of Ag/BSCCO/Ag tapes were investigated as the microstructural bases of tape strengthening effects. The experimental results and discussions are presented in the following sections.

The experimental results are presented in the following paragraphs.

Without Ag-interlayer, one set of specimens were fabricated using two different particle sizes. After T-peeled, the fracture was examined by x-ray diffractometry. Figure 4-14 (a) and (b) are the XRD patterns of peeled

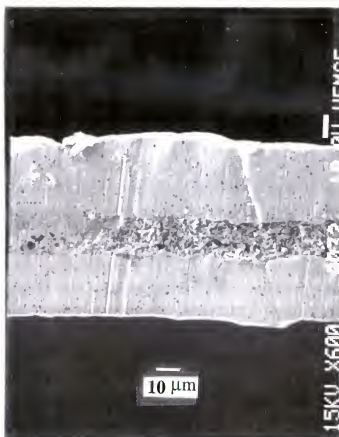


Figure 4-13 Scanning electron Microscopy cross-sectional view of Ag/BSCCO/Ag tape.

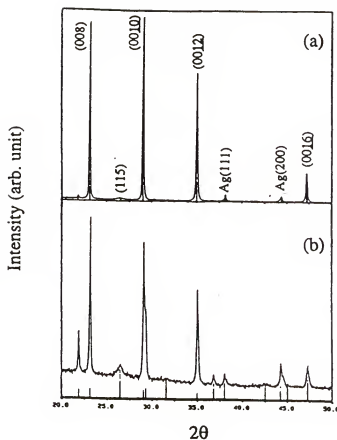
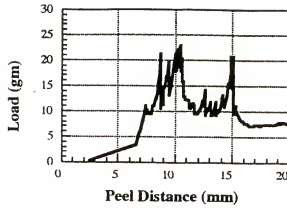


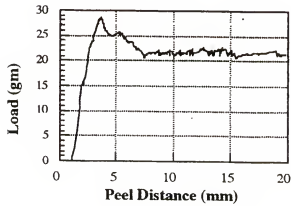
Figure 4-14 The x-ray diffraction patterns of peeled Ag/BSCCO/Ag tapes fabricated using BSCCO powders with average particle size of (a).98 μm and (b) 0.36 μm .

Ag/BSCCO/Ag tapes fabricated using two dispersion solutions having BSCCO powders with 0.98 μm and 0.36 μm particle sizes, respectively. All specimen dimensions of both kinds of films were the same and XRD conditions were also conducted consistently. The figure shows that both kinds of Ag-sheathed BSCCO films are predominantly c-axis oriented. However, the films fabricated using BSCCO powder of smaller particles (labeled as C2) have higher intensity ratios for the background noise, although the intensity ratios of c-axis peaks to miscellaneous peaks were higher than the other sort of BSCCO films. This high XRD background noise is contributed by many fine BSCCO particles with randomly orientation. The films fabricated using BSCCO powder of larger particles (labeled as C1) exhibit some non-c-axis peaks of higher intensity ratios, but the noise level is much lower. We envisage that the c-axis preferential orientation in BSCCO films deposited using larger sized powder solution is brought about by higher c-axis texture ratio in as-deposited BSCCO films.

The mechanical characteristics of the sintered Ag/BSCCO/Ag tapes was evaluated with the T-peel tests on each sample. All T-peel test geometry and experimental condition were kept the same so that the maximum load (P_{max}) at which the fracture initiates, and the fracture propagation load (P_L) which approaches roughly constant value, can be compared. The peel load as a function of peel distance are plotted in Figure 4-15 for both large and small particle sized samples



(a)



(b)

Figure 4-15 The T-peel test curves of Ag/BSCCO/Ag tapes of 10 μm thick films with average BSCCO particle sizes of (a) 0.98 μm and (b) 0.36 μm .

(C1 and C2, respectively) without Ag-interlayer. In these experiments, the samples yielded by fracturing through the superconductor film bulk but not at BSCCO/Ag interface. This was confirmed by BSCCO films remaining on both peeled pieces. The figures also shows that the P_L and P_{max} values of C2 (21 g and 29 g, respectively in Figure 4-15 (b)) are considerably higher than those of C1 (7 g and 23 g, respectively in Figure 4-15 (a)). The higher peeling loads required for small particle superconductor samples suggest that smaller particle-sized samples possess better mechanical characteristics. There are fewer peaks observed in the T-peel test curves due to more uniform microstructure with less and smaller micro-pores (which act as the flaws easier for fracture initiation and propagation), and with higher fraction of fine grains with random orientation.

The surfaces of the fractured films were examined by SEM. Analogous to the fracture toughness behavior of anisotropic $YBa_2Cu_3O_{7-x}$ system studied by Raynes et al. [Rayne91], most of the smooth fracture along the ab-basal plane grain boundaries in sample C1 can be classified as intergranular fracture shown in Figure 4-16(a), while most of the rough fractures in sample C2, appearing as terraces and kinks shown in Figure 4-16(b) [Menci92,Hertz83]. SEM fracture micrograph shows no cracks in BSCCO grains for both kind of samples (prepared using two different size BSCCO powders) even though films were bent during the peel test producing a bending strain of approximately 1%. Such

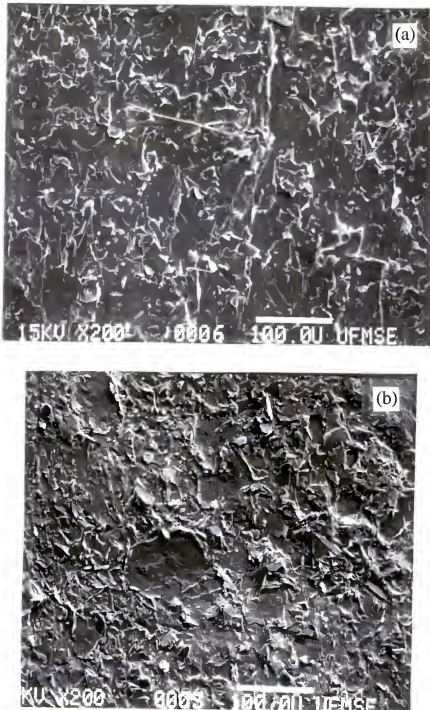


Figure 4-16 The Scanning Electron Microscopy fracture microphotographs of Ag/BSCCO/Ag tapes fabricated using BSCCO powders with average particle size of (a) $0.98\ \mu\text{m}$ and (b) $0.36\ \mu\text{m}$.

improvement in mechanical flexibility of superconducting tapes based on high- T_c superconductors is very important for technological applications.

The experimental results are discussed in the following paragraphs.

The particle size effects on the BSCCO/Ag adhesion strength and T-peel fracture strength of the Ag-sheathed BSCCO films without Ag-interlayer were discussed at the beginning.

Very fine BSCCO particles in smaller particle sized films seem to be preferentially randomly-oriented as deposited, and are more difficult to enhance c-axis texture by mechanical consolidation due to such fine sized particles can easilier fit into the micro-pores where they experience less mechanical stress for c-axis texture re-orienting. Although fine spherical particles should have enhanced driving force for grain growth due to higher surface to volume ratio of smaller particles [Kinge76], plate-like BSCCO particles preferentially two-dimensionally grow along ab-plane [Sche93, Kawas94], the above high surface-to-volume-ratio effect can hardly take action for fine plate-like particles.

It is noted that ab-plane has weakest fracture toughness [Raynes91]. Since fine particle sized BSCCO films (C2) consist of more randomly-oriented grains (very fine), i.e., less gains orient with their ab-plane parallel to the fracture propagation direction (referred to Figure 4-14), T-peel fracture propagation is expected to go through less ab-planes

of grain and along less ab-plane grain boundaries. In addition, very fine grains filling micropores lead to denser and more uniform microstructure with fewer flaws. These flaws were known as the sites for propagating stress-concentration-induced fracture [Menc92].

In general, strength of ceramics are inversely proportional to grain size [Sin93]. Therefore, the BSCCO films prepared from finer particle size should generally also be stronger.

4.4.2 Silver Particle Interlayer Strengthening

The introduction of a silver interlayer between fine-BSCCO-particle films in the configuration Ag/BSCCO/Ag was marked by a significant improvement in the mechanical properties of BSCCO tapes. The resultant sandwich configuration is then represented as Ag/BSCCO/Ag-particles/BSCCO/Ag (samples named C3) using small BSCCO particles. The thickness of Ag interlayer was estimated to be $\leq 1 \mu\text{m}$ based on SEM cross-sectional view which was recorded prior to sintering of the samples. The P_{max} and P_L of BSCCO tapes having an Ag-interlayer were found to be 80 g and 40 g, respectively shown in Table 4-1. These values of P_{max} and P_L are much more higher than those ($P_{\text{max}}=29 \text{ g}$ and $P_L=20 \text{ g}$ for C2) for BSCCO tapes fabricated without Ag-particle interlayer from same size ($0.36 \mu\text{m}$) BSCCO powders. The values of P_{max} and P_L , 39 g. and 18 g., respectively, are also increased for large BSCCO particle sized Ag/BSCCO/Ag-particle/BSCCO/Ag

Table 4-1 The comparison of adhesion strength of Ag-sheathed BSCCO tapes prepared with and without fine Ag-particle interlayer at the middle of BSCCO thick film.

BSCCO Particle s i z e (μm)	Ag particle Interlayer Thickness (μm)	P_{Max} (gm)	P_{Level} (gm)
0.98	0	23	7
	1	39	18
0.36	0	29	21
	1	80	40

films (as C4). With fine Ag particle interlayer, the P_{\max} and P_L of C3 increased to 276% and 190% of C2's, respectively; while the P_{\max} and P_L of C4 increased to 170% and 257% of C1's, respectively. That is, the fine Ag particle interlayer has higher strengthening effects on T-peel fracture (P_{\max}) of small BSCCO particle films, and on adhesion (P_L) of large BSCCO films.

Discussions:

The improvement in the toughness of BSCCO tapes by means of Ag composite is believed to be brought about by the modification in the microstructures of BSCCO films during sintering in presence of Ag-particles. The BSCCO grain size of Ag-consisted film may have been slightly larger[Sin93, Park95]. These reports were confirmed in the Figure 4-17. This optical microscopy photograph taken at 1000 magnification showed those BSCCO grains at Ag substrate two-dimensionally grew up (observed at film opening area). The modification in the microstructure is due to following roles played by silver: (1) joining the neighboring BSCCO grains within the deformation concentration zone (within the middle zone of the film thickness), (2) increasing the resistance[Nishi89] to intergranular fracture by strengthening fine BSCCO grain boundary network, (3) increasing the homogeneity of formation of grains with improved size, and (4) redistribution of the stresses of fracture zones by Ag-particles.

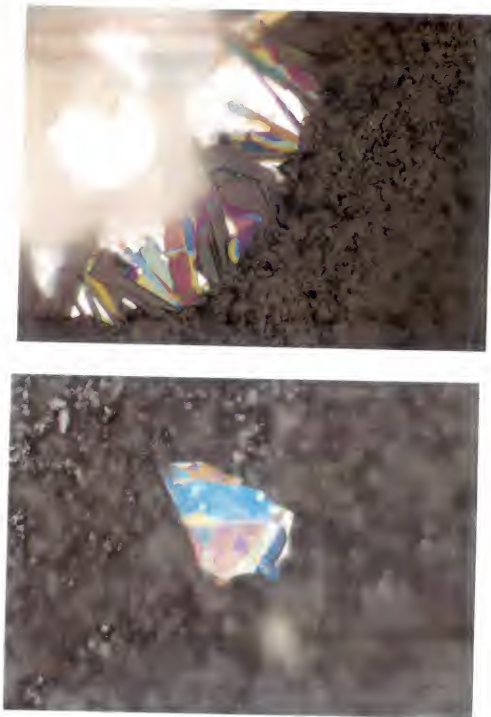


Figure 4-17 The optical microscopic photographs showing BSCCO thin film formation (colorful area) at the Ag/BSCCO interface revealed from the openings of BSCCO thick films (black area).

Additionally, with such high concentration Ag particles at the middle of BSCCO film, Ag can form network along BSCCO grain boundaries. this kind of high Ag-volume-ratio composite has excellent mechanical properties[*Sin93i, Sin93ii, Yun93, .*]. The smaller the BSCCO particles, the finer the Ag network; thus, the supposed stronger mechanical characteristics the Ag-BSCCO composites should be.

4.4.3 BiSrCaCuO Film Thickness Influence

The T-peel fracture strength and adhesion strength of Ag-sheathed BSCCO tapes can be influenced by possible microstructure uniformity across the polycrystalline BSCCO film thickness. This study was conducted to investigate the T-peel fracture strength and adhesion strength of Ag-sheathed BSCCO tapes with half BSCCO film thickness.

Experimental Results:

As expected in the experimental design, the reduction in BSCCO film thickness resulted in adhesion strength enhancement of the Ag/(5 μm)BSCCO/Ag tapes fabricated via cold uniaxial pressing then sintering using BSCCO powder with average particle size of 0.36 μm shown in Figure 4-18. From this T-peel test curve, it was found that the peak load P_{max} was 56 gram, about 2 times of that with double BSCCO film thickness 10 μm . This indicates that the T-peel fracture of the tapes has been strengthened with thinner BSCCO film

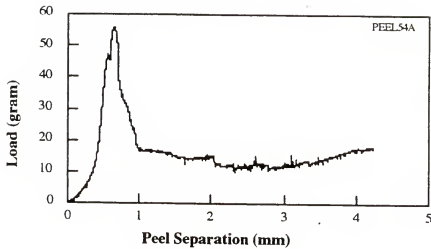


Figure 4-18 The T-peel test curve of the Ag-sheathed BSCCO thick film with 5 μm thickness prepared from 0.36 μm fine particle showing higher adhesion strength and better uniformity than those of 10 μm thick film.

thickness. The level-out load P_L for 5 μm thick film was 18 gram similar to that with 10 μm BSCCO thickness. The adhesion of BSCCO on Ag substrate is still strong enough, since BSCCO films were still found on both sides of peeled tapes. No multipeak found in this T-peel test curve indicates that the adhesion strength is relatively uniform along the longitudinal direction of the tape, implying that microstructure uniformity along the longitudinal direction of the tape is also better with reduced BSCCO film thickness.

Discussions:

Although the same conditions for BSCCO particles, consolidation, sintering and tape structure, the tape adhesion strengthening by BSCCO film thickness reduction can be related to the possible gradual change of BSCCO film microstructure receding from the Ag/BSCCO interface to middle of the BSCCO film. Approaching the Ag/BSCCO interface, the microstructure density can be gradually increased. BSCCO thin films were found at the Ag/BSCCO interface from the polarized optical microscopic photographs shown in Figure 6-5. The BSCCO thin film can be revealed as the colorful area in the openings of BSCCO thick films. This phenomena of thin film formation at Ag/BSCCO interface suggested that Ag surface could be as a "catalytic site" for BSCCO particle's two-dimensional growth along the ab-plane of BSCCO crystallographic structure by lowering the melting point of BSCCO. The Ag/BSCCO interface also acts as thermal energy

providing site for sintering. Since silver has Ag has the highest thermal conductivity among metals and alloys, high oxidization resistance, and limited oxygen solid solubility of 0.5 %.

The initial microstructure of BSCCO thick film can be gradually densified as approaching the Ag/BSCCO interface, due to the depth wise degradation of mechanical consolidation in the thick films receding from the surfaces of press die i.e., actually silver substrate.

4.4.4 Consolidation Temperature Influence

Thermal energy was considered to apply for improving pre-sintering BSCCO film microstructure. In the previous sections of tape strengthening experiments, the samples were prepared by cold pressing and sintering at the same conditions. Thermomechanical consolidation was employed for sample preparation in this set of experiment. The only difference in tape processing is heating during consolidation.

Experimental Results:

As 5 μm thick BSCCO film in Ag/BSCCO/Ag tapes were thermomechanical consolidated at 300°C for 1 hour, the resulted adhesion strength were dramatically enhanced shown in T-peel test curve of Figure 4-19, although the large particle size of 0.98 μm was found weaker ($P_{\text{max}}=23$ gram, and $P_L=7$ gram) for 10 μm thick film prepared by cold pressing.

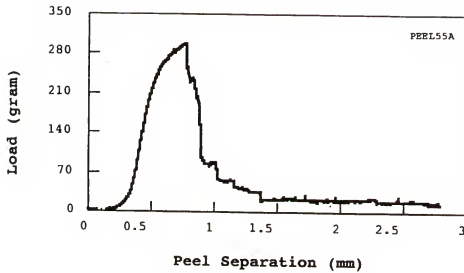


Figure 4-19 The T-peel test curve of Ag/(5 μm)BSCCO/Ag tapes fabricated via thermomechanical consolidation then sintering using BSCCO powder with average particle size of 0.98 μm .

The peak load P_{\max} is 300 gram which is 13 times higher than that with 10 μm BSCCO film thickness. Without multipeak feature in the T-peel test curve, the level-out load P_L of the curve is 25 gram, about 3.6 times higher than that cold pressed samples of double thickness.

Even though the film thickness reduction may have contribution in enhance T-peel fracture strength, the strengthening factor of thickness reduction effect is merely double in P_{\max} , while the P_L even slightly decreased. Hence, the film adhesion strengthening is primarily contributed by the improved microstructure by thermomechanical consolidation processing. Besides, the BSCCO films made from larger average particle size (0.98 μm) supposed to be weaker T-peel fracture strength and adhesion strength than that from smaller particle size (0.36 μm). The particle c-axis texture fraction (0.9804) of the BSCCO thick films used in this experiment set is similar to that (0.9824) of cold pressed samples.

Discussions:

It was well known that the consolidation effectiveness in the powder bulk is lower for the larger average particle sized films than that for smaller average particle sizes film, due to (1) inherently larger pores among larger particles, and (2) smaller sized particles is generally easier to slip into interparticulate pores. Therefore, the additional thermal energy contributed more adhesion strengthening effect than merely mechanical consolidation.

The significant improvement in tape adhesion strength can be attributed to the improved pre-sintering BSCCO film microstructure with reduction in number density and size of micro-pores and increased inter-particulate contact area. Sintering such improved pre-sintering BSCCO film of samples could produce more uniform and denser film microstructure. Such a microstructure of sintered Ag-sheathed BSCCO film was more effectively improved by thermomechanical consolidation, although almost no change in the particle c-axis texture fraction.

4.5 Summary

C-axis texturing enhancement effects of uni-axial pressure and consolidation temperature were investigated for understanding the microstructural controllability of pre-sintering BSCCO thick films. The density and film/substrate adhesion strength of films can be increased by consolidation at higher temperature. The reduction of (200) texture was found to contribute the most to the c-axis texturing enhancement by thermomechanical consolidation. Considering the consolidation temperature influence, the macrostructural effect of open film tape on the angular distribution of c-axis texturing enhancement was also studied. The effect of the as-deposited BSCCO film microstructure on thermomechanical-enhanced c-axis texturing showed that film prepared by AC-electric-field-modified electrophoretic deposition had better microstructural controllability by

thermomechanical consolidation than that by strong-field electrophoretic deposition. Though capable of increasing film density and c-axis texture, higher uni-axial pressure at room temperature can result in worse consolidated film microstructure for later sintering due to particle cracking. Such particle structure defects may not be cured by later sintering process and result in superconductivity stability problem (discussed in Chapter VIII). Pressing started at higher temperatures had slightly lower the c-axis texturing enhancement effect than that at room temperature. However, greatly above room temperature, the higher the temperature, the higher the c-axis enhancement effect resulted by thermomechanical consolidation. Silver margins hindered the expansion of open film under uni-axial pressure, thus, the angular distribution of c-axis texture resulted in the pressed BSCCO films. The angular distribution effect became more pronounced as hot film was pressed. There was even less film extensive deformation in the short dimension with Ag-margins at high temperature before pressing started due to less micropore compaction and difficult inter-particulate slipping as the thermal-induced softening effect of particles increases.

Through these studies, the c-axis texturing enhancement controllability by thermomechanical consolidation parameters was illuminated. Tape macrostructure was also found to significantly influence c-axis texturing distribution, as well as the consolidation temperature. The ways to

consolidate BSCCO film during building up the thick film are actually important in microstructure control of the pre-sintering Ag-sheathed BSCCO tapes.

The control factors for pre-sintering microstructure were found to influence the c-axis texturing enhancement of sintering. BSCCO particle size and Ag sheathed structure were used as these control factors. Pre-sintering films with large particle size resulted in higher degree of sintering-assisted c-axis texturing enhancement effect due to (i) greater fraction of near-c-axis-textured particles in the pre-sintering microstructure according XRD results; (ii) lower fraction of randomly-oriented fine particles indicated with less average fraction of background noise in XRD; (iii) more susceptible to the outward shear stresses in BSCCO film induced by large thermal expansion coefficient difference between Ag and BSCCO film during raising temperature; (iv) less fraction of fine particles accommodated in micro-pores sites where experience less mechanical forces for particle re-orientation. Ag sheathes have slightly higher c-axis texturing enhancement of BSCCO thick films than that of open films. The closer the BSCCO particles to Ag sheathes the easier the c-axis texturing growth of BSCCO grains, due to the Ag surface contacting the BSCCO particles acting as the two-dimensional growth enhancement site for plate-like grains supported in Figure 6-5. Based on these experimental results, it can be concluded that the Ag sheathes and large size (0.98

μm) particles for preparing pre-sintering BSCCO films had more advantages in c-axis texturing enhancement by sintering. The strengthening effects of fine silver particle interlayer, BSCCO particle size, BSCCO film thickness and fabrication processing factor were studied to improve the T-peel fracture and adhesion strengths. Ag-particle interlayer introduced into BSCCO thick film was found capable of improving the mechanical characteristics by about double times at lower fabrication cost and being compatible the BSCCO films deposition method. Without Ag interlayer, the small particle sized films had 3 times higher adhesion strength revealed by level-out load P_L in T-peel test curves than that of large particle sized Ag-sheathed BSCCO tapes, as the T-peel fracture strength of small particle films had about 1.3 times higher than that of large particle films. The Ag particle interlayer had higher enhancement effect on tape adhesion strength for large-BSCCO-particle films, and higher enhancement effect on T-peel fracture strength for finer BSCCO particle films. Improvement in pre-sintering BSCCO film microstructure was found to improve the mechanical characteristics of Ag/BSCCO/Ag tapes via thermomechanical consolidation. This is due to the reduction in size and number density of micro-pore. Even large-BSCCO-particle films exhibited excellent enhancement effect on mechanical characteristics by thermomechanical consolidation on pre-sintering tapes. BSCCO film thickness also played an important role in mechanical characteristics of Ag-sheathed

BSCCO films, because the microstructure density and BSCCO grain size across the film thickness increased as closer to the BSCCO/Ag-substrate interface. Similarly, the fine Ag particle/BSCCO composite formed in the middle of the BSCCO tapes can more effectively strengthen the tapes with small BSCCO particle size, since the silver distributed in the finer and denser boundary network and eliminated the micro-pores which act as fracture initiator.

CHAPTER V

SUPERCONDUCTIVITY CHARACTERIZATION

5.1 Introduction

The superconducting characteristics Ag-sheathed BSCCO films were measured to related to the pre-sintering microstructure control and sintering parameters. All sintered specimens were magnetically characterized by SQUID magnetometry. The measured magnetization hysteresis loops were used to calculate the critical current density J_c based on Bean critical state model at different conditions. The measurement of AC magnetic susceptibility versus temperature was used to characterize the paramagnetic-diamagnetic transition, standing for the normal-superconducting transition. The critical temperature T_c and the critical temperature transition ΔT_c then were determined from the transition curve. This magnetic characterization method has the advantages of (i) capable of simultaneously measuring magnetic and temperature dependencies, (ii) anisotropy sensibility, and (iii) two-dimensional measurement of critical current density.

Prepared by AC-field-modified electrophoretic deposition, the pre-sintering microstructures of BSCCO films resulted in better superconductivity stability of fully processed films. With and without improved pre-sintering

microstructures by MEPD, the J_c dependencies of Ag-sheathed BSCCO thick films on temperature and on applied magnetic field were characterized and compared. The attribution to these differences in superconductivity stability was related to the as-deposited film microstructure. Then the sintered microstructures were correlated to pre-sintering microstructure control. In addition to c-axis texturing enhancement, the defects in BSCCO grains and grain boundaries were considered to explain the relationship between superconducting characteristics and pre-sintering film microstructure control.

It is important to understand the relation between the pre-sintering processing parameters and the superconductivity of finally processed BSCCO films.

Considering BSCCO particle aspect ratio effect as a pre-sintering microstructure control factor, the particle size effects on the tape superconductivity were investigated for the base of polycrystalline thick film microstructure. The intragranular critical current density is related to the particle aspect ratio. The J_c for c-axis textured grain colonies is also related particle aspect ratio. Larger particle aspect ratio is preferred for forming better inter-colony connection. Processed with the same conditions, pre-sintering film microstructures with two particle sizes led to significant difference in superconductivity of fully processed films, although the critical temperatures were the same and c-axis textures were similar.

The effects of thermomechanical consolidation parameters on J_c , ΔT_c and characteristic magnetic fields were investigated. Uniaxial pressure and consolidation temperature were employed as the thermomechanical consolidation parameters, respectively.

As an important superconducting tape fabrication processing factor, the sintering parameter effect on T_c and magnetization hysteresis loop shape were also characterized. AC magnetic susceptibility was measured at different temperature for this critical temperature characterization.

Magnetic hysteresis loops were analyzed to evaluate the superconductivity related to film microstructure. As the magnetic field is increasing in positive direction, the magnetization is negative due to Ampere's Law; vice versa. Away from the magnetization peak, the magnetization rapidly decreases, then increases with the applied magnetic field. At this decreasing-to-increasing transition point, the applied magnetic field H_{pene} starts to laterally penetrate from the normal conducting flux core into the type-II superconductor films, then move the magnetic flux vortex lines. The magnetic field H_{pene} corresponding to this transition point can be also used to indicate degree of penetration depth. The penetration depth is related to the degree of coupling between ab-plane grain boundaries parallel to tape surface. Thus, H_{pene} can be the applied magnetic field at the intergranular-to-intergranular penetration transition. H_{c2} is related to the maximum pinning force density for flux vortex lines, that is,

as normal conducting vortex cores start to overlap and penetration depth diverges. H_{peak} is the level of magnetic potential to induce maximum current density at the critical state. The maximum magnetic flux vortices are generated at the critical current density. H_{peak} can be employed to indicate the grade of supercurrent path link, i.e., intergranular coupling in this study. The lower the H_{peak} , the better the supercurrent path link. Beyond H_{peak} , the flux vortex lattice pinning potential starts to decrease with increasing applied field. This resulted in that supercurrent density decreases with the applied magnetic field at this stage.

5.2 Superconductivity Stability Improvement by ACEPD

The effect of the pre-sintering microstructure on the superconductivity stability of fully processed Ag-sheathed BSCCO thick films was investigated and compared. With and without additional AC-field modified electrophoretic deposition, c-axis texturing enhancement during the BSCCO particle deposition is the most important stage for the pre-sintering microstructure control. The superconductivity stability is contributed by the intragranular component and intergranular component. The experimental results showed which component could be more sensitive to the temperature or magnetic field changes, and how the dependency are. Based on

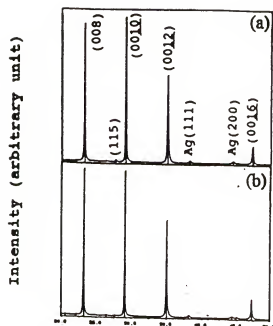
the experimental results of the particle size effect study, the large particle size $0.98\text{ }\mu\text{m}$ was used in this sets of experiments. The specimen dimensions and processing parameters for thermomechanical consolidation and sintering were the same. The electrophoretic deposition parameters were the same, except whether the additional AC electric field had been applied. The detailed processes was described in Chapter III. The following sections are the experimental results and discussions about the superconductivity characteristics relating to the film microstructure.

Figure 5-1 showed the X-ray diffraction patterns of the peeled Ag-sheathed BSCCO thick films prepared with and without AC-electric-field modified electrophoretic deposition. Although the XRD patterns appear similar and the c-axis texturing enhancement factors for both kinds of films are close, the microstructure of the film by modified electrophoretic deposition should have much less microcracking and grain bending, resulting in stronger coupling among BSCCO grains and more supercurrent paths in the film after sintering.

5.2.1 Temperature Dependence

The experimental results are discussed in the following.

Figure 5-2 showed the temperature dependencies of maximum magnetization for the films with and without AC-electric-field modified electrophoretic deposition. Obviously, the films prepared by AC-field modified



20

Figure 5-1 The x-ray diffraction patterns of peeled Ag-sheathed BSCCO thick films prepared by the same thermomechanical consolidation and sintering conditions and the electrophoretic deposition (a) with and (b) without AC-electric-field assisted c-axis texturing.

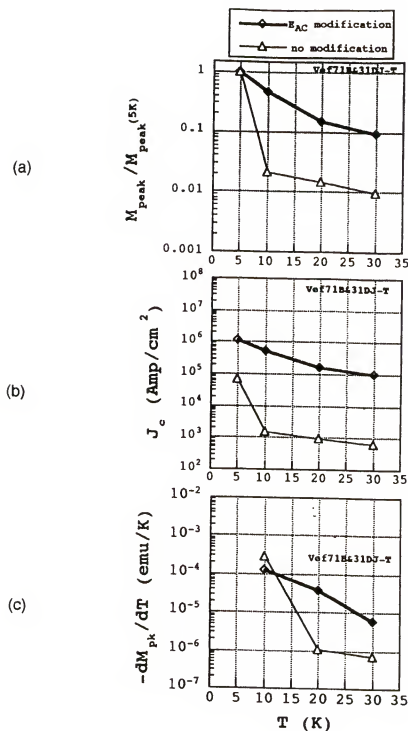


Figure 5-2 The temperature dependence of (a) normalized magnetization, (b) critical current density, and (c) peak magnetization decreasing rates of Ag-sheathed BSCCO thick films prepared by electrophoretic deposition with and without AC-electric-field assisted c-axis texturing.

electrophoretic deposition had superior superconductivity stability with respect to temperature variation, since the slope of the magnetization versus temperature is smaller [Figure 5-2(a) & (c)] at low temperature. Especially, the critical current density of AC-modified films showed 1 to 2 order higher magnitude in J_c as about $10^6 \sim 10^5$ Amp/cm² in Figure 5-2(b), while those without AC-modification are from less than $8 \times 10^4 \sim 7.5 \times 10^2$ Amp/cm². The initial slope is much larger for the later. The magnetization values and J_c of the film with AC-electric-field-modification are always larger than those without.

The general temperature dependence of the slope temperature derivative with respect to temperature is larger for AC-modified films, except at low temperature range (5-10K) shown in Figure 5-2(c). The lower the slope temperature derivative, the more stable the film encounters temperature change. These slope temperature derivative dependencies on various temperatures for both kind of films are opposite to each other: downward for AC-modified films and upward for the other. That means, as temperature increases, the J_c of the AC-modified film had less reduction with temperature than the other's.

The temperature dependence of penetration field H_{pene} is shown in Figure 5-3(a) for both kinds of films. The H_{pene} of the films by AC-field modification is always higher (6000-80 Gauss) than those (4000-40 Gauss) not by AC-field modification at the temperature range 5-30 K; namely, the

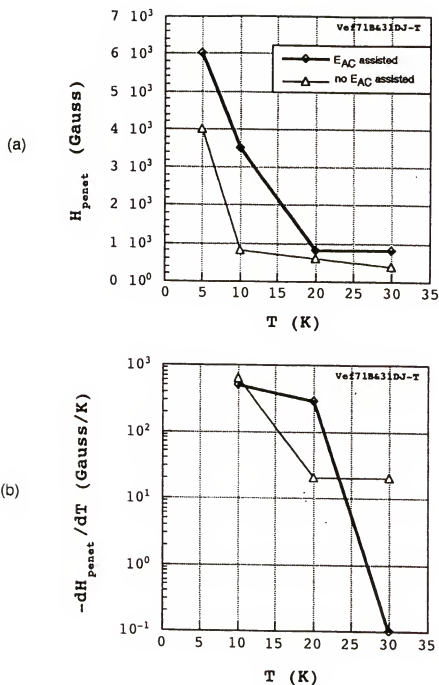


Figure 5-3 The temperature dependence of (a) penetration field, H_{penet} , and (b) the H_{penet} decreasing rates for Ag-sheathed BSCCO thick films prepared by the electrophoretic deposition with and without the AC-electric-field assisted c-axis texturing.

coupling between ab-plane grain boundaries parallel to the substrate surface is stronger. This also means higher thermal energy required for relaxing such intergranular coupling in AC-field-modified films. The H_{pene} ratio of these two kind of films is ranged from 1.5 to 2 in the same corresponding temperature range. These ratios are smaller than those (12.5~133) of J_c in the same corresponding temperature range.

Figure 5-3(b) displays the H_{pen} 's temperature derivative at different temperature. This temperature derivative dependency seems similar to magnetization's [Figure 5-2(c)], except the H_{pene} of AC-field-modified film reduces much less at higher temperature 30 K. Generally, the temperature derivative values (in the order of $10^3\sim 10^{-1}$) of H_{pene} are much larger than magnetization's (M_{pk} , in the order of $10^{-3}\sim 10^{-7}$). The average stability of J_c with AC-field-modification is about one order higher in magnitude than that without.

The experimental results are discussed in the following paragraphs.

The smaller temperature dependence of J_c for the films prepared by AC-field-modified electrophoretic deposition indicated that the thermally-activated flux creep of the Ag-sheathed BSCCO thick films is less due to stronger intergranular coupling. The pre-sintering BSCCO film microstructure by ACEPD results in much less microcracking and bending. Also, more c-axis textured colonies (neighboring plate-like grain cluster with c-axis alignment) can be formed in this ACEPD film. Therefore, with slightly higher c-axis

texture fraction, the sintered microstructure of fully processed film prepared by ACEPD possesses more c-axis colony connections with strong coupling for supercurrent paths. Such strong coupling resist the thermally-activated creep behavior as temperature rising, that is, higher thermal energy is needed to relax the coupling strength [Pust90, Palst88].

Between these two kinds of samples, this normalized J_c ratios of AC-field-modified film to conventional film at each temperature is one or two order larger in value than that of H_{pene} . That is AC-field modified film had about average two order larger in J_c , although merely 1.5 times larger in the intergranular coupling strength than those without AC-field modification. In highly c-axis textured films, H_{pene} is primarily related to the intergranular coupling of ab-plane grain boundary parallel to the substrate surface. Enhancing the critical current density, the AC-field-modified pre-sintering method can not only enhance the intergranular coupling of BSCCO grains due to more c-axis textured colony formation, but also improve intragranular component due to significant reduction in grain bending and microcracks.

From the temperature derivative analysis, the temperature stability for intergranular and intragranular components of the critical current density can be discerned. As temperature rising, the decreasing rate of $-(dH_{pen}/dT)$ was 10^6 times larger than M_{peak} 's. Such many order larger change in $-(dH_{pen}/dT)$ merely results in few $-(dM_{pk}/dT)$ variation. Because the intergranular component of M_{peak} variation is more

susceptible to the penetration field along ab-plane grain boundary than intragranular counterpart. Therefore, the intragranular component of M_{peak} is about 10^6 more stable with temperature variation. That is, the intragranular J_c could be 10^6 times more stable than intergranular J_c with respect to temperature variation.

5.2.2 Magnetic Field Dependence

The experimental Results are presented in the following:

The magnetic field dependence of current density of the Ag-sheathed BSCCO thick films with and without AC-electric-field modified electrophoretic deposition were shown in Figure 5-4 for different temperature. The applied magnetic fields in this plot are all corresponding to the H_{peak} . At the same temperature as 5 K, the current density for the film with AC-electric field-modification is one order higher in magnitude than that without. This J_c magnitude difference enlarges as the temperature increases. From 10 to 30 K, there are two order larger in magnitude for AC-modified film.

In Figure 5-5, the normalized current density curves with respect to 5 K @100 Gauss value revealed the clear view of the magnetic field dependence for both kind of films. For the curves measured below 20 K, the magnetic field dependence curves of both kind films can be overlapped to each other at corresponding temperature. At 30 K, the curves of both films only partially overlapped within the intermedium magnetic

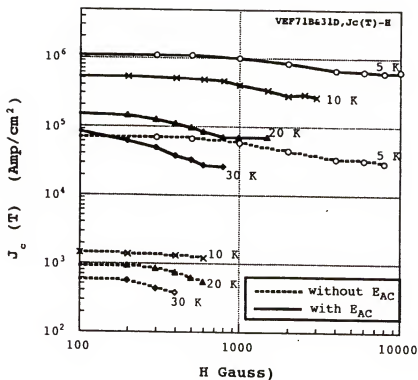


Figure 5-4 The magnetic field dependence curves of critical current density measured at different temperatures for the Ag-sheathed BSCCO thick films prepared by electrophoretic deposition with and without AC-electric-field assisted c-axis texturing.

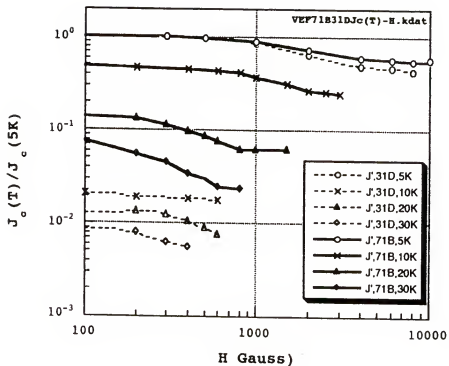


Figure 5-5 The normalized critical current density dependence on the applied magnetic field measured at different temperatures for the Ag-sheathed superconducting BSCCO tapes, prepared by electrophoretic depositions with (solid curves) and without (dashed curves) additional AC electric field assisted c-axis texturing.

field range for the film without AC-electric-field modification. These results revealed that the magnetic field dependencies of critical current density for both films were basically the same at low temperature (≤ 30 K).

The study showed that the AC-electric-field modified electrophoretic deposition can only improve the critical current density, and had less effect on improve the stability in magnetic field.

The experimental results are discussed in the following.

At different corresponding magnetic fields, the current density are one or two order higher in magnitude for the BSCCO film prepared by AC-electric-field modified electrophoretic deposition than by conventional EPD. This is due to the microstructure improvement using improved pre-sintering microstructure via MEPD. With less grain microcracking and bending in the AC-modified film, the intragranular component of J_c is higher due to better intragranular crystallinity. Considering plate-like grain bending, for example, 10° bending within 200~500 lattices results in 0.05° ~ 0.02° angular distortion per lattice. Such lattice distortion in plate-like grains should have similar effect as "diffusive" small angle grain boundary mismatch. This kind of grain boundary can also reduce J_c . Microcracks generated during pre-sintering processing can results in local lattice disorder after sintering. This kind of intragranular defect acts as grain boundary. In other words, the consolidated conventional EPD films having more such

intragranular defects can be treated as smaller grain sized film, leading to significant reduction in the intragranular component of the critical current density. It is noticed that the intragranular component of J_c is the majority, and the smaller grain sized films possess less such component.

The measured magnetic field dependence of current density for both kind of films are basically the same at low temperature (≤ 30 K). It is due to that the portion of intragranular crystallinity divided by the above defects are the basically same for BSCCO films prepared by conventional EPD. The magnetic field dependence of current density is primarily attributed to intragranular crystallinity.

In the next section, the processing parameter influence on superconductivity was discussed in detail, and correlated to the textured film microstructure.

5.3 Processing Parameter Influence on Superconductivity

It had also been investigated the relation between superconductivity and the major pre-sintering processing parameters such as particle size, consolidation pressure and temperature. To understand the microstructure controllability is the major objective of the processing parameter influence on the superconductivity of fully processed Ag-sheathed BSCCO films. The particle size is an important function of the pre-sintering microstructure control. Consolidation pressure and temperature change (i)

the film density, (ii) particle orientation, even (iii) the size (via microcracking) and (iv) the geometry (via microbending) of the consolidated plate-like BSCCO particles.

With two average BSCCO particle size, the pre-sintering microstructure influence on the critical current density and magnetic properties such as penetration field were investigated. Based on these experimental results, the variation of intergranular and intergranular components of J_c and their relationship to particle size were discussed.

It were systematically investigated that the consolidation pressure and temperature effects on magnetic property dependence of large particle sized films. Consolidation temperature effect on critical temperature transition ΔT_c was also investigated. This experiments was conducted to observe consolidation temperature influence on the inter-particulate binding and pre-sintering microstructure. The degrees of the inter-particulate binding and pre-sintering microstructure density impact the sintered texture and intergranular structure quality. A trade-off phenomena was discovered for these processing parameters for improving superconductivity of fully processed BSCCO tapes.

Sintering parameter effects on the superconductivity were also investigated to relate to the microstructure controllability for large particle size films in the study. The considered sintering processing parameters were the holding period of the sintering temperature and the cooling rate from this sintering stage to room temperature, while the

other sintering parameters were consistently maintained. The sintering temperature holding period can control the c-axis texturing enhancement and intergranular structure. The cooling rate is related to the composition of grains and the fine structure of grain boundary. The influences of sintering parameter on the shape of magnetic hysteresis loops and critical temperature behavior were investigated. These are related to the sintered intergranular crystallinity.

5.3.1 Particle Size Influence

With two different average particle sizes, Ag-sheathed BSCCO thick films were fabricated through the same processing described in Chapter II. Conventional electrophoretic deposition was used to form BSCCO films. The sintered specimens of the same dimensions then were characterized using SQUID magnetometry. Induced magnetization was plotted as a function of the applied magnetic field. The maximum applied magnetic field was 5 Tesla in two opposite orientations normal to tape specimen surface. The measurement was conducted at 5 K. The particle aspect ratio is the ratio of the dimension along ab-plane to that perpendicular to ab-plane of a grain, i.e., length/thickness ratio,

The experimental results are presented in the following paragraphs.

The magnetization hysteresis loops of BSCCO films with two different pre-sintering particle sizes, 0.98 μm and 0.36 μm shown in Figure 5-6. A summary experimental result data is

shown in Table 5-1. For the large particle sized film, the maximum magnetization 87.2 emu/cm^3 and -86.1 emu/cm^3 appear corresponding to the applied magnetic fields 12.2 and -2.2 Gauss, respectively. For the small particle sized film, the maximum magnetization 35.3 emu/cm^3 and -34.6 emu/cm^3 were measured corresponding to the applied magnetic fields 11.5 and -11 Gauss, respectively. The average maximum magnetization of large particle size film is 2.5 times that of small particle size. This hysteresis loop shapes indicated that both kinds of tapes are superconductive. ΔM , the difference between the positive value and negative value of maximum magnetization is substituted into Equation (2-2) for estimating the critical current density J_c . The J_c 's were calculated as $1.7143 \times 10^5 \text{ Ampere/cm}^2$ for the large particle size films, and $6.4172 \times 10^4 \text{ Ampere/cm}^2$ for the small particle size films. Similar to the maximum magnetization, J_c of the large particle size film is 2.67 times that of the small particle size.

In the hysteresis loops, the magnetic fields H_{c2} were ± 4 Tesla for the large particle size film, as those for the small particle size film were ± 2 Tesla which were one half of the former's. This results indicated that the magnetic field level for stable superconductivity is higher in the larger particle size films. The average H_{pk} magnitude is 7.2 Gauss for the large particle size film, and 11.25 Gauss for the small particle size film.

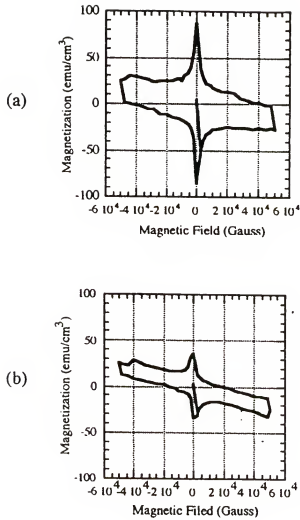


Figure 5-6 The magnetic hysteresis loops of peeled Ag/BSCCO/Ag tapes fabricated using BSCCO powders with average particle size of (a) 0.98 μm and (b) 0.36 μm .

Table 5-1. The superconductivity of peeled Ag/BSCCO/Ag tapes fabricated using BSCCO powder with different average aspect ratios (particle sizes).

Charact.\particle size	0.36 μm	0.98 μm
$+M_{\text{max}}/-M_{\text{max}}(\text{emu}/\text{cm}^3)$	35.3/-34.6	87.2/-86.1
$+H_{\text{peak}}/-H_{\text{peak}}(\text{Gauss})(H_{C1})$	11.5 / -11	12.2/-2.2
$+M_{\text{pene}}/-M_{\text{pene}}(\text{emu}/\text{cm}^3)$	-16.6/16.2	-24.8/24.4
$H_{+M_{\text{pene}}}/H_{-M_{\text{pene}}}(\text{Gauss})$	12000/-10035	20050/-20060
$H_{C2}(M=0)(\text{Gauss})$	20000	40000
$\Delta M_{\text{max}}(\text{emu}/\text{cm}^3)$	69.9	173.3
$J_c(\text{Amper}/\text{cm}^2)$	6.4172×10^4	1.7143×10^5
$\Sigma I_{(00L)}/\Sigma I_{(HKL)}$	0.908	0.9824
C_x	3.6642	3.9645
Particle Aspect Ratio	3.6	9.8
Film dimensions (cm^3)	$0.249 \times 0.441 \times 5 \times 10^{-4}$	$0.275 \times 0.442 \times 6 \times 10^{-4}$

From the above experimental results, it was found the pre-sintering BSCCO particle size had an impact on the resulted superconductivity of the Ag-sheathed sintered thick film. As the pre-sintering plate-like BSCCO particles in the Ag-sheathed film is 2.72 times larger in size (i.e., particle aspect ratio), the film had 2.67 times larger in J_c , and had 2.0 times higher in the H_{pene} level, although with the same sample configuration. This fact displays that larger particle size films have better ab-plane boundary coupling. The H_{peak} of the large particle size film is only 64% of that of the small particle size film. This implies that the large particle size films possess stronger link in supercurrent path.

It is noticed that the J_c values characterized by SQUID magnetometry is higher than those by four-probe method, due to two-dimensional electric current generation mechanism. The polycrystalline film values are lower than those of epitaxial thin films or single crystalline specimens, owing to grain boundaries.

The x-ray diffraction patterns for both peeled films are shown in Figure 4-14. The XRD pattern in Figure 4-14(b) reveals larger fraction of randomly-oriented BSCCO particles existing in small particle size films, due to the fraction of average background noise from small particle films is higher than that of large particle size films. Some ultrafine particles may still exist in the sintered films. Since these ultrafine grains are randomly-oriented, the background noise

intensity ratio of small particle size film is higher. The ratio of c-axis texture fraction of the large particle size film to the small particle size film is 1.082.

Although, the critical current density of BSCCO tapes prepared using smaller size BSCCO powder is less than that using large size BSCCO powder, the former are much superior than the latter in mechanical properties which are relevant to practical applications of tapes.

The experimental results are discussed in the following.

The fully processed large average particle size films had the higher the critical current density. The larger particle aspect ratio is related to the enhancement the intragranular current density. It was found that 2.67 times higher J_c measured in the large particle size films than in small particle size films, although similar in the dimensions and c-axis texture fraction of both films, and the same processing. However, most of particles have the similar thickness. In large particle size films, the number density of grain boundary is smaller as 1.0204×10^4 (boundary/cm). With similar c-axis texture fraction, the supercurrent encounters less grain boundaries for the same unit current path length. Small particle size film has 2.7778×10^4 boundary/cm. Thus, higher critical current density can pass through the large particle size films. The weak coupling in grain boundaries was well-known limiting the critical current density. The intragranular J_c is larger than intergranular

counterpart due to the crystallinity difference [Jagan92] and the crystallographic lattice symmetry variation [Ayy95]. Grain boundaries have poor superconducting coupling [Dim90] and dislocation networks [Babco90] than the grain bulk.

The higher H_{pene} for large particle size films implies that stronger link along ab-plane grain boundaries or c-axis textured colony boundaries parallel to substrate surface. As the c-axis of a BSCCO crystal parallel to the applied magnetic field orientation, the maximum magnetization is measured in this crystallographic orientation, due to the extremely anisotropy of BSCCO crystal [Web77, Ginz88]. In small size particle films, the small longest particle dimension is the limit to magnetic field penetration length, i.e., to H_{pene} .

H_{pk} is related to the BSCCO film crystallinity where is supercurrent follows. As the superconducting films contain lower quality portions (e.g., grain boundary, etc.), or higher density of same low quality portions for inducing supercurrent, the applied magnetic field required to induce maximum magnetization increases.

$$H_{pk} \propto f(\sum a N_{gb,i} + \sum b N_{ds1,j} + \sum c N_{l1tc,k} + \dots) \quad (5-1)$$

which $N_{gb,i}$, $N_{ds1,j}$ and $N_{l1tc,k}$ are the number density per unit supercurrent path length of the given grain boundary, dislocation, and lattice, respectively; a, b and c are parameters for these low crystallinity portions,

respectively. For large particle size films, the lower H_{peak} stands for better the supercurrent path link, i.e. stronger intergranular coupling. In single crystal and epitaxial thin film form, the H_{peak} is very close to zero and the hysteresis loop peaks are symmetrical to vertical axis (magnetization axis) due to no grain boundary. Since the c-axis texture fraction was major contributed by c-axis colonies. Within such colony microstructure, the intergranular coupling is stronger than those among the singly distributed c-axis-textured grains [Goy94]. Bi-axial textured ab-plane grain boundaries within such colonies have even much stronger coupling. In small particle size films, the c-axis texture fraction were primarily contributed by singly distributed grains with their c-axis perpendicular to substrate surface.

5.3.2 Uni-axial Pressure Effect

The consolidation pressure influence on the magnetic properties was studied for fully processed BSCCO films at room temperature. Magnetization and applied magnetic fields were measured from the magnetization hysteresis loops. Based on the experimental results in the particle size effect study section, the large particle size $0.98 \mu\text{m}$ was used in this sets of experiments.

The experimental results of the sintered Ag-sheathed BSCCO films prepared by cold consolidated at different pressure is presented in the next section.

The experimental results are presented in the following.

Corresponding to the peak magnetization values, the peak magnetic fields were measured and plotted in Figure 5-7(a) for the BSCCO films prepared at different consolidation pressures. The constant H_{peak} revealed that the qualities of both intergranular and intragranular crystallinity were not varied by the room temperature consolidation pressure. In contrast, the penetration field was found decreased with increasing consolidation pressure shown in Figure 5-7(a). As the pressure increases up to 4 times, the H_{pene} decreased merely down to 80%. However, the sintered films' penetration field dependency on the uni-axial pressure for consolidating pre-sintering films is not linear. These results displayed either the increased number density of grain boundary, or the intergranular coupling of ab-plane grain boundary parallel to the substrate surface. The former reason is more likely the majority in the case.

The peak magnetization M_{peak} , i.e., J_c , increases up to 3.5 times as the consolidation pressure increases up to 4 times. The M_{peak} dependence on uni-axial pressure is not linear, either. However, the M_{peak} values (11.5~39 emu/cm³) are in the same low order of magnitude, indicating the mechanical force alone can not significantly improve the pre-sintering microstructure in terms of inter-particulate binding and c-axis texturing enhancement. The M_{pen} was measured to show similar tendency of magnetic property as M_{pk} . The measured low magnetization (≈ 12 emu/cm³)

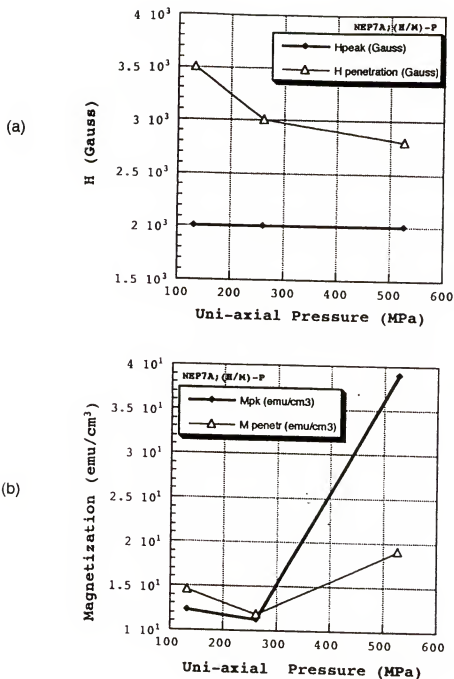


Figure 5-7 The room-temperature consolidation pressure effect on the superconductivity of the simultaneously sintered Ag-sheathed BSCCO thick films: (a)magnetic fields and (b)magnetizations corresponding to the peak and penetration values in the magnetization hysteresis loops.

corresponding to the intermedium pressure (264 MPa) are close to those (M_{peak} 12.3 emu/cm³ and M_{pen} 14.6 emu/cm³) to the lowest pressure (132 MPa). There may be error in the measurement of specimen dimensions.

The experimental results are discussed in the following.

H_{pen} decreasing with pressure is due to the increase in the number density of grain boundary. The higher the consolidation pressure, the more particles can be broken into smaller sizes at room temperature. At such temperature, plate-like BSCCO particles are relatively fragile to break. Also, the constant H_{peak} indicated that the intergranular coupling strength did not vary with the pressure, meaning no significant change in intergranular crystallinity in the films prepared by increasing pressure. Kept in mind, the H_{pene} primarily stands for the quality or quantity of intergranular coupling of ab-plane grain boundary parallel to the substrate surface. Thus, the reduction of H_{pene} implies that either the number density of grain boundary increases or coupling strength decreases. since the consolidation occurred at room temperature and same initial particle size, the coupling strength should not be changed so much. Therefore, the higher number density of grain boundary is the logical origin resulted from higher pressure breaking particles into smaller size.

Larger J_c (or M_{peak}) with increasing consolidation pressure is primarily resulted from increased c-axis texture fraction for size-reduced particles in the BSCCO films.

Supposedly for the same large particle size films, the higher the C_x , the higher the J_c is measured. But low magnitude of M_{peak} supports the idea that the pre-sintering particle reduced due to higher pressure breaking particles into smaller sizes.

5.3.3 Consolidation Temperature Effect

Thermal energy provided during consolidation can improve the inter-particulate binding and microstructure density in pre-sintering Ag-sheathed BSCCO thick films. The sintered films using such pre-sintering microstructure exhibited better superconductivity than cold consolidation. The large particle size $0.98\ \mu\text{m}$ was used in this sets of experiments. 500 MPa pressure was applied during heating up and temperature holding period one hour, as well as at room temperature consolidation. So all films in this experiment had the similar microstructure as that in the previous section, which average particle size reduces more via breaking plate-like particles by the highest pressure at room temperature. If lower consolidation pressure was exerted in this set of experiment, the superconductivity improvement with heating consolidation should be more pronounced.

The experimental results are presented in the following paragraphs.

The H_{pk} decreased from 2000 Gauss to 900 Gauss, as the consolidation temperature increased from 25°C up to 400°C

shown in Figure 5-8 (a), indicating that the intragranular crystallinity of the BSCCO films can be improved with higher consolidation temperature. The penetration field H_{pene} increased up by near one order higher in magnitude (2900 to 25000 Gauss), as the consolidation temperature raised up from 25°C up to 400°C. This phenomena implied that there had been improvement in intergranular crystallinity of ab-plane grain boundary parallel to the substrate.

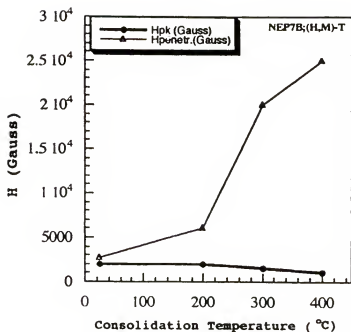
With improved intergranular and intragranular microstructure, the peak magnetization (thus critical current density) increased (22 to 49.4 emu/cm³) up to about 4 times higher in the films prepared by 16 times higher consolidation temperature (25° to 400°C). Although the J_c dependence on consolidation temperature is not linear with steeper magnetization rising in the range of 200°~300°C. The M_{pen} also has similar dependence and close values as M_{pk} .

The critical temperature transition ΔT_c decreased with higher consolidation temperature was measured shown in Figure 5-9. This results further confirmed the better intergranular crystallinity in the films prepared at higher consolidation temperature.

The experimental results are discussed in the following.

The results of H_{peak} decreasing with increasing consolidation temperature indicate that less magnetic field is needed to induced higher critical current density, due to the intragranular crystallinity was improved using the

(a)



(b)

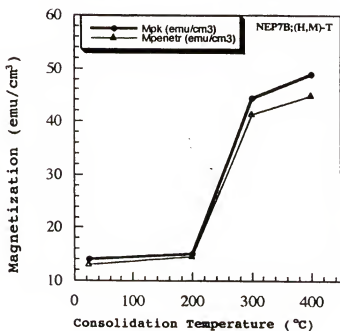


Figure 5-8 The thermomechanical consolidation temperature effects on the superconductivity of Ag-sheathed BSCCO thick films, pressed at the 500 MPa for 1 hour and simultaneously sintered: (a) magnetic field & (b) magnetization corresponding to the peak and penetration values in magnetization hysteresis loops.

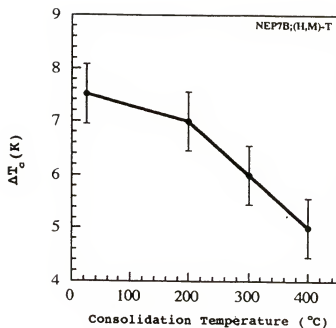


Figure 5-9 The effect of thermomechanical consolidation temperature on the critical temperature transition ΔT_c for the samples prepared at the same pressure, holding time, and simultaneously sintering.

improved pre-sintering microstructure prepared at higher consolidation temperature. Started with higher pre-sintering film density, the better the film crystallinity can be synthesized. The low reduction in H_{pene} with consolidation temperature is risen from the major crystallinity improvement contributed by the intergranular component. The intragranular component contribution is limited by the reduced average particle size of the starting microstructure via high pressure before heating up. Smaller particle size approaching to flux vortex lattice parameter can weaken the intragranular flux pinning force density as discussed in the section of Particle Size Effect. The pronounced increase in H_{pene} with consolidation temperature revealed that significant improvement in intergranular coupling, due to better intergranular crystallinity prepared by heated consolidation. Consolidated at high pressure, the interparticulate contact area and binding of BSCCO films can be enhanced by thermal energy. As mentioned in Chapter V, larger interparticulate contact area and tighter bound interparticulate boundary can lead to (i) further increase sintered film density by reduced micro-pores, and (ii) improve crystallinity near grain boundary of the sintered films. This intergranular coupling enhancement is not reduced by the smaller initial particle size.

Risen from the improved pre-sintering microstructure by higher consolidation temperature, the above improved intergranular crystallinity, thus, resulted in higher J_c (or

M_{peak}). The small difference between M_{peak} and M_{pen} is due to the limited contribution of intragranular flux pinning enhancement. This limitation is caused by the high-pressure-reduced average particle size in the initial film before consolidation heating beginning. That is, even with higher number density of grain boundary, the thermal energy still can improve the inter-particulate microstructure of pre-sintering films. These discussions can be also served as the reasons for decreasing ΔT_c with increasing consolidation temperature.

5.3.4 Sintering Parameter Effect on Superconductivity

The last set of sintering experiment was conducted to investigated the sintering parameter effect on magnetically-characterized superconductivity of Ag-sheathed BSCCO films for optimizing the critical temperature T_c . This grain boundary microstructure improvement can be controlled with the sintering parameters. They are the holding period at the highest sintering temperature T_{s1} (stage 1) and the cooling rate R_1 from the T_{s1} (870°C) to T_{s2} (840°C) shown in Figure 2-6. The curves of measured AC magnetic susceptibility as a function of temperature were used to determine the T_c and ΔT_c and was related to the grain boundary's structure quality of the differently sintered BSCCO films.

The sintering parameters was set referring to the results of Differential Temperature Analysis shown in Figure 4-5 and literature study [Khar90,Namg89]. The first cooling

rate R_1 is 2°C/hour or $10^\circ 2^\circ \text{C/hour}$, while the holding period t_1 at the first stage T_{s1} is 0.1 hour or 0.5 hour. R_2 is done by quenching the specimen in methanol from 840°C down to room temperature in 5 second. The first sub-set sintering experiment was designed to compare the effect of t_1 on magnetically characterized superconductivity for low constant cooling rate $R_1=10^\circ \text{C/hour}$, and the second sub-set experiment was for $R_1=2^\circ \text{C/hour}$. The ambience is open atmosphere. All four specimens were cut from the same Ag-sheathed BSCCO thick film.

The upper T_c can be determined from the AC susceptibility curve where the temperature corresponding to the paramagnetic (normal conductivity) to diamagnetic phase (superconductivity) transformation, that is, the real part of AC susceptibility χ' starts to change from zero to negative value. Below $T_{c,upper}$ or T_{c1} , the temperature corresponding to the second curvature reversal is $T_{c,lower}$ or T_{c2} .

The experimental results are presented and discussed in the following.

Holding period at the sintering temperature T_{s1} was found to elevate T_{c1} and to reduced the critical temperature transition ΔT_c . Observed from Figure 5-10 (a) & (b) for high cooling rate $R_1=10^\circ \text{C/hour}$, the film sintered by longer t_1 (0.5 hour) at T_{s1} (870°C) had higher T_{c1} 88 K, T_{c2} 82 K and smaller ΔT_c of 6 K, indicating better crystallinity in grain and along boundaries, while the film with shorter t_1 (0.1 hour) had T_{c1} 86 K, T_{c2} 75 K and ΔT_c of 11 K. Kept in mind

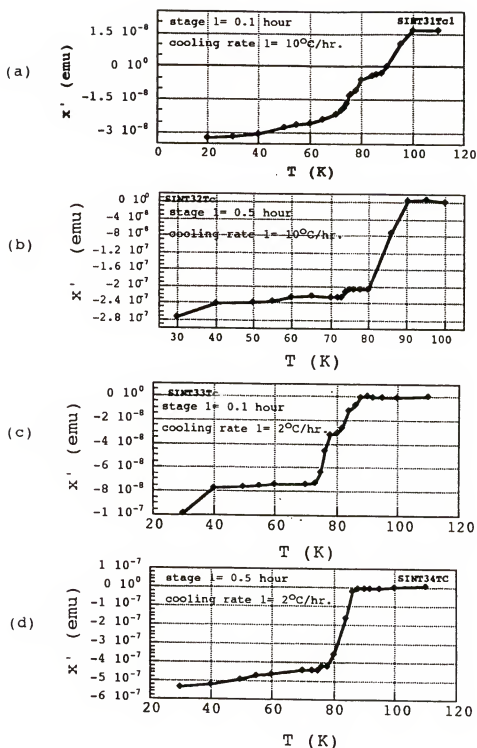


Figure 5-10 The AC magnetic susceptibility x' as a function of temperature of Ag-sheathed BSCCO-2212 samples (cut from the same tape) prepared by different two-stage sintering programs: (a) SINT31, (b) SINT32, (c) SINT33 and (d) SINT34.

that all sintering temperatures were the same. These experimental results revealed the feasibility of crystallinity improvement can be achieved merely via the short sintering holding period at high temperature stage. Longer sintering temperature holding period provides the more time required for synthesizing superconducting phase near grain boundary. With extended t_1 , more particles can be c-axis textured as softening, and more grain boundary could occur partial melting. However, if t_1 is too long (couple of hours), the composition of BSCCO may partially and locally deviated from superconducting phases.

Slow cooling rate was found to have slight enhancement effect on elevating T_{c1} and on reducing ΔT_c by longer T_{s1} holding period. From Figure 5-10 (c) & (d) for lower cooling rate R_1 2 °C/hour, the sintered film for longer t_1 0.5 hour had T_{c1} 88 K, T_{c2} 83 K and ΔT_c of 5 K, while those for shorter t_1 0.1 hour are 86 K, 75 K and 11 K, respectively. From the inter-comparison for the specimen processed with the same short t_1 , the χ' values for slow R_1 were twice more negative than those obtained from faster R_1 . It seems the superconductivity of the specimens with longer holding t_1 were more sensitive to the cooling rate R_1 between the two sintering stages, due to more grain boundary partially molten. Slower cooling rate R_1 enables the emulated intergranular crystal growth as intragranular crystal structure, via slow outward movement of the smooth grain/molten interface [Port81].

Indicated by higher H_{pene} , longer T_{s1} holding period t_1 enhanced the intergranular coupling at R_1 10 °C/hour. Figure 5-11 shows part of the magnetization hysteresis loops for these specimens sintered at different t_1 and R_1 . Sintered at R_1 10 °C/hour, the H_{pene} 8000 Gauss with longer t_1 0.5 hour was higher than 6000 Gauss with 0.1 hour; but the same as that with 0.1 hour at slower R_1 2°C/hour. The specimen of higher H_{pene} has enhanced intergranular coupling. However, the highest two M_{peak} , i.e., J_C , can only obtained with long t_1 0.5 hour. The specimen SINT34 had the highest J_C with long t_1 0.5 hour and slow cooling rate R_1 2 °C/hour. This is also corresponding to (i)the highest upper critical temperature T_{C1} , (ii)the smallest critical temperature transition ΔT_C 5 K, and (iii)the highest H_{pene} 9000 Gauss, among these four specimens for Sintering Parameter Effect experiment. Due to better resultant intergranular crystallinity, the smaller ΔT_C is contributed by the improved AC susceptibility response of intergranular coupling to the applied AC magnetic field 0.1 Gauss, at 100 Hz.

Thus, this sintering condition set was used in the previous section for investigating the effect of the improved pre-sintering microstructure by AC-electric-field-modified electrophoretic deposition. The highest H_{pene} is related to the strongest coupling of ab-plane grain boundary parallel to the substrate surface. Sintered at long holding period and/or slow cooling rate, this crystal growth emulates the intergranular structure as the superconducting grain's

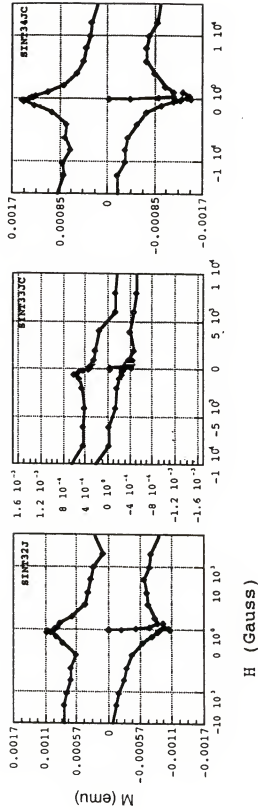


Figure 5-11 The magnetization hysteresis loops of Ag-sheathed BiSrCaCuO thick films with the same dimensions prepared by different sintering programs: (a) SINT32, (b) SINT33, and (c) SINT34.

crystallinity, via reducing the intergrowth, local miscellaneously-oriented grain boundary structure, micro-pores and incoherence.

5.4 Summary

The superconductivity characterizations of the BSCCO films in this chapter proved the feasibility of improving superconductivity with systematic pre-sintering processing. Consistent to the structural characterizations, the superconductivity characterizations further confirmed the improvement of the Ag-sheathed BSCCO thick films via improving the pre-sintering microstructure. Prepared by AC-electric-field-modified electrophoretic deposition, the BSCCO films possessed superior superconductivity stability with respect to temperature and magnetic field, due to enhanced c-axis texturing in the pre-sintering microstructure with less microcracking and bending. This kind of pre-sintering microstructure resulted in better sintered film microstructure such as better intragranular and intergranular structures and c-axis texturing enhancement.

Pre-sintering processing parameter effects on the superconductivity had been systematically investigated, and related to BSCCO film microstructure. Particle size was studied as a pre-sintering microstructure control base. The large particle size (0.98 μm) films had higher critical current density, higher penetration field, and larger range

of mixture states ($H_{C1} \sim H_{C2}$) than smaller particle size films, due to larger grain size (much larger than vortex lattice constant), better intragranular crystallinity, and stronger intergranular coupling of ab-plane grain boundary parallel to the substrate surface.

Consolidation processing parameters was also found having the controllability on the pre-sintering microstructure quality. Cold pressing at higher pressure resulted in worse quality in terms of more particle breaking into smaller sizes and more particle microcracking within Ag-sheathed BSCCO thick films. After sintering, the cold pressed films showed lower H_{pene} with higher consolidation pressure and constant H_{pk} , owing to lower intergranular coupling with increasing consolidation pressure, and no improvement in intragranular superconductivity, respectively. Heating during consolidation at high pressure was found capable of improving the above drawbacks. Higher consolidation temperature can enhance the inter-particulate binding, further reduce micro-pore volume fraction, and relax the mechanical-work-induced strains. The higher the consolidation temperature, the (up to four times) higher the J_c was, the lower H_{peak} was, and the (up to one order) higher H_{pene} measured was found in the sintered films, as well as lower the critical temperature transition ΔT_c , since the more enhanced c-axis texturing, the better the intragranular crystallinity, and stronger intergranular coupling for supercurrent transport, respectively. These superconductivity control by

consolidation processing parameters was found a kind of trade-off between pressure and temperature.

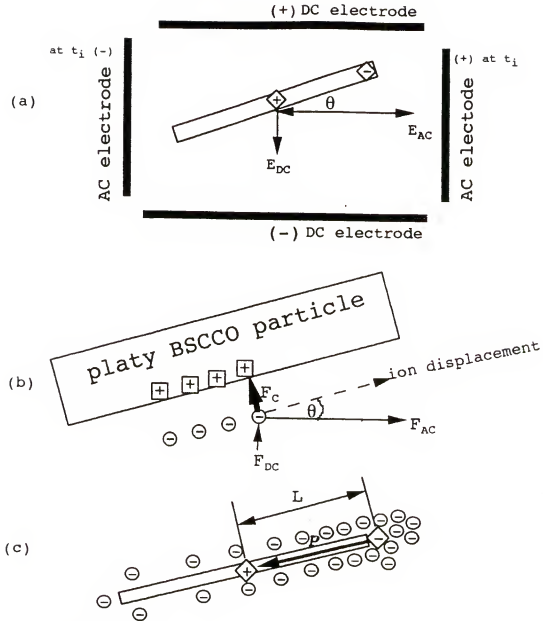
Sintering parameter effect study concluded that slower cooling rate from the highest sintering temperature T_{s1} and longer holding period at T_{s1} gave the best superconductivity among the investigated conditions: smaller higher T_{c1} , ΔT_c , H_{pne} and J_c . Control of intergranular crystal growth and c-axis texturing enhancement by these sintering parameters was confirmed feasible.

CHAPTER VI

COMPUTER SIMULATION MODEL FOR ANGULAR MOTION BEHAVIOR OF PLATE-LIKE PARTICLE IN ACEPD

6.1 Introduction

The angular motion behavior of plate-like BSCCO particles is modeled as a system based on the physical model of the interaction between the applied electric fields and the particle-geometry-preference-induced electric dipole. The physical modeling for plate-like BSCCO particle in the additional-AC-field modified electrophoretic deposition comes out the angular vibration behavior of plate-like BSCCO particles derived in the following paragraph. The purpose of this derivation is to elucidate the non-linear behavior of BSCCO particle major face orientation in the dispersion under the influence of AC electric field. First, the net effective dipole model is postulated. To simplify, a plate-like BSCCO particle has the longest dimension of its major face parallel to **a**-axis of crystallographic structure, and orients the longest dimension to the applied AC electric field orientation at an angle θ shown in Figure 6-1(a) at the beginning of electrophoretic deposition. Just as the discussions about the forces affecting particle orientation, the electric force has many order higher in magnitude than fluid dynamic force and any



F_{AC} = AC electric force (at t_i)

F_{DC} = DC electric force

F_C = Coulomb's force by particle surface charge

P = particle-geometry-preference-induced electric dipole moment

\oplus = BSCCO particle surface charge

$\diamond+$ $\diamond-$ = charge center of cations and anions, respectively

Figure 6-1 The schematic showing particle-geometry-preference-induced electric dipole moment formation in additional AC electric field modified electrophoretic deposition: (a) particle-electrode configuration, (b) electric forces cooperation, and (c) electric dipole formation.

other physical forces. Therefore, the Brownian motion effect and unbalanced fluid dynamic drag force effect can be neglected in this physical model. As AC electric field of frequency ω applied, a net effective electric dipole moment parallel to the BSCCO particle major face can be induced and expected to be initially flipping up and down its major face (i.e., ab-plane) along a given axis at its own unstable frequencies. Eventually, by the applied AC field, such a electric dipole associated with BSCCO particle can be switched along an axis approaching AC field orientation, and the angular vibration amplitude of the particle can be attenuating by surrounding medium damping within short time. Figure 6-1(b) shows the electric forces exerting on the anion of electric double layer. Then the cooperation of AC field, DC field and particle surface charge attraction results in a net electric force. This is net electric force can displace the adsorbed anions parallel to the particle major face. Such an extension of the electric double layer is virtually two-dimensional parallel particle major face instead of three-dimensional spherical distortion. Thus, the induced electric dipole moment [shown in Figure 6-1(c)] is associated with the long dimension of particle major face, and becomes greater as the angle θ approaches to zero or 90° . The positive charge center of the induced electric dipole moment is coincident to that of particle surface charge, and the negative charge center is at the charge center of elongated anion layer which is assumed to be soon saturated to maximum value as total

effective field larger than 30 v/cm. The induced electric dipole moments have two components, P_{DC} and P_{AC} , expressed as the below equations:

$$P_{DC} = -\chi E_{DC} \cos(\pi/2 - \theta) = -\chi E_{DC} \sin(\theta) \quad (6-1)$$

$$P_{AC} = -\chi E_{AC} \sin(\theta) = -\chi E_0 \cos(\omega t) \sin(\theta) \quad (6-2)$$

which χ is the polarizability of adsorbed anion layer, t is time, and E_{AC} is AC electric field as $E_0 \cos(\omega t)$, E_0 is the maximum amplitude of AC field strength (v/cm). The interaction between applied electric field and the dipole moments results in the an electric-force-related torque acting on this BSCCO plate-like particle as a function of θ and time, $f(\theta, t)$. The torque is defined as $\tau = P \times E \sin(\theta)$.

$$\begin{aligned} f(\theta, t) &= -P_{AC} \times E_{AC} \sin(\theta) - P_{DC} \times E_{DC} \sin(\pi/2 - \theta) \\ &= -[\chi E_0 \cos(\omega t) \cos(\theta)] \times [E_0 \cos(\omega t) \sin(\theta)] - [\chi E_{DC} \sin(\theta)] \times \\ &\quad [E_{DC} \sin(\pi/2 - \theta)] \\ &= -\chi E_0^2 \cos^2(\omega t) \cos(\theta) \sin(\theta) - \chi E_{DC}^2 \cos(\theta) \sin(\theta) \end{aligned} \quad (6-3)$$

The polarization effects by AC and by DC electric field should be the same for low AC frequency ($\ll 10^6$ Hz). At low original angle θ , AC electric field dominantly induces the electric dipole over DC's. At large original θ , the electric dipole is induced primarily by DC electric field. Due to limited by particle dimension, the induced polarization of the anion layer is restricted within a small range even with decreasing angle θ . The induced electric dipole moment

hence can be treated as independent of θ by neglecting the small variation with decreasing θ . Therefore, the induced dipole value is approximately a fixed value. Then, the equation can be simplified as

$$f(\theta, t) = -\chi E_o \cos^2(\omega t) \sin(\theta) - \chi E_{DC} \cos(\theta) \quad (6-4)$$

The other torque on the particle exerted by the damping force from surrounding medium can be analogous to linear motion case:

$$\begin{aligned} \tau_{\text{damping}} &= -(\text{viscosity coefficient})(\text{angular velocity}) \\ &= -\mu(d\theta/dt) \end{aligned} \quad (6-5)$$

Considering the whole BSCCO particle as a rotational body, the third torque can be expressed as the product of plate-like body inertia and angular acceleration:

$$\tau_{\text{rotate.}} = I(d^2\theta/dt^2) \quad (6-6)$$

The overall torque equation hence can be expressed by integrating equations (6-4), (6-5) and (6-6) as

$$\begin{aligned} I(d^2\theta/dt^2) &= -\mu(d\theta/dt) + \chi E_o \cos^2(\omega t) \sin(\theta) - \chi E_{DC} \cos(\theta) \\ &= -\mu(d\theta/dt) + f(\theta, t) \end{aligned} \quad (6-7)$$

Both sides of equal sign divided by inertia I , the equation (6-7) becomes

$$d^2\theta/dt^2 = -\mu(d\theta/dt) / I + f(\theta, t) / I \quad (6-8)$$

Solving this nonlinear second order differential equation, the angular vibration motion behavior of plate-like BSCCO particle can be modeled by numerical analysis method using computer capability. A C++ program was then developed to computationally solve this complicated equation (referred to Appendix). Remarks for computing are all list in the C++ program, the iteration approaching algorithm was employed for numerical solution programming. The experimental parameters such as DC electric field strength, AC electric field strength and frequency, initial particle orientation with respect to AC electric field orientation, can be input to simulate the angular vibration motion behavior of plate-like BSCCO particle for different electrophoretic deposition conditions.

6.2 Plate-like Particle Alignment By DC Electric Field

The computer simulation result of DC electric field 40 v/cm on angular vibration motion behavior plate-like BSCCO particle major face in dispersion solution using conventional electrophoretic deposition is shown in Figure 6-2. The equation used for the physical model is the same as Equation (6-8) simply by setting E_0 equal to zero. The zero E_0

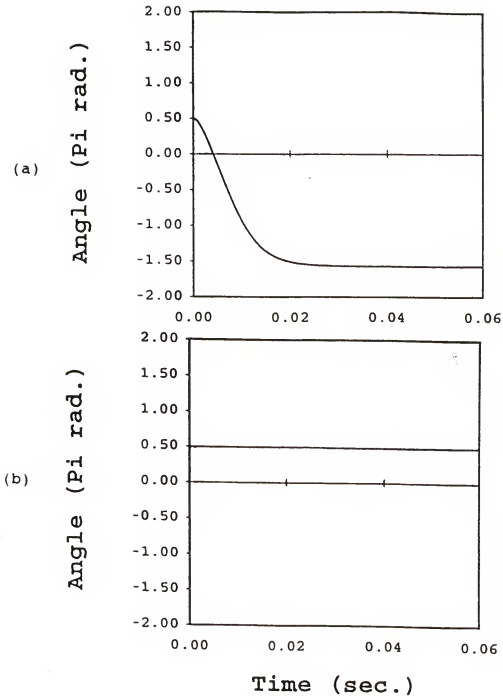


Figure 6-2 The plot of computer numerical simulation for platy BSCCO particle angular motion behavior as a function of time in electrophoretic deposition at $E_{DC} = 40$ v/cm: (a) slow depolarization and (b) quick depolarization case as DC electrode polarity instantly reversed.

eliminates the contribution of AC electric field to the particle angular motion behavior. The horizontal axis of the simulated plot is time, and the vertical axis represents the angle between particle major face and orientation parallel to the substrate surface (this orientation is parallel to AC electric field in the case of additional-AC-field modified electrophoretic deposition) in unit π **radian** (i.e., 90°). With original angle $\pi/2$, the electric dipole associated with BSCCO particle major face rotates 2π into the opposite direction to the original direction, and then fixes at the direction still perpendicular to substrate surface. The smooth curve indicates no angular vibration of BSCCO particle caused by DC electric field, due to the constant E_{DC} (non-restoring force) can not induce any switching behavior of electric dipole. Within short time (about 0.02 second), the particle major face orientation rotates to a fixed angle -1.5π which means perpendicular to substrate surface. Thus, the deposited BSCCO film should have pure a-axis texturing enhancement! This computer simulation result is consistent to the experimental results in section 3-2. However, since the actual particle texturing behavior in electrophoretic deposition is not only determined by the incident particle orientation in medium, but also by the interaction between substrate surface morphology and the contacting particle,...etc. The real particle a-axis texture is not as ideal as the simulation results for DC electric field enhanced a-axis texturing. The particles with different original angles have the same

dependence on time, except smaller angular vibration amplitudes than the simulation's).

6.3 Angular Motion Behavior Of Plate-like Particle With Additional AC Electric Field Parallel To Substrate Surface

The angular vibration motion behavior of the plate-like particle is modeled considering the cases with an additional AC electric field parallel to substrate surface, i.e., simultaneously perpendicular to DC electric field direction, using Equation (6-8) in the computer simulation. In the previous section of this chapter, the physical model derivation was conducted into a nonlinear second order differential equation of one-dimensional form (i.e., perpendicular to substrate surface, Figure 6-1). In the other dimensions, e.g., the parallel dimension to substrate surface, hardly contribute to the c-axis texturing enhancement. The close-form solution of the nonlinear differential equation would be so complicated that the property of processing parameter effect can not be easily and intuitively figure out. Numerical solutions were thereby employed used to plot the solution data. Similar reasons were also applied for the DC field case in the previous computer simulation section. The electrophoretic deposition parameters were set for different simulations to elucidate the effects of (i) AC electric field strength, (ii) AC field frequency, (iii) DC electric field strength, and (iv) the original orientation of particle major face. furthermore, the

simulation results can compare with those of actual experimental results. The possible simulation results were schematically drawn to demonstrate that relation between the simulated data curves and the AC-electric-field-modified electrophoretic deposition configuration in the Figure 6-3. In this figure, plate-like BSCCO particles were only shown their length-thickness view, since the particle major faces are parallel to the line of sight into the paper. In the mathematics equation (6-8), the coefficients were reasonably estimated from fundamental calculation. It is noticed if the viscosity is several order smaller than 10^{-6} , then the "number of total step to take" in simulation should be reduced accordingly. Otherwise, the resulted data become unreasonable to explain.

6.3.1 AC Electric Field Strength Effect On Plate-like Particle Orientation Control

Figure 6-4 illustrates the effect of additional AC electric field strength on plate-like particle orientation behavior. Low DC electric field 40 v/cm, and 200 Hz AC frequency at different AC electric field strengths: 40, 100, 200, 300 and 500 v/cm were used to conduct the computer simulation. The most concerned portion of each curve is the attenuated stage with stable axis orientation, frequency and amplitude of particle's angular vibration motion. Since the angular vibration motion behavior of plate-like particle is nonlinear, there is no simple linear dependency of

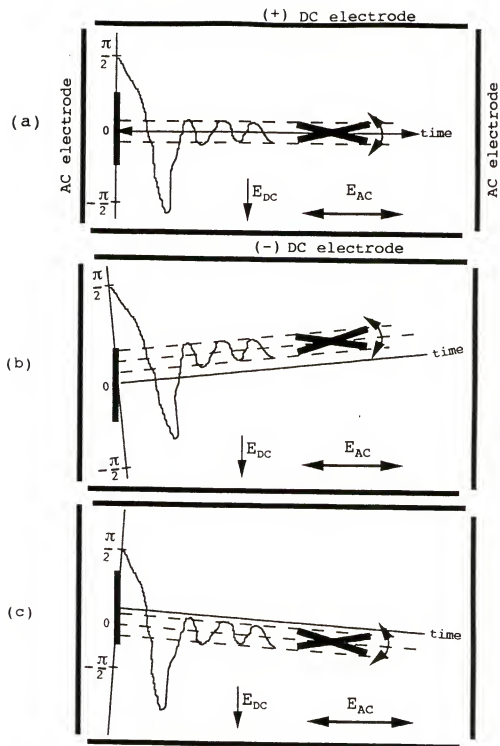


Figure 6-3 The schematic showing the relation between electrophoretic deposition configuration and the simulation data plot of particle orientational motion behavior with vibration axis: (a) parallel, (b) positively inclined, and (c) negatively inclined to the applied AC electric field orientation.

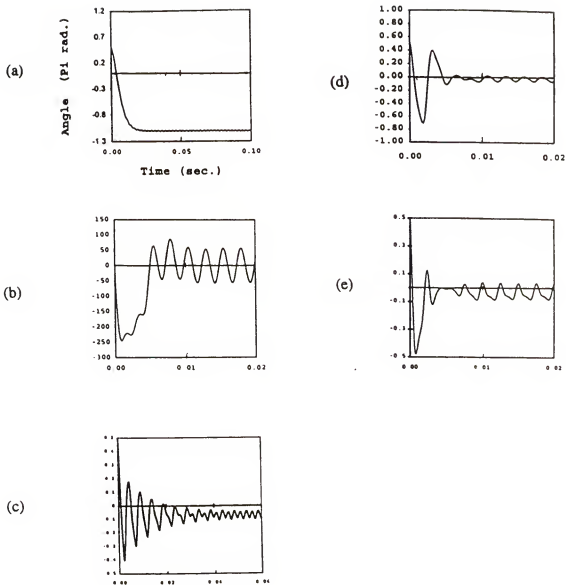


Figure 6-4 The plot of computer numerical simulation expressing platy BSCCO particle orientation behavior as a function of time in modified electrophoretic deposition at E_{DC} 40 v/cm, 200 Hz E_{AC} = (a) 40, (b) 100, (c) 200, (d) 300, and (e) 500 v/cm.

orientation motion on the applied AC electric field strength. However, with these processing parameters, the results show general E_{AC} effects on particle's angular vibration motion behavior. As E_{AC} increases:

- (i) the time-averaging angular vibration orientation (thereafter called angular vibration axis) of particle's major face is approaching E_{AC} orientation;
- (ii) the amplitude of particle's angular vibration decreases for $E_{AC} \leq 300$ v/cm
- (iii) the frequency of particle angular vibration in the stable range (attenuated stage of each curve) is kept at 400 Hz (double the E_{AC} 's).

With increasing E_{AC} range < 100 v/cm, the stable amplitude (as attenuated) of the angular vibration seems increasing shown in Figure 6-4(a) & (b). With E_{AC} in the vicinity of 200 v/cm [shown in Figure 6-4(c)], the time to reach stable particle angular vibration seems longer than that 0.01 second for lower or higher E_{AC} cases, and the wave form was modulated at the stable stage. At high E_{AC} cases (300 & 500 v/cm) shown in Figure 6-4(d) & (e), the curves look similar, except the one for 500 v/cm has modulated wave form after reaching stable stage.

This simulation results bring out an important feature pertinent to c-axis texturing enhancement of BSCCO particles: higher E_{AC} leads to the particle's angular vibration axis approaches E_{AC} orientation, that is, the major face of the plate-like particle is more parallel to substrate surface.

This result conforms to the observed experimental results in the modified electrophoretic deposition.

6.3.2 AC Frequency Dependence Of Angular Motion Behavior Of Plate-like Particle

The influence of AC electric field frequency on the orientation motion behavior of plate-like BSOCO particle is studied by computer simulation modeling shown in Figure 6-5. Above 200 Hz of AC field, the time needed to reach steady state also the same as 0.0112 second. The steady angular vibration frequency of BSOCO particle is always double that of the applied E_{AC} . All wave forms of steady angular vibration are almost the same, except at E_{AC} frequency 200 Hz. Observed from these simulated data curves in Figure 6-5, the clear dependence of steady particle's angular vibration amplitude on AC electric field frequency is depicted in Figure 6-6, while the particle vibration axis fixed at an angle -0.0784 radian ($=-4.47^\circ$) inclined to E_{AC} orientation. The results indicated that AC electric field frequency merely affects the angular vibration amplitude of plate-like particle. With the same E_{AC} magnitude applied at stable stage, the reduced period of AC field switching can decrease the time for the angular acceleration of plate-like particle. Hence, the maximum amplitude of angular vibration of particle reduces accordingly. During steady stage, the viscosity force is dynamically equilibrium with AC electric force, so the liquid damping forces can no longer change particle's orientation

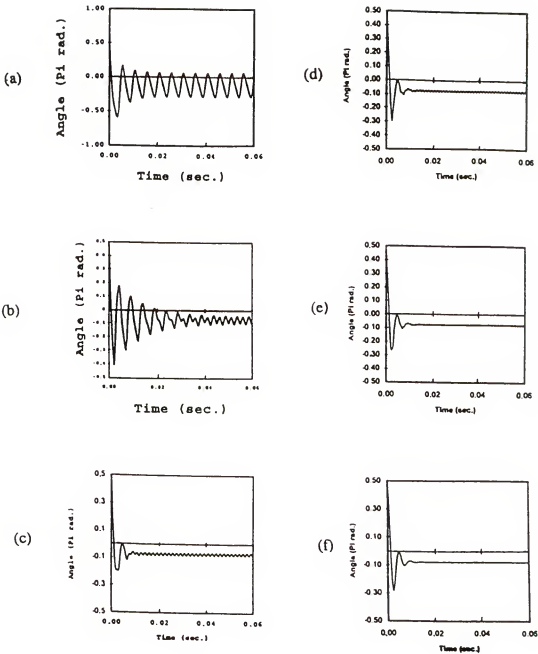


Figure 6-5 The plot of computer numerical simulation expressing platy BSCCO particle angular vibration motion behavior as a function of time in modified electrophoretic deposition at E_{DC} 40 v/cm, E_{AC} 200 v/cm, frequencies: (a)100, (b)200, (c)300, (d)400, (e)500, and (f)1000 Hz.

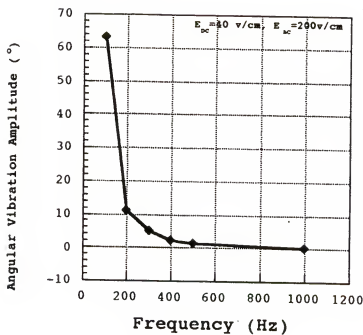


Figure 6-6 The plot showing the attenuated angular vibration amplitude of the platy particle as a function of applied AC electric field frequency obtained from Figure 4-22, and original angle at $\pi/2$ radian with respect to AC field.

motion behavior at steady state.

These computer simulation results are consistent with the concept discussed in explanation for experimental results of AC field frequency effect on particle c-axis texturing.

6.3.3 DC Electric Field Strength Effect On Angular Motion Behavior Of Plate-like Particle

Different DC electric field strength effect were conducted to simulate the angular motion behavior of plate-like party at constant E_{AC} condition as 200 v/cm and 200 Hz shown in Figure 6-7. Obviously, as E_{DC} magnitude increases: (i) the time-averaged orientation (TAO) of plate-like particle at steady state deviates slightly from E_{AC} to E_{DC} orientation shown in Figure 6-8(a); (ii) the steady-state angular vibration amplitude of plate-like particle orientation non linearly (initially slower) increases shown in Figure 6-8(b); and (iii) the time needed to reach steady state (t_{stead}) non linearly (initially faster) decreases shown in Figure 6-8(c). It is noticed that E_{DC} is applied simultaneously perpendicular to E_{AC} and substrate surface.

As E_{DC} increases, the induced electric dipole associating with plate-like particle's major face orientation experiences more DC electric force from the perpendicular direction to E_{AC} . The DC field induced torque is competing with AC's. Thus, the TAO axis of plate-like particle deviates more away from E_{AC} orientation with higher DC electric field

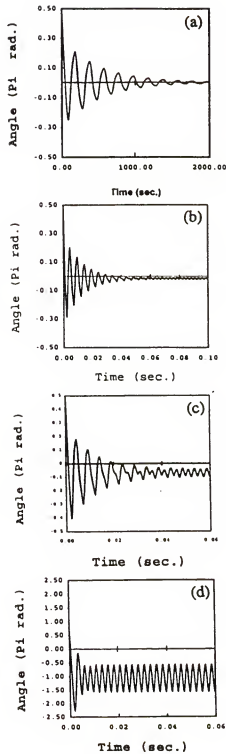


Figure 6-7. The plot of computer numerical simulation expressing platy BSCCO particle orientation behavior as a function of time in modified electrophoretic deposition at E_{AC} 200 v/cm, 200 Hz, E_{DC} = (a) 0, (b) 20, (c) 40, and (d) 200 v/cm.

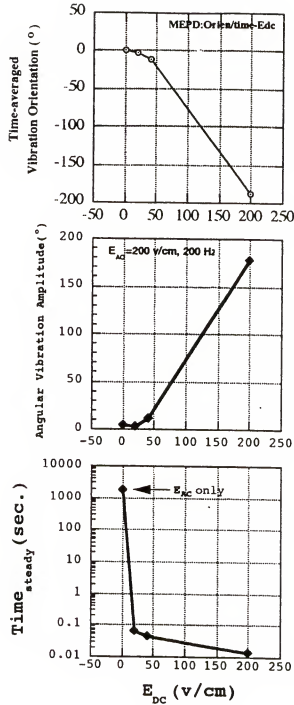


Figure 6-8 The plot of DC electric field strength effect on the angular vibration motion behavior of platy particle at constant $E_{AC}=200$ v/cm, 200 Hz at steady state: (a) time-averaged vibration orientation, (b) angular vibration amplitude, and (c) the time need to reach steady state, analyzed from simulation results in Figure 4-24.

strength. It is also consistent that the reduced c-axis texturing enhancement factor with E_{DC} resulted in modified electrophoretic deposition experiments, due to more deviation of TAO axis away from the substrate surface orientation, i.e., incident particle's major face orientation changes less parallel to the substrate surface by higher E_{DC} . Similarly, the increasing E_{DC} brought about larger steady-state angular vibration amplitude of plate-like particle, which resulted in less probability of depositing plate-like particles with their major face parallel to substrate surface, i.e., less c-axis texture. The reducing of t_{stead} with higher E_{DC} strength indicates that stronger attenuation force exerting on the simulated plate-like particle due to DC electric force is not a restoring force as AC's. Integrating the data in Figure 6-8 (b) and (c), it was found that, with increasing E_{DC} strength, the reducing of t_{stead} is corresponding to the increasing steady-state angular vibration amplitude. This result is very logical, since the plate-like particle experiencing larger angular vibration amplitude will attenuate faster, that is, faster to reach steady vibration state. therefore, the t_{steady} becomes shorter. However, this DC electric force related electrokinetic behavior is not the focused point in this study and was not observable in actual experiments.

From the above computer simulation modeling results, it appears that high E_{AC} strength and frequency are favorable for enhancing the c-axis texturing under low DC electric field strength and the presented electrode configuration.

However, it is also important to study the DC electric field strength effect on the angular motion behavior of plate-like particle at high AC electric field and high AC frequency. E_{AC} of 500 v/cm and 1000 Hz was then applied to the simulation program as the optimized condition, while two different E_{DC} strengths, 20 and 40 v/cm were respectively tested in the following simulation study.

6.3.4 DC Electric Field Strength Influence On Angular Motion Of Plate-like Particle Under High AC Electric Field And Frequency

Figure 6-9 shows the weak DC electric field strength effect on the angular vibration behavior of plate-like particle under E_{AC} 500 v/cm of 1000 Hz. At very weak E_{DC} 20 v/cm, it appears that E_{DC} does not deviate the time-averaged vibration orientation (in the order of $10^{-3}\pi$) away from E_{AC} orientation shown in Figure 6-9(b). As the E_{DC} doubles as 40 v/cm shown in Figure 6-9(a), the time-averaged vibration orientation slightly inclines to E_{DC} orientation, and the angular vibration amplitude also slightly increases (still in the order of $10^{-3}\pi$), although the curve seems the same shape with the downward-translated curve of E_{DC} 20 v/cm. This result indicates that, no matter how high the E_{AC} parameters are, DC electric field can affect orientation motion behavior of plate-like particle, as long as the field strength is high enough as 40 v/cm. Again, the DC field strength can not change the angular vibration frequency of the plate-like particle, but the time to reach steady state

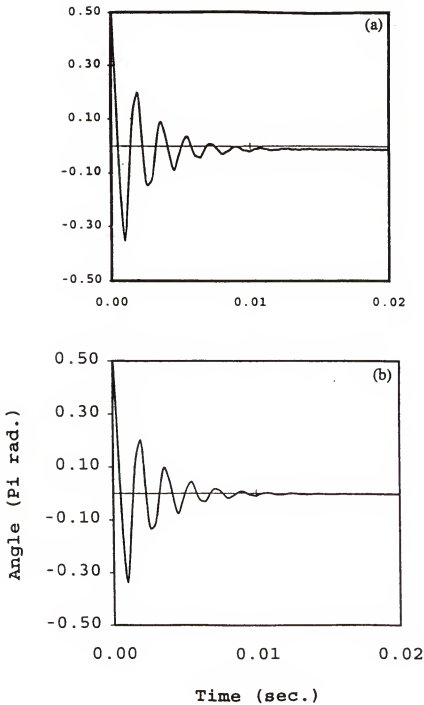


Figure 6-9 The plot of computer numerical simulation expressing platy BSCCO particle orientation behavior as a function of time in modified electrophoretic deposition at E_{AC} 500 v/cm, 1000 Hz, E_{DC} = (a) 40 v/cm, and (b) 20 v/cm.

(mentioned in the previous section).

The simulation results show that not only the ratio of AC to DC field strength influence the angular motion behavior of plate-like particle discussed in the previous sections, but also the absolute values. All the above modeling are based on the same original particle orientation at $\pi/2$, i.e., perpendicular to E_{AC} orientation, which is the largest angle to convert a-axis texture into c-axis texture in the AC field modified electrophoretic deposition. In the following simulation study, different original orientations of plate-like particle were applied to conduct the study.

6.3.5 Original Orientation Influence On The Angular Motion Behavior Of Plate-like Particle

With the same processing parameters ($E_{AC}=200$ v/cm at 200 Hz and $E_{DC}=40$ v/cm) in the simulation model, Figure 6-10 shows the influences of particle's original orientation on the axis orientation and amplitude of particle's angular vibration at steady state. The Figure also reveals that the time to reach steady state is independent of the original orientation of plate-like particle, except that at 0π , i.e., parallel to E_{AC} orientation. As the original orientation of plate-like particle is more deviated away from E_{AC} orientation, the angular vibration axis initially slightly deviated at $-3 \times 10^{-3}\pi$ radian from E_{AC} orientation shown in Figure 6-10(a) & (b), then approach E_{AC} orientation shown in Figure 6-10(c) & (d). Above $\pi/4$ radian

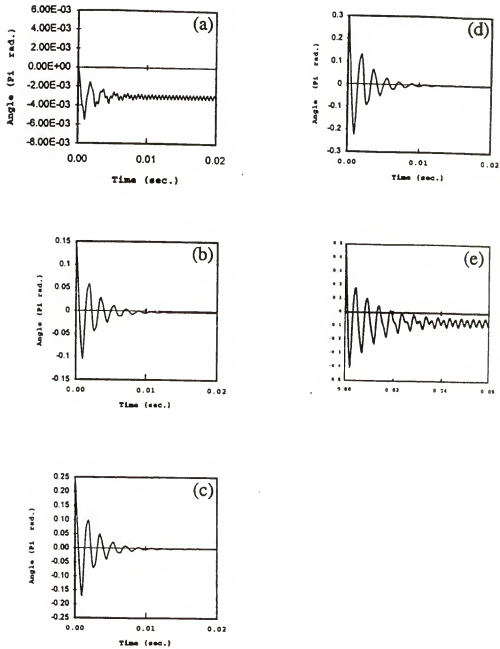


Fig. 6-10 The plot of computer numerical simulation expressing platy BSCCO particle orientation behavior as a function of time in modified electrophoretic deposition at E_{DC} 40 v/cm, E_{AC} 200 v/cm of 200 Hz and initial angles: (a) 0π , (b) $\pi/6$, (c) $\pi/4$, (d) $\pi/3$, and (e) $\pi/2$ radian with respect to E_{AC} orientation.

of original angle, it appears the curves similar except the only difference in their angular vibration amplitudes before reached steady state shown in Figure 6-10 (c) & (d). For the original angle at $\pi/2$ radian, the orientation motion behavior is different from that at smaller original angles due to different initial mechanism for inducing the particle rotation torque discussed in the section of the modeling of AC electric field strength effect. The most wandered result is that at zero degree of original angle shown in Figure 6-10(a). That is, the application of AC and DC electric fields still can very slightly deviate (in the order of $10^{-3}\pi$ rad.) the TAO axis and angularly vibrate the plate-like particle even though particle's original orientation is parallel to E_{AC} . Although the no torque action on particle by E_{DC} at the zero degree of original angle, as the E_{AC} starts to angularly vibrate the particle with a small amplitude, the particle then can experience the torque by $E_{DC} \geq 40$ V/cm. Within half cycle of AC frequency, as the weak E_{DC} -driven torque can affect the particle orientation at a given very small amplitude, the strong AC electric field induced torque still dominates over the DC's, and leads to the particle orientation approaching the E_{AC} orientation. When the particle orientation is approaching toward E_{AC} 's, the E_{AC} -induced torque gradually weakens again according to Equation (6-2). Over a period of time, the above dynamic phenomena repeats itself, and eventually reach steady state. For original angle larger than zero, the E_{AC} -induced torque dominates initially,

and results in larger particle rotation angle during initial unstable stage.

6.4 Summary

Considering the electric force effects on controlling plate-like particle orientation, the physical model had been successfully derived for c-axis texturing enhancement of BSCCO films by modified electrophoretic deposition with additional AC electric field parallel to substrate surface. Computational simulation of this orientation motion behavior of plate-like particle also had been conducted to theoretically elucidate the experimental results in AC-field modified electrophoretic deposition. Non-linear second order differential equations was derived to express the orientation motion behavior of induced dipole moment associated with the plate-like particle geometry. Basic dispersion condition effect on BSCCO particle texturing revealed that: (i) larger particle size was found preferred to have better particle orientation control by uniform applied electric fields, and (ii) lower dispersion solution of BSCCO particles was suitable for higher c-axis texturing enhancement in conventional EPD. Stronger DC electrophoretic field can align particle-geometry-preference-induced electric dipole, which is associated with particle major face, and resulted in less c-axis texture or enhanced more particle deposited with their major face perpendicular to substrate surface. The detailed

discussion for DC field effect on particle orientation control also considered the fluid dynamics effect such as fluid dynamic drag, and Brownian motion effects, which merely contribute several order lower in magnitude than applied electric force induced torque. Stronger additional AC electric field parallel to substrate surface was found enhanced the c-axis texturing due to bringing the angular vibration axis closer to AC field orientation. Higher AC field frequency also can enhance c-axis texturing by reducing the angular vibration amplitude of plate-like particle in the dispersion. Both the absolute values and ratio of AC to DC field strength can influence the orientation motion behavior of plate-like BSCCO particles. Generally, the original orientation of plate-like particle merely affects the damping amplitude of angular vibration of plate-like particles, and no significant impact on the steady angular vibration axis orientation. As similar to restoring force, AC electric field controls the amplitude, frequency and axis orientation of particle's angular vibration behavior, while DC electric field (perpendicular to AC's) can only control the angular vibration axis orientation of particle major face toward substrate, and the time to reach steady state. The computer simulation results conform to the physical model to explain the experimental results.

CHAPTER VII

CONCLUSIONS

In this study, the systematic investigations of Ag-sheathed BSCCO thick film microstructure control were conducted to improve superconductivity and mechanical characteristics via improving pre-sintering microstructure by electric force, mechanical force and thermal force. Sequential micro-lamination of additional AC electric field modified electrophoretic deposition processing and thermomechanical consolidation was found effectively for (i) increasing film microstructure density and (ii) c-axis texturing enhancement without cracking and bending BSCCO particles, resulting in, superconductivity stability improvement. For the modified electrophoretic deposition with additional AC electric field parallel to substrate surface, the mechanism of c-axis texturing enhancement of BSCCO films was physically modeled and computationally simulated considering the particle-geometry-preference-induced electric dipole associated with a plate-like BSCCO particle under AC/DC fields in suspension solution. Based on numerical solution for the secondary non-linear differential equations describing the physical model of ACEPD, computational simulations of angular motion behavior of plate-like BSCCO

particle in suspension solution were conducted to explain the experimental results. It has been discussed that Electric interaction dominates over fluid dynamic drag force and Brownian motion force. This study also contributes to revealing the novel scope of angular motion behavior of the plate-like particle under the dual influence of AC and DC electric fields in suspension solution, using an integrated method of computational simulation and experimental microstructure characterization.

The parameter effects of post-deposition processing on the c-axis texturing enhancement and the resultant superconductivity of sintered Ag-sheathed tape/wire was studied considering the average BSCCO particle size and process sequence difference influence. Regarding to mechanical force effects on c-axis texturing enhancement of as-deposited BSCCO films, the uniaxial pressure dependence of c-axis texturing enhancement was studied. The influences of particle size (or aspect ratio) and Ag sheath on c-axis texturing enhancement were also investigated. As the c-axis texturing enhancement factor C_x of BSCCO films increased with the applied uni-axial pressure at room temperature, the resultant critical current density decreased due to particle cracking and bending by too high mechanical pressure. However, the cold pressing on pre-sintering BSCCO films did not improve the ab-plane grain boundary coupling of sintered tape/wire, due to no enhanced inter-particulate binding in pre-sintering microstructure prepared at room temperature.

Applying thermal energy to pre-sintering BSCCO film processing, the c-axis texturing enhancement dependence on consolidation temperature was investigated. Larger than the cold pressed values, the C_x values increased with increasing consolidation temperature at constant uni-axial pressure. It was found that the process sequence of pressing and heating could affect the c-axis texturing enhancement. Higher temperature for thermomechanical consolidation of pre-sintering films was found to not only improve the intergranular coupling, but also to improve the intragranular pinning force density of sintered films due to reducing particle cracking breaking and bending during consolidation process.

Tape/wire strengthening study was conducted mainly considering the effects of silver particle interlayer and average BSCCO particle size. Electrophoretically deposited Ag particle interlayer in the middle of BSCCO thick films showed effective and economical improvement in fracture strength and Ag/BSCCO interface adhesion strength of Ag-sheathed BSCCO films, using T-peel test for mechanical characterization method.

Estimated from magnetic hysteresis loops and by extended Bean critical state model, the critical current density of polycrystalline BSCCO thick films was increased and found more stable under applied magnetic fields and less temperature dependence for samples prepared by AC-field modified electrophoretic deposition than conventional EPD;

although, the post-deposition process condition was the same. It is due to (i) the much less defects introduced by particle cracking and bending during pre-sintering processing, (ii) reduced number density of micro-pores and micro-pore size.

By controlling the plate-like particle orientation in suspension solution, the c-axis texturing enhancement employing ACEPD had been proved working for improving the superconductivity of Ag-sheathed BSCCO tape/wire. In the future research the powder prepared by whisker crystal growth of plate-like BSCCO particles may be the right direction for further improving the c-axis texturing enhancement efficiency of ACEPD method. With the longest dimension of plate-like particle along the a-axis or b-axis of BSCCO crystallographic structure, the in-plane a-axis texture can be achieved; thus, three-dimensional texturing of BSCCO films can be deposited by the ACEPD technique, hopefully resulting in superior superconductivity than that prepared by the other HTS tape/wire fabrication techniques.

APPENDIX A

MAJOR X-RAY DIFFRACTION PEAKS OF BSCCO PHASES

The Table of the major x-ray diffraction peaks of BSCCO
(a)2212 and (b)2223 phases.

(hkl)	2 θ	I / I _o
0 0 2	5.75*	34.1
0 0 8, 1 1 1	23.20*	48.3
1 1 3	24.90*	35.6
1 1 5	27.52*	100.0
0 0 <u>10</u>	29.15	35.7
1 1 7	31.00*	74.5
2 0 0, 0 2 0	33.20	67.9
1 1 8, 0 0 <u>12</u>		
2 0 4, 0 2 4	35.15*	45.8
1 1 9		
2 0 <u>10</u> , 0 2 <u>10</u>	44.71	34.8
0 0 <u>16</u> , 2 2 0	47.60	34.0
0 0 <u>17</u>	50.65*	28.5
3 1 5, 1 3 5	55.90*	16.8
1 1 <u>17</u>	56.35*	9.5
3 1 7, 1 3 7	57.95*	20.2
0 0 <u>20</u>	60.50	26.2

(h k l)	2 θ	I / I _o
0 0 2	4.7*	29
1 1 1	23.43	10
0 0 <u>10</u>	23.98*	29
1 1 3	24.40	19
1 1 5	26.25*	57
1 1 7, 0 0 <u>12</u>	28.83	88
1 1 9	31.94	53
2 0 0	33.17	100
0 0 <u>14</u>	33.77*	28
1 1 <u>11</u>	35.52*	25
2 0 <u>12</u>	44.60	23
2 2 0	47.61	40
1 1 <u>17</u> , 2 0 <u>14</u>	48.06*	19
1 1 <u>19</u>	52.6*	19
0 0 <u>24</u>	59.9	25

*: denotes characteristic peak

APPENDIX B

BEAN CRITICAL STATE MODEL

This model is usually used to estimate the intrinsic J_c or intragranular contribution of the J_c . It is based on the relation between the Lorentz force induced bulk current inside the superconductor and the external magnetic field. The geometric dimensions of the superconductor are also involved in the relation. The gradient of flux lines exists as flux is driven into an inhomogeneous mixed-state superconductor [Kim62, Fried63, Silco63]. The magnetic field within the specimen decreases linearly with depth as a consequence of Ampere's law, $\text{curl } \mathbf{H} = 4\pi \mathbf{J} / 10$. In the initial stages of magnetization, as the external magnetic field penetrates into the superconductor surface thickness d just enough to reduce the internal local field to zero, i.e., $d = 10H / 4\pi J_c$ [Bean64]. The magnetization curve is size-dependent. The plot of the relationship is Shown in Figure 2'.

For general consideration, the J_c is a function of the external magnetic field as Figure 3'. H_c is the critical field which magnetizes completely the specimen, $H_c(H) = \pi J_c(H) d / 5$. $J_c(H)$ is the current density appropriate to the field at the surface.

Considered with the anisotropy, the Bean Model was extended for high- T_c superconducting oxide of rectangular parallelepiped sample with perpendicular applied magnetic field to one face of the dimensions L by t [Gyor89].

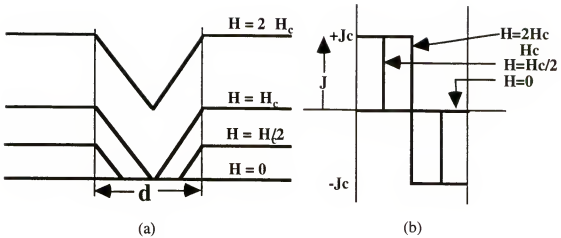


Figure 2' A plot of (a) local fields and (b) current density, as well as magnetization curves for fields 0, $H_c/2$, H_c , and $2H_c$ applied parallel to the sample surface of a slab of thickness d . The critical current density

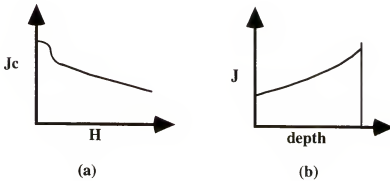


Figure 3' Plots of the effects of the current density J_c depending on field H (a) a schematic curve showing this dependence; (b) the current at a plane surface for a applied field H .

The relation between magnetization width in the hysteresis loop and the critical current density J_c with dimensional effect for $k < p/2$ or $J_{c1}/J_{c2} < p/t$ is given as

$$\Delta M = \frac{J_{c1} t}{20} \left(1 - \frac{t}{3p} \frac{J_{c1}}{J_{c2}} \right)$$

where ΔM (emu/cm³) is the difference between the upper and lower magnetization branches in a given field and t (cm) and p (cm) ($t < p$). For square prism ($p=t$) or a cylinder of diameter t , J_c can be expressed as $J_c = 30\Delta M/t$.

For $J_{c1}/J_{c2} > p/t > 1$ case, where $h/k = J_{c1}$ and $2h/p = J_{c2}$, the equation becomes

$$\Delta M = \frac{J_{c2} p}{20} \left(1 - \frac{p}{3t} \frac{J_{c2}}{J_{c1}} \right)$$

The information of J_c obtained from the Bean model is only the intragranular contribution, i.e., the intrinsic J_c as a function of the applied magnetic field. The field dependence of superconductivity is related to its intrinsic properties.

APPENDIX C

**COMPUTER SIMULATION PROGRAM C++ CODES FOR
ANGULAR MOTION BEHAVIOR OF PLATE-LIKE BSCCO
PARTICLE BY ACEPD**

```

/*****
*   compute the rotational vibration of a dipole in two
*   perpendicular DC and AC electric fields with damping,
*
*   the equation of motion is
*    $d^2 x / d t^2 = - \mu dx/dt / I + f(x,t)/I$ 
*   where  $f(x,t) = -p \cdot E \cos^2(w t) \sin(x) - p_0 \cdot E_0 \cdot \cos(x)$ 
*
*   x is angle; I is inertia
*****/

#include <iostream.h>
#include <fstream.h>
#include <math.h>

main()
{
    double e0,e,w,frequency,area,thickness,rho,chi,x,eta,total_time,p0;
    double
pi=3.1415926,mu,volume,mass,inertia,p,dt,t=0.0,v=0.0,dx,dv,force;
    int Nstep;

// read from "input_c" file
ifstream fin("input_c");
//open "input_c" file
//DC electric field, unit V/cm
//electric field, unit V/cm
//frequency, unit Hz
//area of slab, unit micron^2
//thickness of slab, unit nanometer
//ion layer thickness, unit nanometer
//density of slab, unit g/cm^3
//polarizability
//original angle theta
//viscosity constant
//time to compute x and v, unit sec
//total of steps to take
//close "input_c" file
    fin >> e0;
    fin >> e;
    fin >> frequency;
    fin >> area;
    fin >> thickness;
    fin >> layer_thickness;
    fin >> rho;
    fin >> chi;
    fin >> x;
    fin >> eta;
    fin >> total_time;
    fin >> Nstep;
    fin.close();

```

[illegible]

REFERENCES

- Alner65 D. J. Alner, "Aspect of Adhesion", Proc. Conf. Northampton college of Advanced Technology, 20 and 21 march, 1963, University of London Press (1965).
- Ayy95 Pushan Ayyub, V. R. Palkar, Soma Chattopadhyay, and Manu Multani, *Phys. Rev. B* **51**(9), 6135-8(1995).
- Babco90 S. E. Babcock and D. C. Larbalestier, *J. Mater. Res.* **5**(5), 919-928(1990)
- Bach89 Ram Bachan, "Implications of Pressure Diffusion for Shock Waves", (microfiche)report to National Aeronautics and Space Administration, Springfield, Va., National Technical Information Service (1989).
- Bharg96 Atit Bhargava, Ian D. R. Mackinnon, Toru Yamashita, and Jose Alarco, *J. electronic Mater.*, **24**, 1851(1995).
- Braue92 D. J. Brauer, D. Busch, R. Eujen, A. Gladun and J. Hudepohl, *Cryogenics* **32** (11), 1052-5(1992).
- Bean64 Charles P. Bean, *Rev. Modern Phys.* **36**, 31-39(1964).
- Bird60 R. Byron Bird, W. E. Stewart, and E. N. Lightfoot, "Transport Phenomena", John Wiley & Sons, New York, (1960).
- Blenv84 Robert D. Blenvins, "Applied Fluid Dynamics Handbook", van Nostrand Reinhold Company, New York, 335 & 342-47(1984).
- Bra95 J. W. Bray, *J. Electron. Mat.*, **24**(12), 1767(1995).
- Bula92 L. N. Bulaevskii, J. R. Clem, L. I. Glazman, and A. P. Malozemoff, *Phys. Rev. B* **45**, 2545 (1992).
- Cardo93 A. H. Cardona, H. Suzuki, T. Yamashita, K. H. Young and L. C. Bourne, *Appl. Phys. Lett.* **62**, 411-4(1993).
- Cassi92 S. M. Cassidy, L. F. Cohen, M. N. Cuthbert, S. X. Dou and A. D. Caplin, "Unusual form of the

- temperature and field dependence of the grain boundary weak-link dissipation in Ag-sheathed BSCCO(2223) tape, *Cryogenics* **32**(10), 1034-7(1992).
- Chaud87 P. Chaudhari, J. Manhart, D. Dimos, C. C. Tsuei, J. Chi, M. M. Oprysko, and M. Scheuermann, *Phys. Rev. Lett.* **59**, 1475-1478(1987).
- Coo88 Emanuel I. Cooper, Edward A. Giess and Arunava Gupta, *Mater. Lett.* **7** (12), 5-8(1988).
- Courc79 J. Courchesne, and A. Lanville, "A comparison of Correction Methods Used in the Evaluation of Drag Coefficient Measurements for Two-Dimensional Rectangular Cylinders", *J. Fluids Eng.* **101**, 506-510(1979).
- Della91 Christopher Dellacorte, et al., "Tribological Characteristics of Silicon Carbide Whisker Reinforced Alumina at Elevated Temperature", (microfiche) report to National Aeronautics and Space Administration, Springfield, Va., National Technical Information Service (1991).
- Dim88 D. Dimos, P. Chaudhari, J. Manhart, F. K. Legoues, *Phys. Rev. Lett.* **61**, 219-222(1988).
- Dim90 D. Dimos and P. Chaudhari, *Phys. Rev. B* **41**(7), 4038-4049(1990).
- Dov89 R. V. van Dover, E. M. Gyorgy, L. F. Schneemeyer, J. W. Mitchell, K. V. Rao, R. Puzniak, and J. V. Waszczak, *Nature* **342**, 55 (1989).
- Ekin92 J. W. Ekin, D. K. Finnemore and Qiang Li, J. Tenbrink, W. Carter, *Appl. Phys. Lett.* **61**(7), 858-860(1992).
- Enomo90 N. Enomoto, "The transport critical current properties of BSCCO superconducting wires", *Proceedings the third International Symposium on Superconductivity*, Sendai, Miyagi-Ken, Japan (November 6-9, 1990).
- Fried63 J. Friedel, P. G. DeGennes, and J. Matricon, *Appl. Phys. Lett.* **2**, 119-126(1963).
- Ginz88 V. L. Ginzburg, "Macroscopic theory for superconductors with small coherent length", *Physica C* **135-155**, 1617-1621(1988).

- Golds38 S. Glodstein, "Modern Development in Fluid Dynamics", Oxford Univ. Press, London, 439(1938), cited by Robert D. Blenvins, "Applied Fluid Dynamics Handbook", van Nostrand Reinhold Company, New York, 335(1984).
- Goy94 A. Goyal, E. D. Specht, Z. L. Wang, and D. M. Kroeger, J. A. Sutliff, J. E. Tkaczyk, J. A. Deluca, L. Masur and G. N. Riley, Jr. J. Electron. Mater. **23**(11), 1191-1197(1994).
- Goy95 A. Goyal, E. D. Specht, D. M. Kloege, T. A. Mason, D. J. Dingley, and G. N. Riley, J. Electron. Mat., **24**(12), 1865(1995).
- Gra95 M. P. Grant, Nature, **375**, 107 (1995).
- Greut90 F. Greuter, C. Schuler, P. Kluge-Weiss and W. Paul, Advances in Superconductivity II, ed. T. Ishigura and K. Kajimura (Tokyo: Springer-Verlag), 377(1990).
- Gui88 Mark R. De Guire, Cheol J. Kim, Wen-Haw Lu, David E. Farrel and Daniel Boyne, Ceramic Superconductors **II**, Editor Man F. Yan, Amer. Ceram. Soc. Westerville, Ohio, U. S. A. 343-355(1998).
- Gyo89 E. M. Gyorgy, R. B. van Dover, K. A. Jakson, L. F. Schneemeyer, and J. V. Waszczak, Appl. Phys. Lett. **55**(3), 283-285(1989).
- Hamak40 H. C. Hamaker, "Formation of Deposition by Electrophoresis", Trans. Faraday Soc., **36**, 279-87(1940).
- Han90 P. D. Han and D. A. Payne, Journal of Cryst. Grow. **104**, 201-210 (1990).
- Hens93 B. Hensel, J.-C. Griel, A. Jeremie, A. Perin, A. Pollini, and R. Flükiger, Physica C **205**, 329-337(1993).
- Hens95 B. Hensel, G. Grasso, and R. Flukiger, Phys. Rev. B **51**, 15456 (1995).
- Hells92 E. E. Hellstrom, MRS Bull, **17**(8), 45-51(1992).
- Hertz83 R. W. Hertzberg, Deformation and Fracture Mechanics of Engineering Materials, Wiley, Chichester, 246(1983).

- Ho91 J. C. Ho, H. B. Liu, C. Y. Wu, P. G. Wahlbeck, D. L. Meyers, and S. He, IEEE Transactions on Magnetics, **27**, 1438(1991).
- Ho96 Paul S. Ho, "Stress-induced Phenomena in Metallization", New York, American Institute of Physics(1996).
- Ichin88 N. Ichinose and T. Motai, "Ceramic Superconductors II", American Ceramic Society, Inc. Westerville, Ohio, 162168(1988).
- Iri94 Fujio Irie, "Composite Superconductors", Edited by Kozo Osamura, Marcel Dekker, Inc., New York, 5-18(1994).
- Israe92 Jacob N. Israelachvili, "Intermolecular & Surface Forces", Academic Press, San Diego (1992).
- Israe92 Jacob N. Israelachvili, "Intermolecular & Surface Forces", 57-63(1992), Academic Press, San Diego.
- Iye95 A. N. Iyer, R. Jammy, U. Balachandran, M. Suenaga, and P. Haldar, J. Electron. Mater. **24**(12), 1873-1876(1995).
- Jagan92 K. Jagannadham and J. Narayan, Mater. Res. Soc. Proc. **275**, 597-608(1992).
- Jahan94 Edited by Said Jahanmir, "Friction and Wearing of Ceramics", New York, M. Dekker publication(1994).
- Jin88 S. Jin, R. C. Sherwood, E. M. Gyorgy, T. H. Tiefel, R. B. van Dover, S. Nakahara, L. F. Schneemeyer, R. A. Fastnacht, and M. E. Davis, Appl. Phys. Lett. **54**(6), 584-6(1988).
- Kao93 C. H. Kao, H. Y. Tang, Y. S. Shiue, S. R. Sheen, M. K. Wu, J. Mater. Sci. Lett., **12**, 1793(1993).
- Kas90 J. I. Kase, K. Togano, H. Kumakura, D. R. Dietderich, N. Irisawa, T. Morimoto, H. Maeda, Jpn. J. Appl. Phys. **29**, L1096(1990).
- Kat92 T. Kato, T. Hikata, M. Ueyama, K. Sato, and Y. Iwasa, MRS Bull., **17**(8), 52-54(1992).
- Kawas94 Masashi Kawasaki and Masashi Nantoh, Mater. Res. Soc. Bull. **19**(9), 33-38(1994).

- Khar90 Neeraj Khar, et al., Supercond. Sci. & Tech. **3**, 514-516(1990).
- Kim61 Y. B. Kim, C. F. Hempstead, and A.R. Strnad, Phys. Rev. Lett. **9**, 306-311(1962).
- Kinge76 W. D. Kingery, H. K. Bowen, and J. R. Uhlmann, "Introduction to Ceramics" 2nd Ed., John Wiley & Sons, New York, 452-61(1976).
- Kou91 N. Koura nad H. Shoji, Physica C **190** (1-2), 163-4(1991).
"Preparation of High-T_c superconductors by electrophoretic deposition method. Study on the substrate and electrolyte"
- Kou92 N. Koura nad H. Shoji, Physica C **200** (1-2), 50-54(1992), "BSCCO Superconductor Coating by Electrophoretic Deposition Method"
- Larbe93 D. C. Larbelestier, and M. P. Maley, MRS Bulletin, **18**, 50 (1993).
- Lei76 M. H. Leipold, in Treatise on Materials Science and Technology, Ceramic Fabrication Processes, Vol.9 (F. F. Y. Wang, ed.), Academic Press, New York, 95-134(1976).
- Li97 S. Li, M. Bredehoft, Q. Y. Hu, H. K. Liu, S. X. Dou, W. Gao, Physica C **275**, 259-265(1997).
- Livin90 Burton Edward Livingston, " The role of Diffusion and Osmotic Pressure in Plants", (microfiche) National Aeronautics and Space Administration, Springfield, Va., National Technical Information Service (1990).
- Lotge59 F. K. Lotgering, J. Inorg. Nucl. Chem. **9**, 113-123(1959).
- Malar90 J. A. Malarria, and D. A. Esparza, Proc. ICTP '90 Interference on Transport Properties of Superconductors, April 29-May 4, 1990, Riode Janeiro, Brazil, 615-619(1990).
- Manh88 J. Manhart, P. Chaudhari, D. Dimos, C. C. Tsuei, and T. R. McGuire, Phys. Rev. Lett. **61**, 2476-2479(1988).
- McGinn89 P. J. McGinn, W. Chen and M. A. Black, Physica C **161**, 198-204(1989).

- Menci92 J. Mencik, "Strength and Fracture of Glass and Ceramics", Elsevier, Amsterdam, 227(1992).
- Miyos88 Kazuhisa Miyoshi, et. al., "Adhesion and Micromechanical Properties of Ceramics", (microfiche) report to National Aeronautics and Space Administration, Springfield, Va., National Technical Information Service (1988).
- Mizug91 J. Mizuguchi, M. Suzuki, H. Yamato and M. Matsumura, J. Electrochem. Soc. **138**(10), 2942-6(1991)
"Charact. YBCO_{7-x} prepared by electrophoretic deposition"
- Muns94 Bruce R. Munson, Donald F. Young, and Theodore H. Okiishi, "Fundamental of Fluid Mechanics" 2nd Ed., Wiley & Sons, New York, 599(1994).
- Namg89 C. Namgung, et al., Supercond. Sci. & Tech. **2**, 182-184(1989).
- Nash92 A. S. Nash, K. C. Goretta, D. J. Miller, A. C. Biondo, Donglu Shi, S. Sengupta and R. B. Poeppel, MRS Proc. **275**, 311-317(1992).
- Nishi89 T. Nishio, Y. Itoh, F. Ogasawara, M. Suganuma, Y. Yamada, U. Mizutani, J. Mater. Sci., **24**, 3228-34(1989).
- Non89 T. Nonaka, M. Green, K. Kishio, T. Hasegawa, K. Kitazawa, K. Kaneko and K. Kobayashi, Physica C **160**, 517-523(1989).
- Oba93 Koichi Oba and Folke Björk, "The relationship between welding temperature and T-peel strength of heat-welded seams in single-ply roof-coverings", Adhesion Sci. Technol. **7**(9), 960-66(1993).
- Ohr92 Milton Ohring, "The Materials Science of Thin Films", Academic Press, San Diego, 439-46(1992).
- Osam94 Kozo Osamura, edit. "composite Superconductors", Marcel Dekker Inc., New York, 323-411(1994).
- Palst88 T. T. M. Palstra, B. Batlogg, L. F. Schneemeyer, and V. Waszcszak, Phys. Rev. Lett. **61**(14), 1662-1665(1988).

- Park95 C. Park, S. T. Mixture, D. Sriram, and R. L. Snyder, J. Electron. Mater., **24**(12), 1897-1901(1995).
- Parth94 S. Parthasarathi, M. D. Aesoph, D.-W. Yuan, J. Jo, and J. Kajuch, J. Electron. Mater. **23**(11), 1199-1202(1994).
- Pau92 W. Paul, B. Heeb, T. Baumann, M. Guidolin, and L. J. Gauckler, "Layered Superconductors: Fabrication, Properties and applications", MRS Proc. Vol. **275**, 383-389(1992).
- Port81 D. A. Porter and K. E. Easterling, "Phase Transformations in Metals and Alloys", Van Nostrand Reinhold, New York, etc., 203-221(1981).
- Purce65a Edward M. Purcell, "Electricity and magnetism", McGraw-Hill Company, New York, 307-14(1965).
- Purce65b Edward M. Purcell, "Electricity and Magnetism", McGraw-Hill Book Company, New York, 95-105(1965).
- Pust90 Ladislav Pust, Supercond. Sci. Technol. **3**, 598-601(1990).
- Rames88 R. Ramesh, and G. Thomas, S. M. Green, M. L. Rudee, H. L. Luo, Applied Phys. Lett. **53**, 520(1988).
- Ray91 R. D. Ray II and E. E. Hellstrom, Phys. C, **B175**, 255(1991).
- Rayne91 A. S. Raynes, S. W. Freiman, F. W. Gayle, D. L. Kaiser, J. Appl. Phys. **70**, 5254-5259(1991).
- Reed89.1 James S. Reed, "Principles of Ceramic Processing", New York, John Wiley & Sons, 336-342(1989).
- Reed89.2 James S. Reed, "Principles of Ceramic Processing", New York, John Wiley & Sons, 204-206(1989).
- Rile94 G. N. Riley, et al., Physica C, **235-240**, 3407 (1994).
- Ryan79 W. Ryan and E. Massoud, "Electrophoretic Deposition Could Speed Up Ceramic Casting," Interacram. **2**, 117-19(1979).
- Salam89 K. Salama, V. Selvamanickam, L. Gao, and K. Sun, Appl. Phys. Lett. **54**(23), 2352-4(1989).

- Sand91 Kenneth H. Sandhage, Gilbert N. Riley, and William L. Carter, *J. of Metals* **43**(3), 21-25(1991).
- Sarka92 P. Sarkar, X. Huang, and P. S. Nicholson, "Structural Ceramic Microlaminates by Electrophoretic Deposition," *J. Amer. Ceram. Soc.* **75**, 2907-909(1992).
- Sarka91 Patho Sarkar, S. Mathur, and P. S. Nicholson, *J. Appl. Phys.*, **69**, 1775(1991).
- Sarka94 P. Sarkar, O. Prakash, and P. S. Nicholson, "Micro-Laminate CERamic/Ceramic composites (YSZ/Al₂O₃)," *Ceram. Eng. Sci. Proc.*, **15**, 1019-27(1994).
- Sarka96 Partho Sarkar and Patrick S. Nicholson, *J. Am. Ceram. Soc.* **79**(8), 1987-2002 (1996).
- Sato90 K. Sato, et al, "High J_c Silver-Sheathed Bi-based Superconducting Wires", *Proc. Applied Superconductivity Conference, Snowmass Village, Colorado, Sept. 24, 1990*.
- Sche93 H. J. Scheel, in *Advances in Superconductivity VI*(6th Intl. Symposium on Superconductivity, Hiroshima, Oct.1993), edited by T. Jujita and Y. Shiohara (Springer, Tokyo), 29(1994).
- Schne88 H. G. von Schnering, L. Walz, M. Schwarz, W. Becker, M. Hartweg, T. Popp, B. Hettich, P. Muller, G. Kampf, *Angew. Chem. Int'l Ed. Engl.*, **27**, 574(1988).
- Sere94 J. W. Severin, A. A. M. van Weert and G. de With, *Thin Solid Films* **250**, 115-125 (1994).
- Sheng88 Z. Z. Sheng and A. M. Herman, *Nature*, **332**, 55(1988).
- Shi92 Donglu Shi, S. Sengupta, K. C. Goretta, S. Salem-Sugnui, Jr., M. Smith and Y. N. Lwin, *Proc. Mater. Res. Soc. Sym.* **275**, 609-615 (1992).
- Silco63 J. Silcox and R. W. Rollins, *Appl. Phys. Lett.* **2**, 231-236(1963).
- Singh93a J. P. Singh, J. Joo, D. Singh, T. Warzynski and R. B. Roepfel, *J. Mater. Res.* **8** (6), 1226-31(1993).
- Singh93b J. P. Singh, J. Joo, D. Singh, N. Vasanthamohan, and R. B. Roepfel, *J. Mater. Res.* **8** (8), 2458-64 (1993).

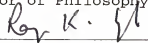
- Stekl95 Z. J. J. Stekly and E. Gregory, "High-Temperature Superconducting materials Science and Engineering: New Concepts and Technology", Editor: Donglu Shi, 441-474(1995).
- Subra88 M. A. Subramanian, C. C. Domenges, C. Michel, B. Raveau, *Mod. Phys. Lett.* **2**, 835(1988).
- Tabuc88 J. Tabuchi, Y. Shimakawa, and K. Utsumi, "Ceramic Superconductors II", American Ceramic Society, Inc., Westerville, Ohio, 464-473(1988).
- Taras88 J. M. Tarascon, Y. Lepage, P. Barboux, B. G. Bagley, L. M. Greene, W. R. McKinnon, G. W. Hull, M. G. Giroud, B. W. Hwang, *Phys. Rev.*, **B37**, 9382(1988).
- Tenb90 J. Tenbrink, M. Wilhelm, K. Heine, and H. Krauth, *Appl. Superconductivity Conf.*, Snowmass Village, CO, U. S. A. (September 24-28, 1990).
- Tenbr94 J. Tenbrink and H. Krauth, *Supercond. Sci. Technol.* **7**, 754-758(1994).
- Tomi92 N. Tomita, Y. Takahashi and Y. Ishida, *Jpn. J. Appl. Phys.* **31**, L942-5(1992).
- Toms97 Michael Tomsic and Asok K. Sarkar, *Superconductor Industry* **10**(1), 18-23(1997).
- Velz72 D. van Velzen, et al., "Liquid Viscosity", *Ind. Eng. Chem. Fund.* **11**, 20-41(1972), cited in Robert D. Blenivins', "Applied Fluid Dynamics Handbook", van Nostrand Reinhold Company, New York, 525-527(1984).
- Vie84 J. M. Vieira and R. J. Brook, "Kinetics of Hot Pressing: the Semilogarithmic Law", *J. Am. Ceram. Soc.* **67**(6), 245-249(1984).
- Web77 Harald Webber, edit., "Anisotropic Effects in Superconductors", Plenum Press, New York (1977).
- Willi95 J. O. Willis, R. D. Ray II, D. S. Phillips, K. V. Salazar, J. F. Bingert, T. G. Holesinger, J. K. Bremser, and D. E. Peterson, *J. Electron. Mater.* **24**(12), 1789-17929(1995).

- Woolf95 L. D. Woolf, T. L. Figueroa, R. A. Olstad, F. E. Elsner, and T. Ohkawa, J. Electron. Mater. **24**(12), 1797-1800(1995)
- Wu87 M. K. Wu et al. Phys. Rev. Lett., **58**, 908(1987).
- Yau94 John Yau and Nick Savvides, Appl. Phys. Lett. **65**(11), 1454-1456(1994).
- Yue97 Cheng-Feng J. Yue, D. Kumar, and Rajiv K. Singh, Physica C **279**, 197-202(1997).
- Yuh95 S. Yuhya, M. Hiraoka, T. Fukunaga, and A. Oota, J. Electron. Mater. **24**(12), 1839-1841(1995).
- Yun93 J. Yun, M. P. Harmer, and Y. T. Chou, Scripta Metallurgica et Materialia, **29**, 267-71(1993).

BIOGRAPHICAL SKETCH

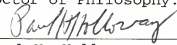
Cheng-Feng Yue was born as the first son (or third child) of the couple Chin-Yen Yue and Re-Yuen Chu on February 13, 1962, living with his two elder sisters and one younger brother in Taiwan, Republic of China. After graduated from Mining and Metallurgical Engineering Department in National Taipei Institute of Technology (the former of National Taipei University of Science and Technology), he served as a secondary lieutenant in Engineering Troop of China Army for about two years. Then he received the certificate of the intense Semiconductor Engineering Training of Sing-Chu Science-based Industrial Park for three months. In 1990, he entered the Department of Metallurgical and Materials Engineering in New Mexico Institute of Mining and Technology to study for the master degree in the field of electronic ceramics. Master thesis titled as "Ferroelectric Fatigue Behavior of Bulk Modified Lead Zirconate Titanate Ceramics", He then transferred to University of Florida to continue his pursuing the doctor of philosophy with specialty in electronic materials in the Department of Materials Science and Engineering. He plans to develop his career in the field of the integration processing of semiconductor and electronic ceramic thin films for electronic devices and microelectromechanical systems.

I certify that I have read this study and that in my opinion it conforms to acceptable standards of scholarly presentation and is fully adequate, in scope and quality, as a dissertation for the degree of Doctor of Philosophy.



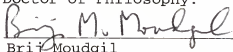
Rajiv K. Singh, Chairman
Professor of Materials
Science and Engineering

I certify that I have read this study and that in my opinion it conforms to acceptable standards of scholarly presentation and is fully adequate, in scope and quality, as a dissertation for the degree of Doctor of Philosophy.



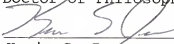
Paul H. Holloway
Professor of Materials
Science and Engineering

I certify that I have read this study and that in my opinion it conforms to acceptable standards of scholarly presentation and is fully adequate, in scope and quality, as a dissertation for the degree of Doctor of Philosophy.



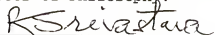
Brij Moudgil
Professor of Materials
Science and Engineering

I certify that I have read this study and that in my opinion it conforms to acceptable standards of scholarly presentation and is fully adequate, in scope and quality, as a dissertation for the degree of Doctor of Philosophy.



Kevin S. Jones
Professor of Materials
Science and Engineering

I certify that I have read this study and that in my opinion it conforms to acceptable standards of scholarly presentation and is fully adequate, in scope and quality, as a dissertation for the degree of Doctor of Philosophy.



Ramakant Srivastava
Professor of Electrical and
Computer Engineering

This dissertation was submitted to the Graduate Faculty of the College of Engineering and to the Graduate School and was accepted as partial fulfillment of the requirements for the degree of Doctor of Philosophy

August, 1998



Winfred M. Philips
Dean, College of Engineering

Karen Holbrook
Dean, Graduate School